UNIVERSITÀ DEGLI STUDI DI MILANO

Facoltà di Scienze Matematiche, Fisiche e Naturali

PhD Course in Chemistry

INVESTIGATION OF HALOGEN BONDING BY EXPERIMENTAL CHARGE DENSITY STUDIES AND THEORETICAL METHODS

Supervisor: Prof. Maurizio SIRONI
Assistant Supervisor: Dr. Alessandra FORNI
Assistant Supervisor: Dr. Stefano PIERACCINI
Coordinator: Prof. Emanuela LICANDRO

PhD Thesis:
Davide FRANCHINI
Matr. R11399

Anno Accademico 2017 / 2018

“I wish it need not have happened in my time," said Frodo. "So do I," said Gandalf, "and so do all who live to see such times. But that is not for them to decide. All we have to decide is what to do with the time that is given us.”

J. R. R. Tolkien, The Lord of the Rings.

"Kill the boy, Jon Snow. Winter is almost upon us. Kill the boy and let the man be born."

George R. R. Martin, A Dance with Dragons

“Nothing in life is to be feared, it is only to be understood. Now is the time to understand more, so that we may fear less.”

Marie Curie

TABLE OF CONTENTS

0. INTRODUCTION

0.1 PREFACE

In this thesis the results obtained during the three years of doctorate (2015-2018) will be illustrated. Although several different computational and crystallographic techniques have been exploited throughout my research activity, almost all projects were linked by a common thread: halogen bond,[1] a non-covalent interaction the nature of which will be briefly illustrated in the introduction section together with a brief description of the state of art of the research on this interaction.

Then, the different activities carried out during my PhD thesis will be described in the following Chapters according to the WBS (work breakdown structure) depicted in Figure 1, where each activity is denoted as WP (work-package).

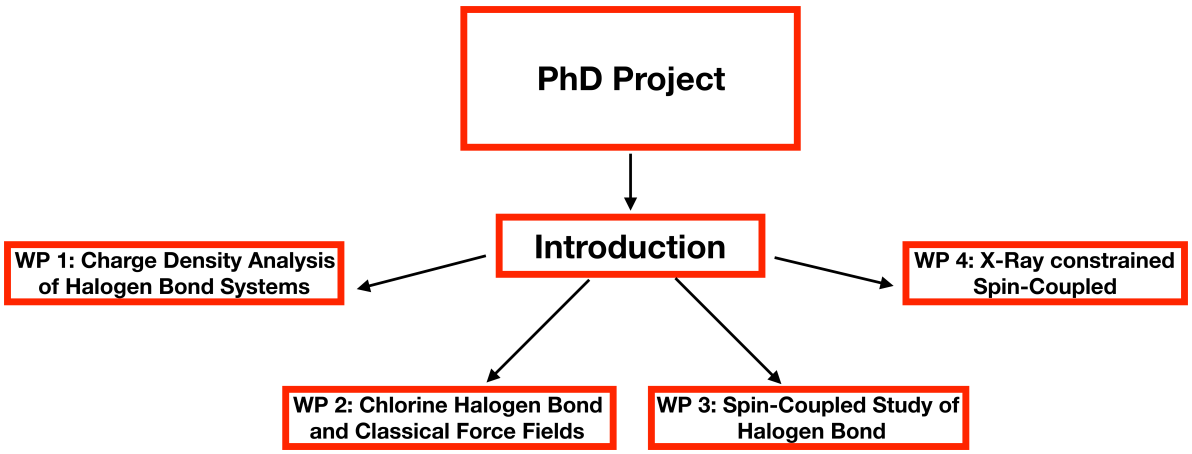

Figure 1: WBS of the thesis

In each of these chapters a short overview of the theoretical background of the methods employed throughout the WP will be outlined, then the description of the main results obtained will follow and, finally, some conclusion will be drawn.

It is worth mentioning here the content of the WP4. Indeed, in this chapter I exploited the X-ray constrained spin-coupled method developed by Dr. Alessandro Genoni (during the period I spent working in his research group in Metz, France) to study other systems than halogen bonding ones (particularly, I focused my attention on aromatic molecular crystals). However, the method is completely general and could be used to study halogen bonded crystalline systems in future projects.

0.2 INTRODUCTION

In 2009[1] the International Union of Pure and Applied Chemistry (IUPAC) launched a project (2009-032-1- 100): "to take a comprehensive look at intermolecular interactions involving halogens as electrophilic species and classify them".[2] An IUPAC recommendation[3] giving the first formal definition of halogen bonds was published in 2013 when the project ended. The definition states that "A halogen bond occurs when there is evidence of a net attractive interaction between an electrophilic region associated with a halogen atom in a molecular entity and a nucleophilic region in another, or the same, molecular entity."

Halogen bond (XB) is an interesting non-covalent interaction[4,5] between a halogen atom X (covalently bonded to a group R, such as an aromatic or aliphatic moiety or another halogen atom) and an acceptor group B (e.g. N, O, S and Se, anions like the halides: I^-, Br^-, Cl^- and F^-, or even the π electrons systems of aromatic molecules) characterized by a nucleophilic character, following the general scheme R-X···B (see Figure 2, for a schematic representation of the interaction geometry).

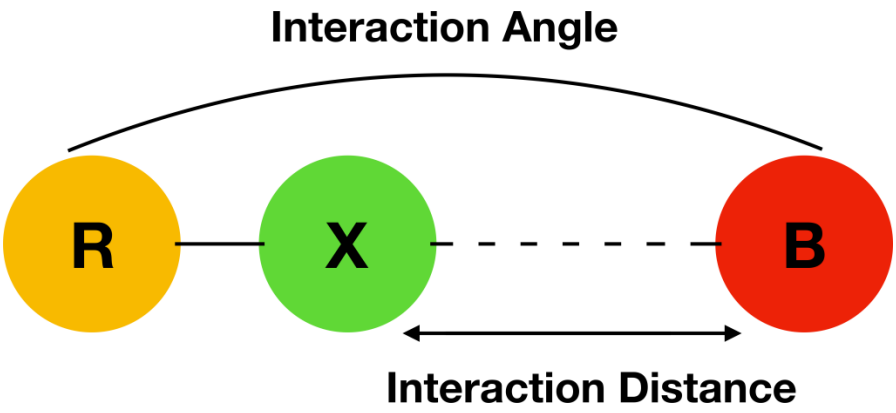

Figure 2: Halogen bond interaction scheme

This non-covalent interaction occurs in all the three physical states of matter. Indeed, halogen bonds is easily found in crystal structures of halogenated molecules, where interestingly (from a statistical analysis of the Cambridge Structure Database, CSD[6]) the interaction distances were

always found to be shorter than the sum of the Van der Waals radii of interacting atoms. Moreover, this kind of interaction could be used to direct chemical reactions in liquid phase,[7] for this reason several efforts have been undertaken to describe correctly the dependence of halogen bond features with respect to the solvent.[8] There are also several evidences of non-covalent interactions involving halogens in the gas phase,[9] where exploiting analytical techniques such as microwave spectroscopy, several halogenated adducts have been detected.

The name given to this interaction is a clear remainder to the ubiquitous hydrogen bond, with which XB shares several features, such as the strength and the great directionality. However, it possesses also different features with respect to hydrogen bond, resulting in cooperation or competition of these two non-covalent interactions in directing chemical processes.

There are several factors that contribute to determine the strength of this peculiar bonding interaction. The most important ones are:

- the electron withdrawing power of the substituent group R (see Figure 3, where an increasing in the electron withdrawing power of R magnifies the intensity of the σ-hole)
- the polarizability of the halogen atom, which decreases in the order I > Br > Cl >> F
- the basicity of the acceptor group B. Generally, the greater the basicity of B the greater will be the interaction strength.

Due to its counterintuitive nature, basically consisting in a halogen atom acting as electrophile, XB interaction has been only barely studied in the past and it has become a hot topic in modern chemistry and material science only quite recently. In fact, thanks to the more and more detailed investigations that allowed to gain fundamental insights into the nature of the interaction, several

research groups have envisaged the possibility of exploiting halogen bonding for functional applications.

Among them we can mention applications in medicinal chemistry and, particularly, in the rational design of new drugs. In fact, experimental evidences have interestingly shown that halogen bonds are able to efficiently stabilize protein-ligand complexes[10,11] and to compete with hydrogen bonds in stabilizing DNA junctions through brominated uracil-bases[12]. Then, in the last years it has been started to think to halogen bond as a potential tool to be exploited in drug design, also thanks to the enhanced membrane permeability and the increased half-lives of halogenated drugs.

Moreover, since XB interactions have been shown very efficient in tuning material properties (e.g., optical or magnetic properties)[13,14] and in directing supramolecular assemblies,[15–18] two important and related fields where halogen bond currently plays a crucial role are Materials Science and Crystal Engineering.[19]

As mentioned above, several efforts have been recently made either to propose models to shed further light on the nature of halogen bonding or to develop new useful, theoretical/computational tools to correctly predict properties of halogen bond-based systems. As an example, in the latter case, the increasing number of X-ray resolved protein structures with halogenated ligands led to the need of developing an efficient strategy to describe halogen bonds by means of classical force field methods.[20,21]

Concerning the different models that have been proposed over the years to rationalize halogen bonding, the one introduced by Politzer[22] could be probably considered as a milestone in this research area. In fact, it has been the first one to successfully and rationally describe the reason why halogens, which are commonly considered as "negative atoms", can interact with nucleophiles. According to the Politzer model, the electronic configuration of a halogen bonded to

a group R along the z-axis can be described as depicted in (1). This implies a depletion of electron density along the z-axis in the region outward the halogen atom, in comparison with the spherical electronic distribution on the isolated halogen atom. In the latter, in fact, each *p* orbital has a mean electron population equal to $\frac{5}{3}$..

$$s^2 p_x^2 p_y^2 p_z^1 \qquad (1)$$

The depletion of electron density on the halogen atom gives rise to a region of positive electrostatic potential (ESP), which is commonly called σ-hole, and a belt of negative ESP around this σ-hole to compensate it. This anisotropy of the ESP is the reason why halogens can interact with nucleophiles. Moreover, the model explains

- the trend in the strength of halogen bonding, which is simply associated with the maximum value of the ESP in the σ-hole (for a given acceptor, see Figure 3)[23]
- the great directionality of the XB interaction, which is strictly related to the narrow localization of the σ-hole around the z-axis (see Figure 3).

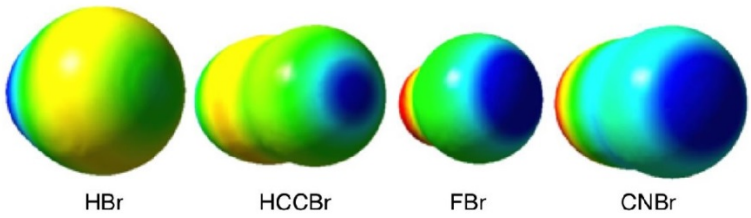

Figure 3: M06-2X/6-31G(d,p) ESP of four different brominated molecules, mapped onto the surface of electron density (0.002 electrons au^{-3}). The σ-hole increases from left to right, the same direction of halogen bond strengthening. Blue regions represent positive ESP regions, while red are negative ones.

Another model complementary to the Politzer one is the lump-hole model[24] that relies on the chemical interpretation of the Laplacian of the electron density, $\nabla^2\rho(r)$. The Laplacian for an atom

averages to zero when integrated over its atomic basin.[25] Atomic regions with negative (positive) Laplacian are regions of charge concentration (depletion)[25]. Following Bader's Quantum Theory of Atoms in Molecules,[25] and quoting Koritsanszky and Coppens,[26] "If two reactants approach each other in a Lewis acid-base-type reaction, their relative orientation can be predicted by the Laplacian function of their electron density. Charge concentrations/depletions of one molecule can be considered to be complementary to depletions/concentrations of the other".

When analyzing the Laplacian distribution around the halogen bonded atoms, it has been found the presence of an electron density depletion region ($\nabla^2\rho(r) > 0$), the hole, in proximity of the halogen atom and an electron density concentration region ($\nabla^2\rho(r) < 0$), the lump, localized on the acceptor. As the halogen atom approaches towards the acceptor, the hole will interact with the lump in a key-lock mechanism, thus leading to the establishment of the interaction (see Figure 4). Hence, the topology of the Laplacian explains all the main features of halogen bonding, namely, its electrophilic-nucleophilic character and strong directionality.

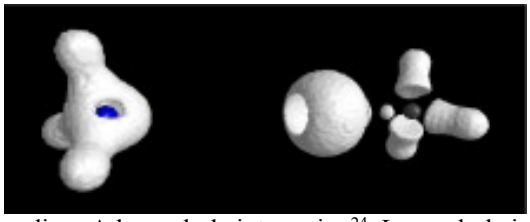

Figure 4: Taken from: Halogen bonding: A lump–hole interaction[24]. Lump–hole interaction between NH_3 (left) and CH_3Cl (right). The molecules are oriented so that the lump in the VSCC (Valence Shell Charge Concentration region) of nitrogen is aligned with the hole in the VSCC of chlorine.

So far, all these models have been accurately tested by several either theoretical[27] or experimental (mainly based on crystallographic techniques) strategies.[8]

Throughout this thesis, these models have been exploited to study new halogen bonding interacting systems (for example, in the experimental and theoretical charge density studies reported in chapter two, concerning investigation of the behavior and the features of halogen bond in iodinated molecular crystals). Moreover, we have tried to go further, proposing new methods to get a deeper insight into the nature of halogen bond. Indeed, a brand-new concept (see chapter 4) related to halogen bond has been devised, based on the Valence-Bond theory and in particular the Spin-Coupled method (that at the best of our knowledge, hasn't been used to investigate non-covalent interactions such as halogen bond).[28,29]

As mentioned in the preface to this thesis, during my period spent in the Dr. Alessandro Genoni's research group it was given to me the opportunity either to deepen my knowledges on quantum crystallography (QC) topics (a new branch of modern crystallography, combining the tools of quantum chemistry with the information supplied by crystals diffraction data) or collaborating with Dr. Genoni in developing and testing a new method in the framework of QC, besides attending the Quantum Crystallography Meeting[30] held in Nancy in 2017. As a result of this period the new X-ray Constrained Wavefunction (XCW)[31] technique has been successfully developed and tested (see chapter 5) on aromatic molecular crystals, such as crystalline benzene, proving to be a powerful tool to extract chemical information (such as weights of resonance structures) from the experimental structure factors.

1. CHARGE DENSITY STUDIES ON IODOALKYLIMIDAZOLES DERIVATIVES

1.1 INTRODUCTION

Herein is reported a joint experimental and theoretical charge density study on two different iodoalkylimidazoles (**1** and **2**), which crystallize forming I···N halogen bonded infinite chains. In these crystals, iodine is directly bonded to a perfluorinated alkyl chain, unlike the previously analyzed I···N halogen bonded complex of (E)-1,2-bis(4-pyridyl)ethylene with 1,4-diiodotetrafluorobenzene,[32] hereinafter denoted as **3**, where iodine is bonded to a fluorinated aryl ring. One of the aims of the present investigation was therefore to outline the differences in the charge density features of both C–I bonded and I···N non-bonded interactions between the two XB systems involving alkyl vs. aryl iodides. Two analogous alkylimidazole derivatives have been taken into consideration in order to assess the reproducibility of the experimental findings.

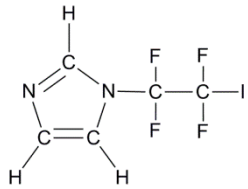

1

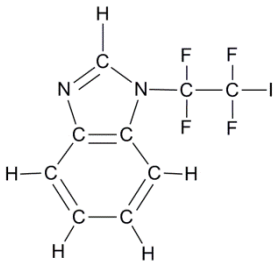

2

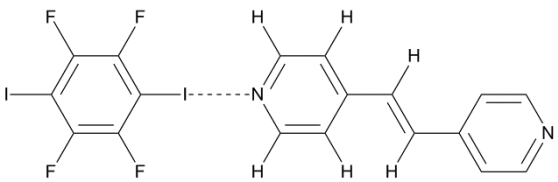

3

An interesting characteristic of **1** and **2** crystal structures is the abundance of F···F contacts below or just above the sum of the fluorine van der Waals radii. The nature of these interactions, which are ubiquitous in crystal structures of fluorinated molecules and were rarely investigated in previous charge density studies,[32–35] has been recently studied either experimentally[36–38] or theoretically,[39,40] after the recognized role of organic fluorine in crystal engineering[41] in spite of its low polarizability. Halogen···halogen (C–X1···X2–C) interactions are generally geometrically classified[6] according to the values of the two θ1=C–X1···X2 and θ2=X1···X2–C angles. Contacts

with θ1 ≅ θ2, including both cis and trans geometry when θ1 and θ2 differ from 180°, are referred to as type-I, whereas contacts with θ1 ≅ 180° and θ2 ≅ 90° are referred to type-II interactions. Type-I interactions are deemed to not have any stabilizing role in crystal structure (when ideally taken alone), while type-II interactions provide a stabilizing electrostatic contribution.[19] A CSD survey to retrieve X···X homohalogen contacts from halogen-substituted hydrocarbons indicates a dominance of type-I over type-II contacts when X is fluorine, unlike what observed for the heavier halogens.[38] This observation suggests that F···F contacts are generally determined by close packing, though the few type-II exceptions suggest that fluorine can potentially act as the electrophilic species in XB, contributing to govern the crystal packing motif.[42]

It is worthwhile to note that, differently from what generally observed for perfluorinated alkyl chains, which tend to be highly disordered in crystal structures at both fluorine and carbon atoms making in some cases altogether impossible to rationalize their statistical disorder, fluorine atoms in **1** and **2** are unexpectedly highly ordered. Charge density studies were made possible just thanks to this feature, allowing to characterize, for the first time, F···F interactions among perfluorinated alkyl chains.

1.2 THEORETICAL FRAMEWORK

1.2.1 THE ASPHERICAL-ATOM FORMALISM AND THE CHARGE DENSITY DETERMINATION

To account for the aspherical deformation of the electron density ($\rho(\mathbf{r})$) of a molecule (due to the establishment of chemical bonds) composing a crystal Hansen and Coppens[43] proposed a method in which the aspherical part of $\rho(r)$ is divided into three components, as shown in equation 1.

$$\rho(\mathbf{r}) = \rho_c(\boldsymbol{r}) + P_v\rho_v(k\boldsymbol{r}) + \rho_d(k'\boldsymbol{r}) \qquad (1)$$

Where ρ_c and ρ_v stand for the spherical core and valence electron density respectively, whereas ρ_d represents the aspherical deformation of the valence electron density, which can be expressed by using density normalized, real spherical harmonics (y_{lm}) as follows:

$$\rho_d(k'\boldsymbol{r}) = \sum_i R_l(k'r)\sum_{m=-l}^{l} P_{lm}y_{lm}(\tfrac{r}{r}) \qquad (2)$$

Here, $R_l(k'r)$ are proper radial functions, the expansion or contraction of which is regulated by a correspondent variation of k' parameter, and P_{lm} represents the Legendre associate functions. Then, it is possible to show that the corresponding scattering factor can be written as shown in equation 3.

$$f(\boldsymbol{h}) = f_c(H) + P_v f_v\left(\tfrac{h}{k}\right) + \sum_l \langle J(\tfrac{h}{k'})_l\rangle \sum_{m=-l}^{l} P_{lm}y_{lm}(\tfrac{\boldsymbol{h}}{h}) \qquad (3)$$

Where $\boldsymbol{h}$ and H represent the Bragg vector and the (h, k, l) triplets respectively, while $J(\frac{h}{k'})_l$ is the *l-th* order spherical Bessel function.

Then, once the scattering factors are obtained, it is possible to compute the calculated structure factors, which are refined against the experimental ones, to obtain the experimental electron density.

1.2.2 TOPOLOGICAL ANALYSIS OF THE CHARGE DENSITY

Once the (experimental or theoretical) charge density has been obtained, it is possible to apply the Bader's quantum theory of atom in molecules[25] in order to obtain several chemical properties of the molecules making up the analyzed crystal. Particularly, the topological analysis of the $\rho(\mathbf{r})$ could reveal different kind of critical points, the features of which provide chemical or physical insight. The critical points are defined as the points in which the first derivates of $\rho(\mathbf{r})$ vanish:

$$\nabla\rho(\mathbf{r}) = \hat{\boldsymbol{\imath}}\frac{\partial\rho}{\partial x} + \hat{\boldsymbol{\jmath}}\frac{\partial\rho}{\partial y} + \hat{\boldsymbol{k}}\frac{\partial\rho}{\partial z} = 0 \qquad (4)$$

Where, $\hat{\boldsymbol{\imath}}$, $\hat{\boldsymbol{\jmath}}$ and $\hat{\boldsymbol{k}}$ are unit vectors. The nature of critical point is determined by the sign of the second derivatives of $\rho(\mathbf{r})$ in that point. In particular, the critical point can be labelled as (ω, σ), where ω, the rank, is the number of non-zero eigenvalues of the Hessian of $\rho(\mathbf{r})$ in the critical point, while σ, the signature, corresponds to the sum of the signs of the curvatures (eigenvalues) at that point. The types of critical points that have a chemical meaning are the following:

- **(3, -3)** is a local maximum and it is found in the position where a nucleus is expected.
- **(3, -1)** is a saddle point located on the ZFS (zero-flux surface, a particular surface through which the flux of the $\nabla\rho(\mathbf{r})$ is zero) connecting two atoms. Particularly, it indicates a minimum of electron density along the ZFS, while it is a maximum in the two perpendicular directions. This type of critical point is often called bond critical point (BCP), because it is always found between two interacting atoms.
- **(3, +1)** is a saddle point called ring critical point because it is always found inside an intra- or intermolecular ring (e.g. the benzene ring).
- **(3, +3)** is a minimum of $\rho(\mathbf{r})$ and it is called cage critical point because it is located inside cage structures (such as the adamantane one).

Moreover, some important features of the critical points can be devised by computing the trace of the Hessian matrix, called the Laplacian of the $\rho(\mathbf{r})$ (see equation 5).

$$\nabla^2\rho(\mathbf{r}) = \frac{\partial^2\rho}{\partial x^2} + \frac{\partial^2\rho}{\partial y^2} + \frac{\partial^2\rho}{\partial z^2} \qquad (5)$$

The sign of $\nabla^2\rho(\mathbf{r})$ indicates regions of local concentration ($\nabla^2\rho(\mathbf{r}) < 0$) ore depletion ($\nabla^2\rho(\mathbf{r}) > 0$) of electron density, and then it can be exploited as a useful parameter to describe the nature of a particular kind of chemical interaction. In fact, $\nabla^2\rho_{bcp} < 0$ means that the electrons are locally concentrated around the bcp and shared by both nuclei, corresponding to a covalent interaction between the two nuclei. Otherwise, $\nabla^2\rho_{bcp} > 0$ indicates that the electrons are depleted from the bcp and concentrated in each of the atomic basins, predicting a closed shell behavior of the interaction. An additional criterion to characterize of the chemical bond is provided by the local electronic energy density $H_b = G_b + V_b$, where G_b and V_b indicate, respectively, the values of the local kinetic and potential energy densities at the bcp. The covalent interactions show negative values of H_b, owing to the dominating V_b contribution, while closed shell interactions exhibit positive values of H_b, since G_b is greater than $|V_b|$.

1.2.3 INTERACTING QUANTUM ATOMS (IQA)

The Interacting quantum atoms (IQA)[44] method is an energy partition scheme. The peculiarity of this scheme is that it partitions the energy of the molecule into atomic contributions according to the QTAIM[45] theory.

Following this partition technique, it is possible to obtain either monoatomic or diatomic contributions to the total energy.

Particularly, the interaction energy (E_{int}^{AB}) of two generic interacting atoms, A and B, (which is not to be confused with the binding energy, that takes into account also the contribution deriving from the deformation of electron density of the interacting atoms) can be expressed as follow:

$$E_{int}^{AB} = V_{cl}^{AB} + V_{xc}^{AB} \qquad (6)$$

Where V_{cl}^{AB} represents the electrostatic component of the interaction energy of the generic atomic pair AB, while V_{xc}^{AB} takes into account the exchange-correlation contribution to the interaction. Moreover, V_{cl}^{AB} can be further developed as shown in equation (7).

$$V_{cl}^{AB} = V_{nn}^{AB} + V_{en}^{AB} + V_{ne}^{AB} + V_{ee,cl}^{AB} \qquad (7)$$

Where V_{nn}^{AB} is the nuclear-nuclear electrostatic interaction energy between A and B and V_{en}^{AB} and V_{ne}^{AB} are the electron-nuclear and nuclear-electron interaction energies, respectively. Finally, $V_{ee,cl}^{AB}$ expresses the classical component of the electron-electron interaction energy.

The IQA approach could give important information about the nature of the interaction(s) established in a dimer.

1.3 MATERIALS AND METHODS

1.3.1 SYNTHESIS

The Synthesis has been carried out by Prof. Yuri L. Yagupolkii, who provided the crystals. *N-2*-Iodoperfluoroethylimidazole (**1**) and *N-2*-iodoperfluoroethylbenzimidazole (**2**) were obtained by reacting (benz)imidazole sodium salts with *2*-chloro-*1*-iodotetrafluoroethane in DMF using tetrabutylammonium bromide as a catalyst (Scheme 1). The reaction was complete after 10-15 min and required cooling to -10 – -15 ºC because of the high exothermicity. Solely the chlorine atom was substituted by the heterocyclic residue and **1** and **2** were obtained without any evidence of iodine substitution. Target compound **1** is obtained in yields no higher than 35% (with a large amount of by-products being also formed) and was purified by distillation in vacuo. Benzimidazole derivative (**2**) was obtained in good yield (72%) and purified by crystallisation from n-hexane.

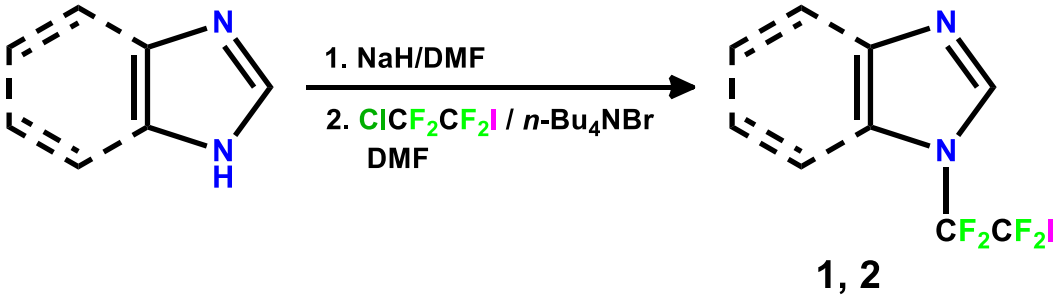

Scheme 1

1.3.2 DIFFRACTION EXPERIMENTS

Diffracted intensities were collected with graphite-monochromated Mo Kα radiation (λ = 0.71073 Å) at a nominal source power of 50 kV × 30 mA on a three-circle Bruker SMART APEX II

goniometer equipped with a CCD area detector and an Oxford Cryostream N_2 gas blower. The SAINT[46] program package was employed throughout to perform data reductions. Absorption correction was performed with SADABS[47] and the structure was solved with the SHELXS[48] structure solution program using direct methods. In Table 1 we report the details of crystal data and X-ray data collection.

Table 1. Experimental details for crystals of **1** and **2**.

	1	**2**
Chemical formula	$C_5H_3F_4IN_2$	$C_9H_3F_4IN_2$
Formula weight	293.99	344.05
Dimensions (mm^3)	0.27×0.18×0.09	0.31×0.26×0.25
Colour, habit	colourless, block	colourless, block
Crystal system	monoclinic	monoclinic
Space group	$P2_1/n$	$P2_1/n$
a (Å)	8.8030(13)	10.0833(5)
b (Å)	5.6607(9)	5.9718(3)
c (Å)	16.061(2)	18.1674(9)
β (°)	90.432(8)	105.156(2)
V ($Å^3$)	800.3(2)	1055.91(18)
Z	4	4
ρ_{calcd} ($g\ cm^{-3}$)	2.440	2.164
μ (mm^{-1})	4.016	3.062
λ (Å), MoKα	0.71073	0.71073
Scan method	ϕ and ω	ϕ and ω

T (K)	100(2)	100(2)
h,k,l range	–21→21,–14→13,–39→38	–25→23,–15→15,–45→46
$2\theta_{max}$ (°)	123.32	128.80
no. of measured reflns	185312	377638
no. of independent reflns	12513	17853
R_{int}	0.0276	0.0276
Data completeness (%)	98.2	98.7
Intensity decay	0.00	0.00
Absorption correction	multiscan	Multiscan
Transmission factors T_{min}, T_{max}	0.5877, 0.7520	0.2743, 0.3646

1.3.3 REFINEMENT AND TOPOLOGICAL ANALYSIS OF EXPERIMENTAL CHARGE DENSITIES

The final charge density model has been refined against the observed $|Fo|^2$ (squared structure factor amplitudes), exploiting the VALTOPO program,[49] using the procedure as described by Forni.[50] In Table 2 are summarized all the results related to the refinements of both the crystal structures of 1 and 2. The first refinement has been performed adopting the conventional independent atom model (IAM). Then, the same model with the inclusion of the third- and fourth- order Gram-Charlier terms on I atom has been exploited (IAM + CUM) and, finally, the multipole model has been introduced in the refinement (POP + CUM).

Table 2. Refinement details of **1** and **2**.

	1			**2**		
	IAM	IAM+CUM	POP+CUM	IAM	IAM+CUM	POP+CUM

reflections with $\|F_o\|>0$		11923			17196	
parameters	122	147	352	166	191	462
R(F)	0.0253	0.0233	0.0211	0.0285	0.0245	0.0219
wR(F)	0.0153	0.0136	0.0110	0.0217	0.0197	0.0175
$R(F^2)$	0.0217	0.0176	0.0135	0.0208	0.0165	0.0114
$wR(F^2)$	0.0285	0.0252	0.0196	0.0367	0.0323	0.0272
S	1.448	1.281	1.003	1.344	1.186	1.006
scale factor	0.989(1)	1.002(1)	1.000(1)	0.993(1)	1.010(1)	0.999(1)
$(shift/e.s.d.)_{max}$	<0.01	<0.01	<0.01	<0.01	<0.01	<0.01

By observing the data reported in Table 2, it is clear that, to obtain a good charge density model, it is important to include either the anharmonic parameters or the multipolar expansion on all heavy atoms. Atomic anomalous scattering factors were taken from International Tables for Crystallography (1995, Vol. C).

During the POP + CUM refinement, the following parameters have been varied: atomic position, anisotropic thermal and population parameters of the heavy atoms and third- and fourth-order Gram-Charlier coefficients.

Functional expansion up to hexadecapole level has been introduced on the iodine atom, while this expansion has been stopped to the octupole for F, N and C and at dipole level for the hydrogens and their positions have been determined through the 'polarized hydrogen atom' approach.[51] A single parameter has been refined for all F, N and C atoms core populations (which, then, exhibits spherical shapes).

An extinction correction has been introduced during the multipolar refinement of **2**, for this reason an isotropic parameter for a type II crystal, $\rho = 0.245(6)$, has been added to the model.[52]

The topological analysis of the experimental electron density has been carried out using the VALTOPO software.[49] Then, atomic charges have been computed by integrating the charge density over all the topological basins Ω, according to QTAIM.[45] The accuracy of the integration has been estimated through the errors in the evaluation of:

- the integrated number of electrons (N_Ω), $N_{err}(\%) = (\sum_\Omega m_\Omega N_\Omega - N_{cell})/N_{cell}$
- the basin volume (V_Ω), $V_{err}(\%) = (\sum_\Omega m_\Omega V_\Omega - V_{cell})/V_{cell}$
- the basin Laplacian (L_Ω), $L_{err}(\%) = (\sum_\Omega L_\Omega^2/N_{atoms})^{1/2}$.

1.3.4 QUANTUM CHEMICAL CALCULATIONS

Gas-phase calculations on either the isolated monomers or dimers of **1** and **2**, have been performed at DFT and (if possible) MP2 levels of theory using Gaussian09.[53]

The M06-2X functional has been adopted throughout for DFT computations because it was demonstrated to have good performances in describing geometrical, energetic and topological properties of halogen bonding systems,[54] including also weak interactions.[55,56] However, it should be noted that iodine, being a highly polarizable atom, may induce critical dispersion effects[57] and while it accountsatisfactorily for middle-range dispersion effect, it may fail when exploited to recover full dispersion.

The all-electron 6-311++G(d,p) basis set, previously used to study Br···N interaction,[50] has been used both for DFT and MP2 calculations. For the iodine atom, the exponents of the *s* and *p* diffuse functions taken from literature[58,59] were added to Basis Set Exchange site.[60,61]

Both single-point (on the experimental geometry) and BSSE-free geometry optimization calculations on selected dimers have been performed. [62]

The topological analysis of the electron density distributions was performed through the AIMALL program.[63]

Solid-phase periodic single-point calculations on both **1** and **2** at the experimental geometry have been performed using the Crystal14 software.[64] Shrinking factors along the reciprocal lattice vectors are: IS1 = 8, IS2= 8 and IS3 = 8. The corresponding grid of k points in reciprocal space, according to Pack-Monkhorst method is built by 170 points.

The same functional as the gas-phase calculations has been adopted, while the 6-311G(d,p) basis, with the exclusion of the diffuse functions (which should be avoided in periodic computations. However, future development should comprehend gas-phase calculation using 6-311G(d,p) basis to assess the consistency of the comparison between all the data presented here), has been used. The topological analysis of the electron density distributions obtained by these calculations has been performed with the Topond13 program.[65]

1.4 RESULTS AND DISCUSSION

1.4.1 STRUCTURE DESCRIPTION

Both compounds **1** and **2** crystallize in the $P2_1/n$ space group with one molecule in the asymmetric unit (see Figures 1 for partial views of the respective crystal packing diagrams). The bond lengths as obtained by the final multipole refinement (POP + CUM) are collected in Tables 3 and 4 for **1** and **2**, respectively, while Table 5 reports those referring to the C–I bond for **1-3**. These crystal structures (either for **1** or **2**) are formed by infinite linear chains in which the molecules interact by establishing I···N halogen bond between the iodine and the unsubstituted nitrogen of the imidazolic ring, N1.

Table 3. Experimental (first row) and computed (monomer optimization at M06-2X/6-311++G(d,p), second row, and MP2/6-311++G(d,p) levels, third row) bond lengths and bcp properties of **1**. Fourth row: bcp properties from periodic single point calculations at M06-2X/6-311G(d,p) level.

	R	R_x (Å)	R_x/R_e (Å)	ρ_b (eÅ^{-3})	$\nabla^2\rho_b$ (eÅ^{-5})	λ_1 (eÅ^{-5})	λ_2 (eÅ^{-5})	λ_3 (eÅ^{-5})
C5–I1	2.1488 (4)	1.0309	0.48	0.776(7)	1.46(6)	−2.86(7)	−2.71(7)	7.03(13)
	2.1477	*1.0503*	*0.49*	*0.833*	*−0.67*	*−3.09*	*−2.99*	*5.41*
	2.1448	*1.0461*	*0.49*	*0.842*	*−0.76*	*−3.18*	*−3.08*	*5.51*
				0.790	1.16	−2.83	−2.78	*6.77*
C5–C4	1.5489(5)	0.7695	0.50	1.750(17)	−10.2(4)	−12.5(2)	−12.3(2)	14.64(16)
	1.5505	*0.7761*	*0.50*	*1.751*	*−15.7*	*−13.0*	*−12.4*	*9.83*
	1.5515	*0.7763*	*0.50*	*1.760*	*−15.9*	*−13.1*	*−12.5*	*9.59*
				1.761	−15.9	−13.2	−12.5	*9.75*
C5–F3	1.3526(6)	0.5363	0.40	1.92(3)	−15.8(13)	−15.5(6)	−15.0(6)	14.6(4)
	1.3383	*0.4477*	*0.33*	*1.83*	*−0.8*	*−14.2*	*−12.4*	*25.8*
	1.3454	*0.4533*	*0.34*	*1.81*	*−3.1*	*−13.9*	*−12.2*	*23.0*
				1.76	−1.21	−13.2	−11.2	*23.2*
C5–F4	1.3485(6)	0.5290	0.39	2.02(3)	−17.6(14)	−16.8(6)	−16.0(6)	15.2(5)
	1.3389	*0.4480*	*0.33*	*1.83*	*−0.9*	*−14.2*	*−12.4*	*25.6*
	1.3463	*0.4537*	*0.34*	*1.80*	*−3.1*	*−13.8*	*−12.1*	*22.8*
				1.79	−1.6	−13.7	−11.5	*23.6*
C4–F1	1.3413(6)	0.5398	0.40	2.09(3)	−19.3(13)	−18.4(6)	−17.1(6)	16.2(6)
	1.3397	*0.4495*	*0.34*	*1.84*	*−2.2*	*−14.6*	*−12.8*	*25.3*
	1.3442	*0.4527*	*0.34*	*1.82*	*−3.5*	*−14.4*	*−12.6*	*23.4*
				1.84	−2.3	−14.6	−12.7	*24.9*
C4–F2	1.3424(6)	0.5483	0.41	2.10(3)	−18.8(13)	−18.3(6)	−17.5(6)	17.0(5)
	1.3399	*0.4498*	*0.34*	*1.84*	*−2.3*	*−14.6*	*−12.8*	*25.1*
	1.3452	*0.4535*	*0.34*	*1.82*	*−3.7*	*−14.3*	*−12.6*	*23.1*
				1.84	−2.8	−14.6	−12.7	*24.5*
C4–N2	1.4327(5)	0.6302	0.44	1.94(2)	−13.8(8)	−15.6(4)	−14.0(4)	15.8(2)

	1.4213	*0.5798*	*0.41*	*2.01*	*−21.9*	*−16.1*	*−14.1*	*8.4*
	1.4235	*0.5726*	*0.40*	*2.00*	*−22.4*	*−16.0*	*−14.1*	*7.7*
				1.95	−21.0	−15.5	−13.6	*8.1*
C1−N2	1.3705(5)	0.5861	0.43	2.15(3)	−18.5(10)	−18.2(5)	−14.5(5)	14.1(3)
	1.3787	*0.4810*	*0.35*	*1.96*	*−12.9*	*−13.2*	*−11.5*	*11.8*
	1.3833	*0.4797*	*0.35*	*1.94*	*−12.7*	*−13.2*	*−10.9*	*11.4*
				2.01	−13.5	−13.8	−12.1	*12.4*
C3−N2	1.3858(5)	0.5893	0.43	2.05(3)	−15.7(10)	−16.6(5)	−13.3(5)	14.2(3)
	1.3870	*0.4792*	*0.35*	*1.90*	*−10.6*	*−11.9*	*−10.7*	*12.0*
	1.3869	*0.4757*	*0.34*	*1.91*	*−10.7*	*−12.2*	*−10.5*	*12.0*
				1.91	−10.7	−12.0	−10.9	*12.2*
C1−N1	1.3108(6)	0.5957	0.45	2.61(3)	−23.4(10)	−22.8(5)	−19.2(5)	18.6(3)
	1.2979	*0.4763*	*0.37*	*2.50*	*−24.6*	*−20.4*	*−16.1*	*11.9*
	1.3175	*0.4916*	*0.37*	*2.41*	*−24.9*	*−19.4*	*−14.9*	*9.4*
				2.43	−24.0	−19.5	−15.5	*11.1*
H1−C1	1.080(13)	0.3596	0.33	1.90(4)	−17.0(9)	−20.0(5)	−17.8(5)	20.8(4)
	1.0790	*0.3761*	*0.35*	*1.94*	*−24.6*	*−19.3*	*−18.5*	*13.2*
	1.0800	*0.3708*	*0.34*	*1.93*	*−24.5*	*−19.1*	*−18.1*	*12.7*
				1.94	−24.9	−19.6	−18.9	*13.6*
C2−N1	1.3827(6)	0.6414	0.46	2.21(2)	−14.6(8)	−17.9(4)	−15.9(4)	19.2(3)
	1.3791	*0.5215*	*0.38*	*2.09*	*−20.8*	*−14.9*	*−13.5*	*7.5*
	1.3806	*0.5214*	*0.38*	*2.09*	*−21.2*	*−15.1*	*−13.2*	*7.1*
				2.06	−20.0	−14.5	−13.1	*7.7*
C2−C3	1.3641(6)	0.6862	0.50	2.26(2)	−20.5(6)	−18.9(4)	−14.1(4)	12.51(16)
	1.3605	*0.6515*	*0.48*	*2.20*	*−22.1*	*−16.7*	*−12.4*	*7.0*
	1.3771	*0.6619*	*0.48*	*2.13*	*−20.8*	*−16.1*	*−11.9*	*7.1*
				2.19	−22.05	−16.7	−12.5	*7.1*
H2−C2	1.081(13)	0.3794	0.35	1.88(3)	−17.1(8)	−19.2(5)	−17.1(5)	19.2(4)
	1.0777	*0.3833*	*0.36*	*1.93*	*−24.2*	*−18.8*	*−18.1*	*12.7*
	1.0805	*0.3779*	*0.35*	*1.91*	*−24.0*	*−18.5*	*−17.8*	*12.3*
				1.91	−24.0	−18.7	−18.1	*12.9*
H3−C3	1.095(13)	0.3439	0.31	1.77(3)	−15.2(10)	−18.6(5)	−17.3(5)	20.7(4)
	1.0761	*0.3779*	*0.35*	*1.92*	*−24.1*	*−18.8*	*−18.2*	*12.9*
	1.0787	*0.3723*	*0.35*	*1.91*	*−23.9*	*−18.6*	*−17.8*	*12.5*
				1.86	−22.7	−18.2	−17.6	*13.2*

Table 4. Experimental (first row) and computed (monomer optimization at M06-2X/6-311++G(d,p), second row, and MP2/6-311++G(d,p) levels, third row) bond lengths and bcp properties of **2**. Fourth row: bcp properties from periodic single point calculations at M06-2X/6-311G(d,p) level.

X−Y	*R*	R_x (Å)	R_x/R_e (Å)	ρ_b (eÅ^{-3})	$\nabla^2\rho_b$ (eÅ^{-5})	λ_1 (eÅ^{-5})	λ_2 (eÅ^{-5})	λ_3 (eÅ^{-5})
C5−I1	2.1468(4)	1.0382	0.48	0.782(9)	1.95(8)	−3.11(9)	−2.96(9)	8.02(16)
	2.1481	*1.0498*	*0.49*	*0.832*	*−0.69*	*−3.09*	*−2.99*	*5.39*
	2.1462	*1.0457*	*0.49*	*0.840*	*−0.79*	*−3.17*	*−3.07*	*5.46*
				0.798	1.10	−2.97	−2.92	*7.00*
C5−C4	1.5520(6)	0.7742	0.50	1.73(2)	−11.8(5)	−12.9(3)	−12.6(3)	13.7(2)
	1.5513	*0.7773*	*0.50*	*1.75*	*−15.6*	*−13.0*	*−12.4*	*9.8*
	1.5522	*0.7776*	*0.50*	*1.76*	*−15.9*	*−13.0*	*−12.4*	*9.6*
				1.75	−15.2	−13.1	−12.4	*10.3*
C5−F3	1.3569(7)	0.5440	0.40	1.97(4)	−18.1(17)	−17.2(8)	−15.9(7)	15.0(5)
	1.3392	*0.4481*	*0.34*	*1.83*	*−0.9*	*−14.1*	*−12.4*	*25.6*
	1.3463	*0.4536*	*0.34*	*1.80*	*−3.1*	*−13.8*	*−12.2*	*22.8*
				1.76	−3.5	−13.1	−11.1	*20.7*

C5–F4	1.3457(6)	0.5272	0.39	2.00(4)	–20.1(18)	–17.6(8)	–16.1(8)	13.7(6)
	1.3385	*0.4478*	*0.33*	*1.83*	*–0.9*	*–14.2*	*–12.4*	*25.7*
	1.3458	*0.4535*	*0.34*	*1.80*	*–3.1*	*–13.8*	*–12.2*	*22.9*
				1.80	–2.9	–13.9	–11.7	*22.8*
C4–F1	1.3411(7)	0.5309	0.40	2.06(4)	–22.2(19)	–18.8(8)	–18.1(8)	14.7(6)
	1.3415	*0.4501*	*0.34*	*1.83*	*–2.2*	*–14.5*	*–12.7*	*25.0*
	1.3460	*0.4534*	*0.34*	*1.81*	*–3.6*	*–14.2*	*–12.5*	*23.1*
				1.85	–4.5	–14.8	–12.9	*23.2*
C4–F2	1.3453(7)	0.5305	0.39	2.06(4)	–22.0(19)	–18.3(8)	–18.2(8)	14.4(6)
	1.3412	*0.4507*	*0.34*	*1.84*	*–2.5*	*–14.6*	*–12.7*	*24.8*
	1.3462	*0.4542*	*0.34*	*1.81*	*–3.9*	*–14.2*	*–12.5*	*22.9*
				1.83	–4.4	–14.4	–12.6	*22.6*
C4–N2	1.4266(5)	0.6370	0.45	2.01(3)	–16.1(10)	–16.9(5)	–15.4(5)	16.2(3)
	1.4176	*0.5768*	*0.41*	*2.01*	*–22.0*	*–16.1*	*–14.1*	*8.3*
	1.4201	*0.5699*	*0.40*	*2.00*	*–22.4*	*–16.1*	*–14.0*	*7.7*
				1.99	–21.1	–16.1	–14.0	*9.1*
C1–N2	1.3819(6)	0.5956	0.43	2.14(4)	–19.5(13)	–18.5(6)	–15.1(6)	14.0(4)
	1.3924	*0.4947*	*0.36*	*1.93*	*–15.0*	*–12.9*	*–11.7*	*9.7*
	1.3955	*0.4917*	*0.35*	*1.92*	*–14.7*	*–13.0*	*–11.2*	*9.5*
				2.01	–17.6	–14.4	–12.7	*9.5*
C3–N2	1.3985(6)	0.5755	0.41	2.02(4)	–16.9(14)	–16.6(7)	–13.5(7)	13.1(4)
	1.3970	*0.4925*	*0.35*	*1.88*	*–13.1*	*–11.8*	*–11.3*	*10.0*
	1.3966	*0.4887*	*0.35*	*1.89*	*–13.3*	*–12.1*	*–11.1*	*9.8*
				1.91	–15.4	–12.8	–11.7	*9.1*
C1–N1	1.3024(6)	0.5946	0.46	2.66(4)	–25.0(13)	–24.3(7)	–19.3(6)	18.6(4)
	1.2888	*0.4710*	*0.37*	*2.55*	*–24.6*	*–21.0*	*–16.6*	*13.0*
	1.3092	*0.4861*	*0.37*	*2.45*	*–25.1*	*–19.8*	*–15.3*	*10.0*
				2.50	–25.9	–20.6	–16.3	*11.0*
H1–C1	1.1286(5)	0.3533	0.31	1.74(4)	–13.5(12)	–18.3(7)	–16.6(7)	21.4(5)
	1.0800	*0.3748*	*0.35*	*1.95*	*–24.9*	*–19.4*	*–18.8*	*13.4*
	1.0816	*0.3697*	*0.34*	*1.93*	*–24.7*	*–19.2*	*–18.3*	*12.8*
				1.77	–20.8	–17.3	–16.7	*13.1*
C2–N1	1.3940(7)	0.6343	0.46	2.15(3)	–15.1(10)	–17.8(5)	–15.6(5)	18.3(3)
	1.3915	*0.5387*	*0.39*	*2.05*	*–20.9*	*–14.6*	*–13.7*	*7.4*
	1.3920	*0.5383*	*0.39*	*2.06*	*–21.2*	*–14.8*	*–13.5*	*7.0*
				2.06	–20.9	–15.1	–13.8	*8.0*
C2–C3	1.4032(5)	0.6951	0.50	2.10(3)	–18.3(8)	–17.0(5)	–13.8(4)	12.5(2)
	1.4035	*0.6785*	*0.48*	*2.08*	*–20.5*	*–15.6*	*–12.7*	*7.8*
	1.4154	*0.6861*	*0.48*	*2.04*	*–19.6*	*–15.1*	*–12.2*	*7.7*
				2.11	–21.1	–16.2	–13.1	*8.2*
C6–C2	1.3960(7)	0.6610	0.47	2.17(3)	–20.5(9)	–18.7(5)	–14.4(5)	12.6(2)
	1.3952	*0.6791*	*0.49*	*2.07*	*–20.6*	*–15.3*	*–12.8*	*7.5*
	1.4035	*0.6834*	*0.49*	*2.04*	*–20.2*	*–15.0*	*–12.4*	*7.2*
				2.08	–20.9	–15.6	–13.0	*7.8*
H6–C6	1.1058(5)	0.3732	0.34	1.76(4)	–13.7(11)	–17.4(6)	–16.2(6)	19.9(4)
	1.0827	*0.3870*	*0.36*	*1.90*	*–23.4*	*–18.0*	*–17.8*	*12.4*
	1.0860	*0.3814*	*0.35*	*1.88*	*–23.2*	*–17.8*	*–17.4*	*12.0*
				1.82	–21.5	–17.2	–16.9	*12.5*
C7–C6	1.3892(8)	0.6489	0.47	2.18(3)	–19.0(10)	–17.7(6)	–14.2(5)	12.9(3)
	1.3840	*0.6861*	*0.50*	*2.10*	*–20.8*	*–15.4*	*–12.6*	*7.3*
	1.3930	*0.6913*	*0.50*	*2.06*	*–20.2*	*–15.1*	*–12.2*	*7.1*
				2.09	–20.8	–15.7	–12.8	*7.7*
C7–C8	1.4082(8)	0.7004	0.50	2.10(3)	–16.8(8)	–16.4(5)	–14.0(5)	13.6(2)
	1.4051	*0.6992*	*0.50*	*2.02*	*–19.5*	*–14.7*	*–12.4*	*7.6*
	1.4142	*0.7038*	*0.50*	*1.99*	*–19.1*	*–14.4*	*–12.1*	*7.4*
				2.02	–19.6	–14.9	–12.6	*7.9*

H7–C7	1.0731(6)	0.3855	0.36	1.89(4)	–15.4(11)	–18.0(7)	–17.3(7)	19.9(4)
	1.0831	*0.3918*	*0.36*	*1.90*	*–23.3*	*–17.9*	*–17.6*	*12.2*
	1.0863	*0.3860*	*0.36*	*1.88*	*–23.1*	*–17.6*	*–17.3*	*11.8*
				1.96	–24.7	–19.1	–18.7	*13.1*
C8–C9	1.3902(8)	0.6673	0.48	2.16(3)	–19.0(9)	–17.7(5)	–14.2(5)	12.9(2)
	1.3860	*0.6829*	*0.49*	*2.08*	*–20.5*	*–15.3*	*–12.5*	*7.3*
	1.3951	*0.6883*	*0.49*	*2.05*	*–19.9*	*–15.0*	*–12.1*	*7.2*
				2.09	–20.6	–15.6	–12.7	*7.7*
H8–C8	1.0946(6)	0.3645	0.33	1.80(5)	–14.2(12)	–17.9(7)	–17.0(7)	20.7(5)
	1.0832	*0.3914*	*0.36*	*1.90*	*–23.3*	*–17.9*	*–17.6*	*12.2*
	1.0866	*0.3858*	*0.36*	*1.88*	*–23.1*	*–17.6*	*–17.3*	*11.8*
				1.87	–22.5	–17.8	–17.4	*12.6*
H9–C9	1.0528(5)	0.3934	0.37	1.96(4)	–17.9(11)	–18.9(7)	–17.4(6)	18.4(4)
	1.0816	*0.3871*	*0.36*	*1.90*	*–23.4*	*–18.1*	*–17.8*	*12.4*
	1.0840	*0.3814*	*0.35*	*1.89*	*–23.3*	*–17.9*	*–17.5*	*12.0*
				2.03	–26.6	–20.1	–19.7	*13.1*
C9–C3	1.3941(7)	0.6602	0.47	2.14(3)	–18.9(9)	–17.6(5)	–14.1(5)	12.8(2)
	1.3923	*0.6583*	*0.47*	*2.04*	*–20.0*	*–14.8*	*–12.3*	*7.2*
	1.4016	*0.6644*	*0.47*	*2.01*	*–19.5*	*–14.5*	*–11.9*	*7.0*
				2.06	–20.3	–15.2	–12.5	*7.5*

Beside I···N halogen bond several others C–H···F, C–H···I, C–H···π, F···F and, in the case of **2**, π···π interactions have been detected and, overall, they contribute to stabilize the crystal structures (see the topological analysis part of this discussion for further details on these weak interactions).

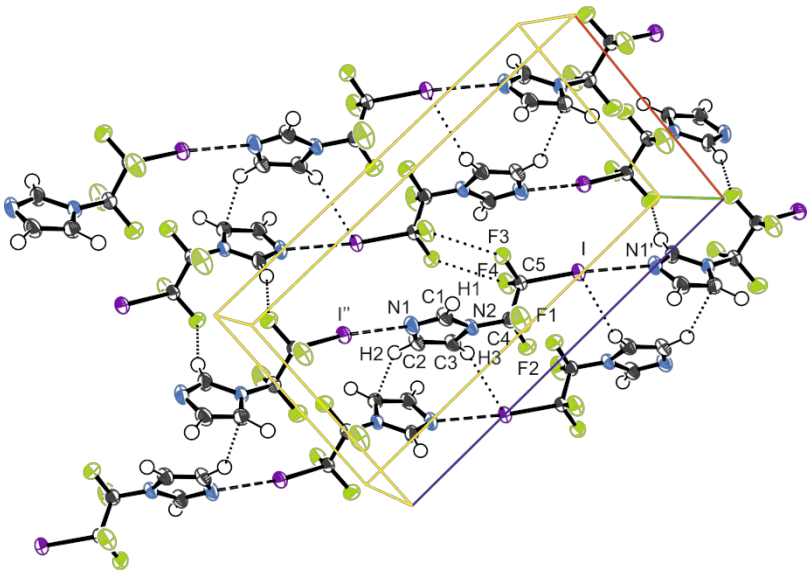

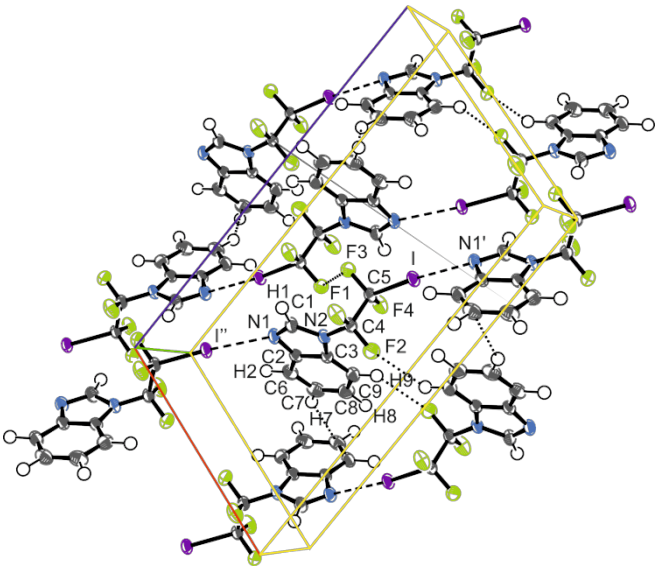

Figure 1. Packing diagrams of **1** (top) and **2** (bottom) at 100 K with atom numbering scheme, showing halogen bonding (dashed lines) and selected weaker interactions (dotted lines). Ellipsoids at 90% probability level.

The C-I bond lengths in **1** and **2 (**2.1488(4) and 2.1468(4) Å respectively) are slightly longer (by 0.052-0.050 Å) than that of **3**, this is mainly due to different nature (aliphatic in **1** and **2** vs aromatic in **3**) of the carbon atom linked to the iodine. Also, the I···N halogen bonding distances (2.8263(4) and 2.8260(4) Å in **1** and **2**, respectively) are longer than the same halogen bond found in **3 (**2.7804(8) Å) and this is a clear clue of the weaker halogen bond in the former structures. This observation (that will be confirmed by the topological analysis) is to be ascribed to two main factors: the greater nucleophilicity of the pyridinic nitrogen with respect to the imidazolic one and the greater electrophilicity of the iodine linked to an aromatic carbon, rather than to an aliphatic one.

All the gas-phase calculations (either DFT or MP2) performed on the **1** and **2** are able to well reproduce the C-I bond lengths. However, the same levels of theory slightly overestimate (by about

0.2 Å) the I···N1 distance. According to what reported in,[50] the latter result is a consequence of the rather flat potential energy surface between the halogen-bonding interacting monomers, which can therefore lead to slight deviations from the geometry of minimum energy owing to crystal packing effects. In agreement, the C5-I···N1 angles, 172.04(2) and 174.56(3) ° for **1** and **2**, respectively, are slightly lower than the DFT (178.1 and 178.5° for **1** and **2**, respectively) and MP2 (178.9° for **1**) optimized values. It is, also, worth noting that the experimental $\nabla^2\rho_{bcp}$ values for C-F bonds differ significantly from the same values obtained through both gas phase and periodic calculations. This observation can be imputed to the crystal field effect which make C-F interaction be more covalent with respect to the same bond observed in gas phase. However, it should also been pointed out that $\nabla^2\rho$ is a very sensitive function and some deviation from the experimental value can occour.

The final residual density maps ($F_{observed} - F_{multipole}$) (for both **1** and **2**), calculated in the planes containing halogen bonding and the imidazole rings, are quite featureless for either systems and the largest peaks are 0.21 and 0.27 eÅ^{-3} for **1** and **2**, respectively (see Figure 2).

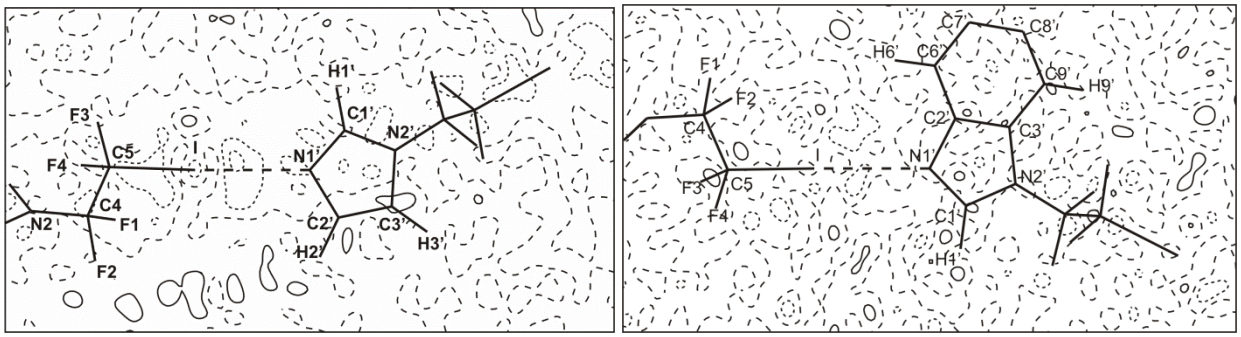

Figure 2. Residual density maps in the least squares plane defined by I, N1', C1' and C2' for **1** (left) and **2** (right) (the prime refers to operations *x-1/2,1/2-y,z-1/2* and *x+1/2,3/2-y,z+1/2* for **1** and

2, respectively). The contour interval is 0.10 eÅ^{-3}. Solid lines: positive contours, short dashed lines: negative contours, wide dashed lines: zero contours.

1.4.2 TOPOLOGICAL ANALYSIS OF THE ELECTRON DENSITY

The quantum theory of atom in molecules (QTAIM), briefly illustrated previously, has been exploited to analyze both the experimental and theoretical charge density, $\rho(\mathbf{r})$, and its Laplacian, $\nabla^2\rho(\mathbf{r})$. Figure 3 shows the experimental Laplacian of electron density for **1** and **2** in the plane containing the I···N halogen bond and the aromatic system. The Laplacian maps clearly reveal the different nature of the shared-shell (C–C, C–N, C–H and C–F bonds) and essentially closed-shell (C–I bond and I···N XB) interactions in the two systems.

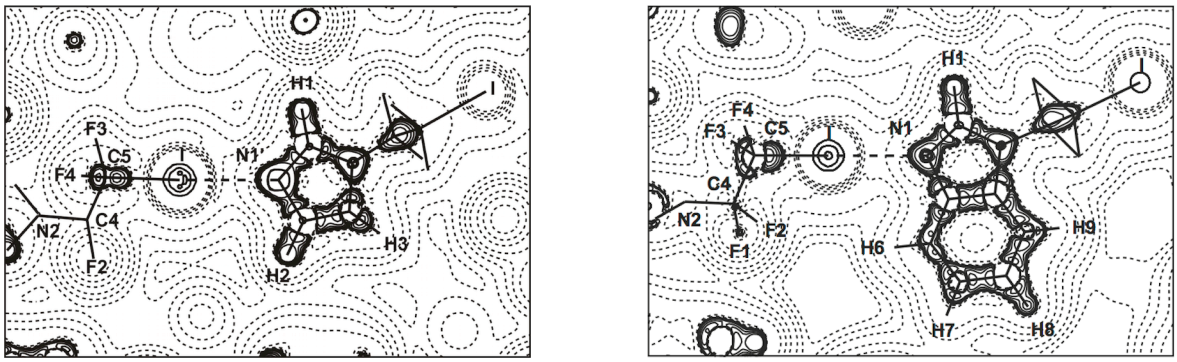

Figure 3. Laplacian of the experimental electron density distribution, $\nabla^2\rho(\mathbf{r})$, of **1** (left) and **2** (right) in the same planes as in Figure 2. The absolute values of the contours (au) increase in steps of 2×10^n, 4×10^n, and 8×10^n with n beginning at -3 and increasing in steps of 1. Positive values are denoted by dashed contours, negative values are denoted by solid contours.

All the topological properties considered during this charge density analysis (obtained either from POP + CUM refinement or gas- and solid-phase calculations) are summarized in Tables 3 for **1**

and 4 for **2**, whilst Table 5 reports specific properties for the C-I bond in the three crystalline structures.

Table 5. Experimental (first row) and computed (gas-phase monomer optimization at M06-2X/6-311++G(d,p), second row, and at MP2/6-311++G(d,p) levels, third row) C–I bond lengths and associated bcp properties of **1**, **2** and **3**.[3] Fourth row: bcp properties from periodic single point calculations at M06-2X/6-311G(d,p) level.

X–Y	*R*	R_x (Å)	R_x/R_e (Å)	ρ_{bcp} (eÅ^{-3})	$\nabla^2\rho_{bcp}$ (eÅ^{-5})	λ_1 (eÅ^{-5})	λ_2 (eÅ^{-5})	λ_3 (eÅ^{-5})
				1				
C5–I1	2.1488(4)	1.0309	0.48	0.776(7)	1.46(6)	–2.86(7)	–2.71(7)	7.03(13)
	2.1477	*1.0503*	*0.49*	*0.833*	*–0.67*	*–3.09*	*–2.99*	*5.41*
	2.1448	*1.0461*	*0.49*	*0.842*	*–0.76*	*–3.18*	*–3.08*	*5.51*
				0.790	1.16	–2.83	–2.78	*6.77*
				2				
C5–I1	2.1468(4)	1.0382	0.48	0.782(9)	1.95(8)	–3.11(9)	–2.96(9)	8.02(16)
	2.1481	*1.0498*	*0.49*	*0.832*	*–0.69*	*–3.09*	*–2.99*	*5.39*
	2.1462	*1.0457*	*0.49*	*0.840*	*–0.79*	*–3.17*	*–3.07*	*5.46*
				0.798	1.10	–2.97	–2.92	*7.00*
				3				
C7–I1	2.0969(7)	1.0660	0.51	0.76(1)	1.4(2)	–1.94	–1.42	4.79

In all the three systems, C-I bonds exhibit a quite low value of ρ_{bcp} and a low and positive value of $\nabla^2\rho_{bcp}$, compared with classical covalent bonds. These observations clearly indicate the presence of a mainly close-shell interaction. Surprisingly, the ρ_{bcp} associated to the C-I bcp of **1** and **2** results to be very similar to the one associated to **3**, despite the shorter C-I bond length in this last structure due to the aromatic character of the carbon linked to the halogen. This consideration allows to conclude the importance of crystal packing in influencing not only

intermolecular interactions but also intramolecular bonds. The importance of crystal packing turns out also from the comparison between gas-phase and solid-state calculations. Indeed, by observing the results obtained for **1** and **2** in Table 5, it is possible to observe that *in vacuo* computations tend to overestimate the electron density at the C-I bond critical point, providing a slightly negative $\nabla^2\rho_{bcp}$ value, thus suggesting a higher degree of covalence with respect to experimental findings (since it should be remembered that negative values of $\nabla^2\rho_{bcp}$ denotes covalent interaction according to QTAIM), in which crystal field effect gives its contribution in determining the nature of halogen bond. However, all the experimental topological properties of C–I bond in **1** and **2** are fully recovered by *Crystal14* (fourth row in Table 5) calculations, underlying the importance of considering the crystal environment in the description of this bond.

Table 6. Experimental (first row) and selected computed (gas-phase M06-2X/6-311++G(d,p), second row;[a] solid-state M06-2X/6-311G(d,p), third row; gas-phase MP2/6-311++G(d,p), fourth row) distances and bcp properties of intermolecular interactions for which a bond path was found in **1**.

X···Y	R_e /Å	C–X···Y/°	R_x/R_e	ρ_{BCP}/eÅ^{-3}	$\nabla^2\rho_{BCP}$/eÅ^{-5}	G_{BCP}/HÅ^{-3}	V_{BCP}/HÅ^{-3}	H_{BCP}/ρ_{BCP}	$\lvert V_{BCP}\rvert/G_{BCP}$
halogen bond									
I···N1^{X}	2.8263(4)	172.04 (2)	0.55	0.205(2)	1.897(18)	0.146(1)	–0.159(3)	–0.064(2)	1.091(3)
	2.9973	178.13		0.126	1.328	0.087	–0.081	0.048	0.930
				0.168	1.765	0.120	–0.116	0.024	0.967
	3.0415	178.88		0.122	1.195	0.080	–0.076	0.028	0.958
hydrogen bonds									
H2···N2^{VIII}	2.796 (12)	132 (1)	0.40	0.039(2)	0.572(12)	0.030(1)	–0.020(2)	0.254(9)	0.676(8)
H3···I1^{VI}	3.071 (13)	148(1)	0.34	0.039(3)	0.512(12)	0.027(1)	–0.019(2)	0.214(9)	0.696(8)
H3···F1^{II}	2.603 (12)	114 (1)	0.47	0.038(1)	0.648(10)	0.034(1)	–0.022(1)	0.307(6)	0.654(5)
H1···F3^{III}	2.519 (13)	166 (1)	0.41	0.023(3)	0.616(12)	0.030(1)	–0.017(2)	0.549(19)	0.576(8)
F-F interactions									
F4···F1^{II}	2.7405(7)	155.86 (3)	0.50	0.047(1)	1.007(9)	0.052(1)	–0.033(1)	0.390(4)	0.644(3)
			0.50	0.050	0.933	0.057	–0.049	0.162	0.859
				0.050	0.945	0.058	–0.050	0.160	0.863
F3···F4^{IV}	2.9295(7)	136.09(4)	0.50	0.032(1)	0.660(5)	0.033(1)	–0.021(1)	0.398(3)	0.617(2)
			0.50	0.038	0.706	0.043	–0.036	0.175	0.841
				0.038	0.722	0.044	–0.036	0.186	0.837

F2···F2^{VI}	2.9696 (8)	125.72 (4)	0.50	0.027(1)	0.550(6)	0.028(1)	–0.017(1)	0.394(4)	0.609(4)
			0.50	0.036	0.651	0.039	–0.032	0.189	0.828
				0.033	0.662	0.039	–0.032	0.222	0.812
F3···F3^{IV}	3.1193(8)	96.55(3)	0.50	0.024(1)	0.456(4)	0.023(1)	–0.014(1)	0.373(3)	0.607(3)
			0.50	0.028	0.540	0.031	–0.024	0.268	0.761
				0.027	0.553	0.031	–0.024	0.278	0.763
F2···F4^{VI}	3.2332(7)	174.44(4)	0.50	0.016(1)	0.295(2)	0.015(1)	–0.009(1)	0.376(2)	0.585(2)
			0.49	0.013	0.304	0.016	–0.014	0.333	0.714
				0.015	0.363	0.019	–0.013	0.420	0.680
F3···F1^{III}	3.3104(8)	164.92 (4)	0.50	0.012(1)	0.236(2)	0.012(1)	–0.007(1)	0.422(3)	0.565(3)
			0.49	0.013	0.304	0.016	–0.010	0.421	0.652
				0.042	0.631	0.037	–0.005	0.655	0.554
F2···F1^{V}	3.5256(9)	128.06(4)	0.50	0.008(1)	0.143(1)	0.007(1)	–0.004(1)	0.409(2)	0.551(2)
			0.50	0.008	0.200	0.009	–0.005	0.500	0.571
				0.007	0.203	0.010	–0.005	0.655	0.554
					other interactions				
F4···C1^{IV}	3.2486 (7)	104.47 (3)	0.47	0.029(1)	0.433(5)	0.022(1)	–0.015(1)	0.270(3)	0.649(4)
F3···C2^{IV}	3.2459 (6)	116.99 (3)	0.45	0.037(1)	0.562(4)	0.030(1)	–0.020(1)	0.667(3)	0.266(2)
H1···H2^{I}	3.077 (18)	107(1)	0.47	0.017(1)	0.217(6)	0.011(1)	–0.007(1)	0.251(7)	0.620(9)

[a]Geometry optimization on the XB dimer for the I···N interaction, single point calculations for the F···F interactions

Codes for the symmetry operations:

I	x, y + 1, z
II	x, y – 1, z
III	–x +2, –y +1, –z + 2
IV	–x + 2, –y, –z + 2
V	–x + 1, –y + 1, –z + 2
VI	–x + 1, –y, –z + 2
VII	–x + 3/2, y + 1/2, –z + 5/2
VIII	–x + 3/2, y – 1/2, –z + 5/2
IX	x + 1/2, –y + 1/2, z + 1/2
X	x – 1/2, –y + 1/2, z – 1/2

Table 7. Experimental (first row) and selected computed (gas-phase M06-2X/6-311++G(d,p), second row;[a] solid-state M06-2X/6-311G(d,p), third row) distances and bcp properties of intermolecular interactions for which a bond path was found in **2**.

X···Y	R_e /Å	C–X···Y/°	R_x/R_e	ρ_{BCP}/eÅ^{-3}	$\nabla^2\rho_{BCP}$/eÅ^{-5}	G_{BCP}/HÅ^{-3}	V_{BCP}/HÅ^{-3}	H_{BCP}/ρ_{BCP}	$\lvert V_{BCP}\rvert/G_{BCP}$
					halogen bond				

I···N1^{VIII}	2.8260(4)	174.56 (3)	0.55	0.198(2)	1.84(2)	0.140(1)	–0.151(3)	–0.056(3)	1.079(3)
	3.0118	178.52		0.122	1.30	0.084	–0.078	0.050	0.928
				0.175	1.65	0.113	–0.110	0.015	0.976
hydrogen bonds									
H8···I^{III}	3.557(19)	116(1)	0.40	0.023(1)	0.248(7)	0.013(1)	–0.009(1)	0.188(6)	0.671(9)
H1···F3^{IV}	2.589(17)	166(1)	0.48	0.018(2)	0.235(10)	0.012(1)	–0.007(1)	0.253(13)	0.623(16)
H1···F3^{IV}	2.589(17)	166(1)	0.41	0.023(3)	0.523(15)	0.026(1)	–0.015(2)	0.46(2)	0.589(11)
H9···F2^{III}	2.555 (16)	140(1)	0.44	0.029(3)	0.588(15)	0.030(1)	–0.018(2)	0.395(14)	0.612(9)
hydrogen-π interactions									
H7···C7^{VII}	2.771 (17)	144.5(9)	0.38	0.045(4)	0.654(16)	0.035(1)	–0.024(2)	0.241(12)	0.693(10)
F-F interactions									
F4···F1^{I}	2.7513(7)	166.47(4)	0.50	0.046(1)	0.973(11)	0.050(1)	–0.032(1)	0.392(5)	0.642(4)
			0.50	0.045	0.887	0.054	–0.045	0.194	0.838
				0.042	0.752	0.046	–0.039	0.164	0.849
F3···F3^{V}	2.9319(8)	100.36(4)	0.50	0.035(1)	0.705(9)	0.036(1)	–0.023(1)	0.381(5)	0.627(4)
			0.50	0.043	0.745	0.046	–0.040	0.141	0.868
				0.042	0.752	0.046	–0.039	0.164	0.849
F3···F4^{V}	2.9502(7)	140.84 (4)	0.50	0.032(1)	0.639(6)	0.032(1)	–0.020(1)	0.389(3)	0.619(3)
			0.50	0.036	0.682	0.040	–0.034	0.185	0.833
				0.036	0.689	0.041	–0.033	0.204	0.819
F3···F1^{IV}	3.1684(8)	147.48(4)	0.50	0.016(1)	0.326(3)	0.016(1)	–0.009(1)	0.421(4)	0.577(3)
			0.50	0.018	0.407	0.223	–0.016	0.333	0.073
				0.018	0.413	0.022	–0.015	0.386	0.692
π-π interactions									
C1···C7^{II}	3.3621(8)		0.50	0.038(1)	0.405(9)	0.022(1)	–0.016(1)	0.158(5)	0.732(7)
other interactions									
F1···C9^{I}	3.1725 (8)	119.00(4)	0.47	0.036(1)	0.541(7)	0.028(1)	–0.019(1)	0.262(4)	0.667(5)
F4···C1^{V}	3.2900 (8)	99.13(4)	0.48	0.029(1)	0.413(5)	0.021(1)	–0.014(1)	0.263(4)	0.650(4)

[a]Geometry optimization on the XB dimer for the I···N interaction, single point calculations for the F···F interactions.

Codes for the symmetry operations:

I	x, y + 1, z
II	x, y – 1, z
III	–x +1, –y +1, –z + 2
IV	–x, –y + 2, –z + 2
V	–x, –y + 1, –z + 2
VI	–x + 1/2, y + 1/2, –z + 3/2
VII	–x + 1/2, y – 1/2, –z + 3/2
VIII	x + 1/2, –y + 3/2, z + 1/2

IX	x + 1/2, –y + 1/2, z + 1/2
X	x – 1/2, –y + 3/2, z – 1/2
XI	x – 1/2, –y + 1/2, z – 1/2

Table 8. Experimental (first row)[a] and, when available, computed (at M06-2X/6-311++G(d,p) level on the geometry-optimized gas-phase dimer, second row, and at periodic M06-2X/6-311G(d,p) level on the experimental geometry, third row) I···N distances and associated bcp properties of **1**, **2** and **3**.[3]

X···Y	R_e /Å	C–X···Y/°	R_x/R_e	ρ_{bcp}/eÅ^{-3}	$\nabla^2\rho_{bcp}$/eÅ^{-5}	G_{bcp}/HÅ^{-3}	V_{bcp}/HÅ^{-3}	H_{bcp}/ρ_{bcp}	$\lvert V_{bcp}\rvert/G_{bcp}$
					1				
I···N1‘	2.8263(4)	172.04 (2)	0.55	0.205(2)	1.897(18)	0.146(1)	–0.159(3)	–0.064(2)	1.091(3)
	2.9973	178.13		0.126	1.328	0.087	–0.081	0.048	0.930
				0.168	1.765	0.120	–0.116	0.024	0.967
					2				
I···N1‘	2.8260(4)	174.56 (3)	0.55	0.198(2)	1.84(2)	0.140(1)	–0.151(3)	–0.056(3)	1.079(3)
	3.0118	178.52		0.122	1.30	0.084	–0.078	0.050	0.928
				0.175	1.65	0.113	–0.110	0.015	0.976
					3				
I···N1‘	2.7804(8)	179.32(4)	0.54	0.236(2)	1.96(2)	0.164(1)	–0.191(3)	–0.114(3)	1.165(3)

[a] The primes refer to the following symmetry operations: *x-1/2,1/2-y,z-1/2* (**1**), *x+1/2,3/2-y,z+1/2* f (**2**) and *1-x, 1-y,-1-z* (**3**).

The topological properties of all the non-covalent interactions in **1** and **2** are reported in Tables 6 and 7, while the one related to the bcp of the I···N halogen bond in the three structures are collected in Table 8. As already described,[32] this halogen bond is a mainly closed-shell interaction (due to the positive sign of the Laplacian of the electron density at the bcp) with a partial shared shell character (because of the negative sign of H_{bcp}/ρ_{bcp}), unlike the previously studied Br···N halogen bond,[50] which exhibits a positive value of H_{bcp}/ρ_{bcp} which indicates a fully closed shell

interaction of this weaker halogen bond. By comparing the topological properties derived for the three iodinated systems, it is however evident the substantially different character of the I···N XB in **1** and **2** (showing practically the same topological properties) with respect to **3**. The longer XB distance in **1** and **2** is in fact associated with significantly lower ρ_{bcp} and H_{bcp}/ρ_{bcp} (in magnitude) values, indicating weaker interaction with lower shared-shell character for the alkylated iodo-derivatives owing to both intrinsic and extrinsic factors, as elucidated above. Theoretical analysis on the gas-phase XB dimers of **1** and **2** provides lower ρ_{bcp} and positive H_{bcp}/ρ_{bcp} values for the I···N interaction, mainly as a consequence of the longer I···N distances as obtained without including the crystal environment. In fact, periodic calculations at the experimental geometry allow topological properties to get closer to the experimental ones.

1.4.3 F···F INTERMOLECULAR INTERACTIONS

Both **1** and **2** crystal structures present several weak interactions such as F···F, C-H···I, C-H···F and C-H···π hydrogen bonds and π-π non-covalent bond (see Table 9). Among these weak interactions it has been paid particular attention to the F···F contacts. By looking at their C–F···F–C geometry, they cover a large range of θ_1, θ_2 angles (see Tables 6 and 7). In all cases, they correspond to very weak interactions, as can be inferred by observing the very low values of ρ_{bcp} associated with these contacts. Moreover, these interactions show a pure closed shell character, due to their positive values of $\nabla^2\rho_{bcp}$ and H_{bcp}/ρ_{bcp}, resulting from the topological analysis of the charge densities distributions as obtained either experimentally or theoretically. The rather random reciprocal disposition of the interacting fluorine atoms in **1** and **2** is clearly indicative of the close packing origin of all the F···F interactions in the present structures, differently from the few type-II electrostatic F···F interactions reported in the literature.[38] As an example of such interactions, in

Figure 4 the experimental Laplacian map for the F1…F4' contact has been reported. The map clearly illustrates the closed shell character of the interaction.

Table 9. θ_1, θ_2 angles (°) associated with the C–F_1···F_2–C contacts (θ_1=C–F_1···F_2 and θ_2=F_1···F_2–C).[a]

Contact	θ_1	θ_2
1		
F4···F1^{II}	155.86	153.98
F3···F4^{IV}	136.09	105.58
F2···F2^{VI}	125.72	125.72
F3···F3^{IV}	96.55	96.55
F2···F4^{VI}	174.44	103.30
F3···F1^{III}	125.04	164.92
F2···F1^{V}	128.06	115.44
2		
F4···F1^{I}	160.04	166.35
F3···F3^{V}	100.36	100.36
F3···F4^{V}	140.97	99.66
F3···F1^{IV}	160.04	166.35

[a] Codes for the symmetry operations for **1** and **2** as in Tables 6 and 7, respectively.

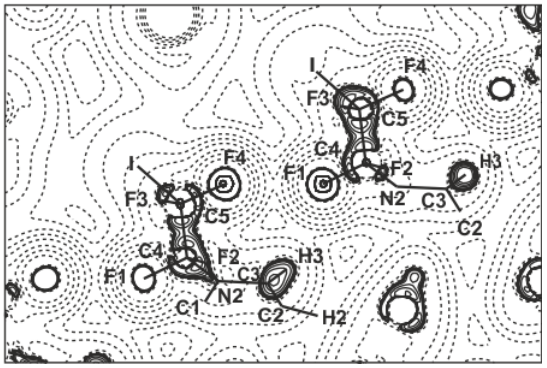

Figure 4. Laplacian of the experimental electron density distribution, $\nabla^2\rho(\mathbf{r})$, of **1** in the least-squares plane of atoms C4, F1, F4', C5'(the prime refers to operation $x,1+y,z$). The absolute values of the contours (au) increase in steps of 2×10^n, 4×10^n, and 8×10^n with n beginning at -3 and

increasing in steps of 1. Positive values are denoted by dashed contours, negative values are denoted by solid contours.

It is worth to underline that[66] the presence of a bond path connecting two atoms proves that the pairwise interaction, overall, is stabilizing, even if a repulsive electrostatic (i.e., classic) component of interaction energy is observed. The bond path is in fact associated with a privileged electron-exchange (i.e., quantum mechanical) channel which contributes to lower the mutual interatomic interaction energy. In order to estimate this effect in the F···F interaction, an interacting quantum atom (IQA) analysis has been performed on two representative F···F interacting dimers, the structure of which has been extracted from the experimental structure of **1**.

The IQA analysis has been performed on the dimers interacting through the $F1^{I}$···F4 (dimer 1) and the F2···$F4^{II}$ (dimer 2) close contacts (see Figure 5 for the related molecular graphs). The former dimer represents a type-I F···F interaction, whereas the latter is close to a type-II interaction (at least from a geometrical point of view).[6]

The three main terms of IQA (as underlined in equation 6) analysis as obtained from such analysis are reported in Table 10 for the full body of atom pairs connected by a bond path in the investigated dimers.

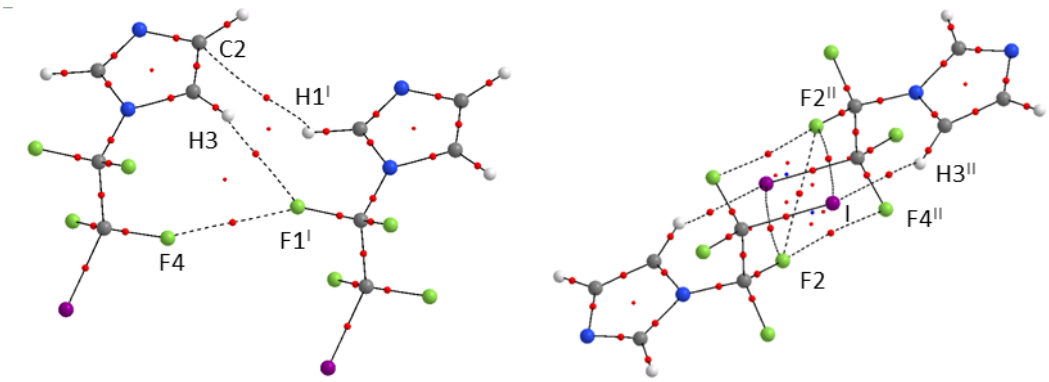

Figure 5. M06-2X/6-311++G(d,p) molecular graphs of dimer 1 (left) and dimer 2 (right) of compound **1** extracted from crystal structure.

Table 10. Electron density at bcp (eÅ^{-3}), interatomic distance (Å), θ_1 and θ_2 angles (°) and IQA total (E_{int}^{AB}), electrostatic (V_{cl}^{AB}) and exchange-correlation (V_{xc}^{AB}) interaction energies (kcal mol^{-1}) computed at M06-2X/6-311++G(d,p) level in selected dimers of **1** for pairs of atoms connected by a bond path.[a]

A···B	ρ_{bcp}	$R_{A\cdots B}$	θ_1	θ_2	E_{int}^{AB}	V_{cl}^{AB}	V_{xc}^{AB}
Dimer 1							
F4···F1^{I}	0.050	2.740	155.85	153.98	37.68	41.16	-3.48
H3···F1^{I}	0.042	2.603	114.31	- [b]	-9.71	-7.89	-1.82
C2···H1^{I}	*0.018*	*3.304*	- [b]	*122.55*	*2.86*	*3.59*	*-0.73*
Dimer 2							
F2···F4^{II}	0.016	3.233	174.44	103.30	36.63	37.53	-0.90
F2···F2^{II}	0.036	2.970	125.72	125.72	39.95	42.12	-2.18
I···H3^{II}	0.050	3.071	- [b]	148.42	-2.88	1.72	-4.60
I···F2^{II}	*0.021*	*3.841*	*72.038*	*72.038*	*-13.53*	*-11.91*	*-1.62*

[a]See Figure 5 for the molecular graphs of dimers 1 and 2. In italics the interactions which are not present in the experimental charge density distribution. Symmetry operations: I, *x, y – 1, z*; II, *–x + 1, –y, –z + 2*. [b]Non-significant for this interaction.

As expected (from the positive values of QTAIM derived fluorine atomic charges), all the reported F···F contacts, independent on their relative disposition, have E_{int}^{AB} positive due to the large electrostatic V_{cl}^{AB} term, denoting destabilizing interactions. On the other hand, the H3···F1^{I} and H3^{II}···I contacts (associated with C–H···X hydrogen bonds) are stabilizing interactions, though only the former has negative and quite high electrostatic contribution, in agreement with its more favorable geometry. It is however to be noted that all F···F contacts have non-negligible exchange-correlation V_{xc}^{AB} contribution, which explains the presence of a bond path[66] and, interestingly, is larger the greater is the value of ρ_b, independent on V_{cl}^{AB}. It is finally to be remarked that the

additional C2···H1^{I} and I···F2^{II} interactions (italicized in Table 10), associated with strongly distorted C–H···π hydrogen bond and X···X' XB, respectively, are not observed in the experimental charge density distribution, so that their meaning is questionable being most probably a consequence of neglecting the crystal environment.

1.4.4 ATOMIC CHARGES

Atomic net charges have been determined in **1** and **2** through integration of electron density over the topological atomic basins Ω, at both experimental and theoretical (from gas-phase calculations over the optimized isolated molecules and XB dimers) levels. These charges are reported in Tables 11 and 12. By observing these values, it is possible to observe positive experimental net charges for iodine in both **1** and **2** (q = 0.22(2) and 0.28(2) e for **1** and **2**, respectively), which are well reproduced by theoretical calculations on either the monomer (0.20 e in both structures) or XB interacting dimers (0.28 and 0.27 e for **1** and **2**, respectively, for the iodine involved in the XB interaction). Furthermore, by observing the differences between the summation of the net charges of interacting molecules in the dimers (XB donor and acceptor) it is possible to estimate, if any, the charge transfer, which is about 0.02 e in both compounds, then significantly lower than that computed in the XB dimer of **3**, 0.08 e, in agreement with the stronger interaction detected in the latter system. On the other hand, the experimentally derived molecular dipole moment, obtained by summing the integrated atomic dipoles, provides the values 4.2(5) and 5.8(9) D for **1** and **2**, respectively, which are greater than those computed for the gas-phase optimized isolated molecules (2.40 and 1.99 D at M06-2X, and 2.55 and 2.22 D at MP2 levels for **1** and **2**,

respectively) by about 65-75 and 190-160 % (according to the theoretical method), respectively. This increase of the dipole moment (with respect to theoretical values) is due to large polarization effects of the molecules within the XB chain, which is mainly due to the crystal matrix effects because the geometrical variations from gas-phase to solid-state induce only negligible changes (from 2.40/2.55 to 2.75/2.78 D in **1** and from 1.99/2.22 to 2.34/2.47 D in **2**, according to the M06-2X/MP2 method).

Table 11. Experimental and computed atomic net charges q(e) for **1** as obtained by QTAIM partitioning.

	experimental	M06-2X/6-311++G(d,p)		
		Monomer	Dimer	
			Donor	Acceptor
I1	0.221(19)	0.205	0.276	0.219
F1	-0,533(7)	-0.633	-0.636	-0.633
F2	-0,524(7)	-0.633	-0.635	-0.631
F3	-0,460(5)	-0.628	-0.632	-0.627
F4	-0,493(5)	-0.629	-0.633	-0.628
N1	-0,663(11)	-1.135	-1.139	-1.172
N2	-0,932(12)	-1.224	-1.227	-1.226
C1	0,498(10)	1.026	1.027	1.034
C2	0,186(8)	0.444	0.441	0.446
C3	0,173(12)	0.321	0.325	0.331
C4	1,267(4)	1.588	1.570	1.588
C5	0,829(6)	1.041	0.987	1.038
H1	0,130(7)	0.100	0.098	0.111
H2	0,072(9)	0.062	0.058	0.072
H3	0,234(8)	0.096	0.094	0.103
Tot	0,01(4)	0.001	-0.026	0.025

Table 12. Experimental and computed atomic net charges q(e) for **2** as obtained by QTAIM partitioning.

	experimental	M06-2X/6-311++G(d,p)		
		Monomer	Dimer	
			Donor	Acceptor
I1	0.278(20)	0.201	0.271	0.211
F1	-0.518(7)	-0.634	-0.636	-0.633
F2	-0.578(7)	-0.635	-0.637	-0.634
F3	-0.534(6)	-0.628	-0.631	-0.627
F4	-0.560(8)	-0.631	-0.634	-0.630
N1	-0.654(13)	-1.139	-1.141	-1.174

N2	-0.966(9)	-1.217	-1.218	-1.218
C1	0.507(15)	1.056	1.057	1.063
C2	0.199(6)	0.404	0.405	0.403
C3	0.187(9)	0.324	0.329	0.326
C4	1.447(4)	1.590	1.575	1.592
C5	0.898(5)	1.040	0.989	1.039
C6	-0.104(11)	-0.003	-0.005	-0.002
C7	0.019(13)	-0.012	-0.013	-0.007
C8	-0.057(12)	-0.004	-0.006	-0.001
C9	0.058(13)	0.012	0.012	0.015
H1	0.183(10)	0.105	0.103	0.114
H6	0.117(15)	0.053	0.050	0.056
H7	-0.011(10)	0.028	0.025	0.034
H8	0.111(10)	0.030	0.027	0.034
H9	-0.011(15)	0.058	0.058	0.061
Tot	0.01(2)	-0.002	-0.020	0.022

1.4.5 INTERACTION ENERGIES

The XB interaction energies, ΔE, for both **1** and **2** interacting molecules have been evaluated through M06-2X/6-311++G(d,p) calculations as the difference between the energy of the XB dimer, optimized on the BSSE-free potential energy surface, and the sum of the energies of the optimized monomers. These interaction energy values are -5.7 and -5.5 kcal/mol for **1** and **2**, respectively, which are smaller than the one reported for **3**, though computed at lower level of theory, amounting to -6.5 kcal/mol, in perfect agreement with the previous observation on the topological properties of the electron density that provided a stronger XB interaction in **3**. A rough estimation of the XB interaction energy can be obtained exploiting the Espinosa-Molins-Lecomte (EML) formula $E_{int} = 0.5V_{bcp}$,[67] which was first derived to estimate O···H hydrogen bonds and actually referring to interatomic rather than intermolecular interactions. This formula, applied on the experimental V_{bcp} values, provides the following interaction energy values, E_{int} = -7.4, -7.0 and -8.9 kcal/mol for **1**, **2** and **3**, respectively. While it is clear that a local topological descriptor such as V_{bcp} does not necessarily correlate with the intermolecular interaction energy ΔE, it is however

interesting to exploit the approximate 'universal' relationship depicted by Spackman,[68] which relates the EML atom-atom interaction energies, for a given atomic pairwise, with their interaction distances *d*. This relationship can be depicted as follow, $E_{int} = -3.30 \exp(-2.669[d - d_{vdW}]/\text{Å})$ kJ mol^{-1}, where d_{vdW} represents the sum of vdW radii. By adopting this expression to estimate the I···N interaction energy, the values $E_{int} = -5.2$ kcal/mol (for both **1** and **2**) and −5.8 kcal/mol (for **3**) are obtained. These ΔE values are much closer to the computed ones with respect to the values obtained by exploiting directly the EML relationship, thus confirming the universality of the relationship proposed by Spackman. Morever, concerning the ΔE result for **3**, it is worth noting that it is in good agreement with the previously reported interaction energy, -5.0 kcal/mol, as obtained by calculations based on the Gavezzotti's PIXEL approach on the XB molecular pair of **3**.[69] Finally, using the full set of 28 V_{bcp} values for the intermolecular contacts in **1** and **2**, the log-linear plot of EML values, $-E_{int}$, vs. the internuclear distances minus the sum of vdW radii (see Figure 6 and Table 13) provides a line of best fit $E_{int} = -3.56 \exp(-2.384[d - d_{vdW}]/\text{Å})$ kJ mol^{-1}, i.e., very close to that reported by Spackman.[68]

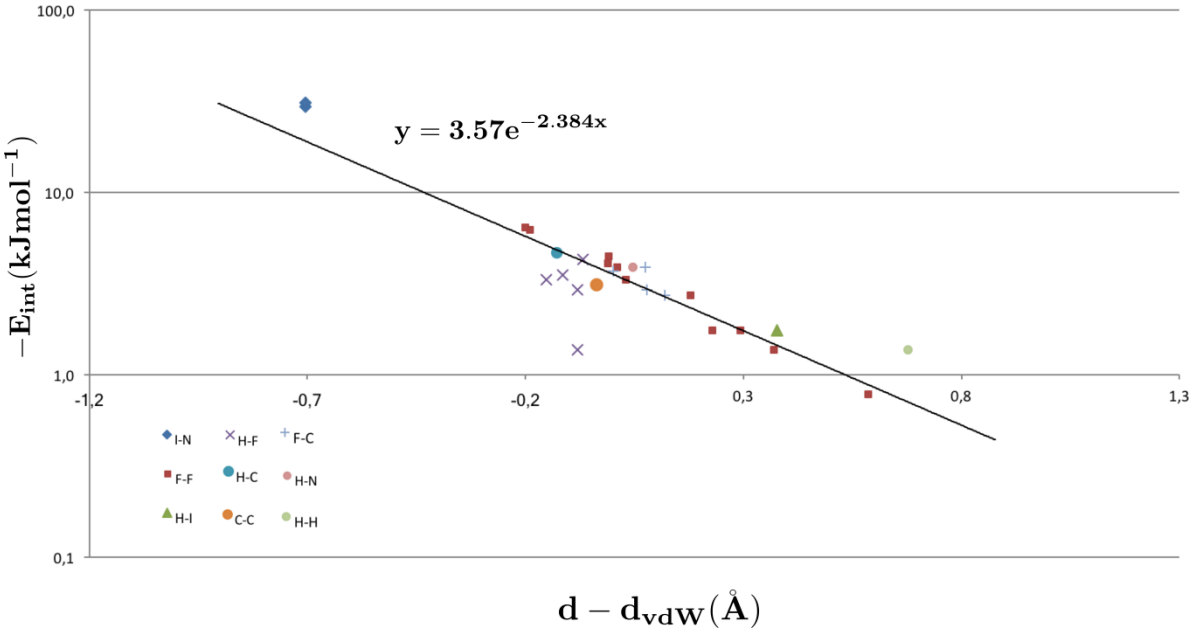

Figure 6. Log-linear plot of EML interatomic interactions ($-E_{int}$), vs internuclear distance (d) minus the sum of van der Waals radii (d_{vdW}). The black line is the best fit to the data of **1** and **2**.

Table 13. Approximated interaction energies E_{int} derived by the EML formula, $E_{int} = 0.5V_{bcp}$ (3rd and 4th columns, in kcal/mol and kJ/mol, respectively) and by the Spackman relationship, $E_{int} = -3.30 \exp(-2.669[d - d_{vdW}]/Å)$ kJ mol^{-1} (5th and 6th columns, in kJ/mol and kcal/mol, respectively) for the intermolecular contacts found in structures of **1** and **2**.

	Interaction	EML E_{int} (kcal mol^{-1})	EML E_{int} (kJ mol^{-1})	Spackman E_{int} (kJ mol^{-1})	Spackman E_{int} (kcal mol^{-1})
1	I···N1	7.4	30.9	21.6	5.2
2	I···N1	7.0	29.4	21.6	5.2
1	F4···F1	1.5	6.4	5.6	1.3
1	F3···F4	1.0	4.1	3.4	0.8
1	F2···F2	0.8	3.3	3.0	0.7
1	F3···F3	0.7	2.7	2.0	0.5
1	F2···F4	0.4	1.8	1.5	0.4
1	F3···F1	0.3	1.4	1.2	0.3
1	F2···F1	0.2	0.8	0.7	0.2
2	F4···F1	1.5	6.2	5.5	1.3
2	F3···F3	1.1	4.5	3.4	0.8
2	F3···F4	0.9	3.9	3.2	0.8
2	F3···F1	0.4	1.8	1.8	0.4
1	H2···N2	0.9	3.9	2.9	0.7
1	H3···I	0.9	3.7	4.4	1.1
1	H3···F1	1.0	4.3	3.9	0.9
1	H1···F3	0.8	3.3	4.9	1.2

1	F4···C1	0.7	2.9	2.7	0.6
1	F3···C2	0.9	3.9	2.7	0.6
1	H1···H2	0.3	1.4	0.5	0.1
2	H8···I	0.4	1.8	1.2	0.3
2	H1···F3	0.3	1.4	4.1	1.0
2	H1···F3	0.7	2.9	4.1	1.0
2	H9···F2	0.8	3.5	4.5	1.1
2	H7···C7	1.1	4.7	4.7	1.1
2	C1···C7	0.7	3.1	3.7	0.9
2	F1···C9	0.9	3.7	3.3	0.8
2	F4···C1	0.7	2.7	2.4	0.6

1.5 CONCLUSIONS

Two new iodoalkylimidazole derivatives, able to self-assemble through I···N halogen bond, have been studied by performing a multipolar refinement of the electron density against X-ray diffraction data and, also, by exploiting theoretical techniques (both gas-phase and periodic-phase). After the charge density distribution determination, the topological analysis has been carried out on both structures to feature the C–I and I···N bonding and non-bonding properties according to QTAIM. Then, those properties have been compared with the ones previously reported on an I···N complex based on iodoaryl derivative, allowing to infer the effect of hybridization of the carbon atom bound to the XB donor site. Furthermore, the energetic features of XB interaction have been studied through both quantum-mechanical and approximated (i.e., based on local topological descriptors) methods. Also, the full set of intermolecular interactions present in crystal structures have been analyzed, and particular attention has been devoted to F···F interactions, which are present in large number in **1** and **2**. The nature of these contacts has been explored through the use of either QTAIM or IQA energy decomposition schemes. It appears that F···F interactions are mainly electrostatic, though the stabilizing exchange-correlation energy term is non-negligible, explaining the presence of the associated F···F bcp's.

2. CHLORINE HALOGEN BOND IN THE FRAMEWORK OF CLASSICAL FORCE FIELD

2.1 INTRODUCTION

In this project,[70] a brand new and effective strategy to describe chlorine halogen bond (XB) by means of classical force-field has been proposed, exploiting a set of extra-point charges or pseudo-atoms (Pa's), correctly placed around the halogen atom. This approach has been applied to the XB-analysis of a set of chlorinated model systems in which the interaction was established with the carbonyl oxygen of the capped alanine (see Figure 1). To test the model, molecular mechanics (MM) geometry optimization has been performed on the systems previously described. Also, one brominated molecule has been studied to verify the generality of the Pa's strategy. These model systems have been adopted to reproduce halogenated ligands occurring in real biological systems. Indeed, in this kind of systems it is very frequent to find halogen atom linked to an aromatic backbone.[71] The reason why aromatic rings, instead of aliphatic, are preferred is that the first ones could be exploited (from an applicative point of view) thanks to the higher stability of their C-X bond. Thus, this feature reduces the chance of an eventual release of halide in the organism.

The position of the halogens, the nature of the ring and the types of substituent have been changed in order to cover a wide spectrum of halogen bonding interactions.

As a result of this analysis, it turns out that the approach here illustrated significantly improves the description of interaction distances and angles (the geometrical parameters) of chlorine halogen bond compared to the previously proposed strategy, involving only one extra-point charge.[20 72,73,74]

To benchmark these geometrical parameters, M06-2X/6-311++G(d,p) computations on the systems depicted in Figure 1 have been performed.

Furthermore, it has been demonstrated that a re-parametrization of the general AMBER force field (GAFF37) van der Waals parameters for chlorine is mandatory to get a clear definition of chlorine halogen bond occurring in biological systems, in agreement with the results obtained by Scholfield et al.[75]

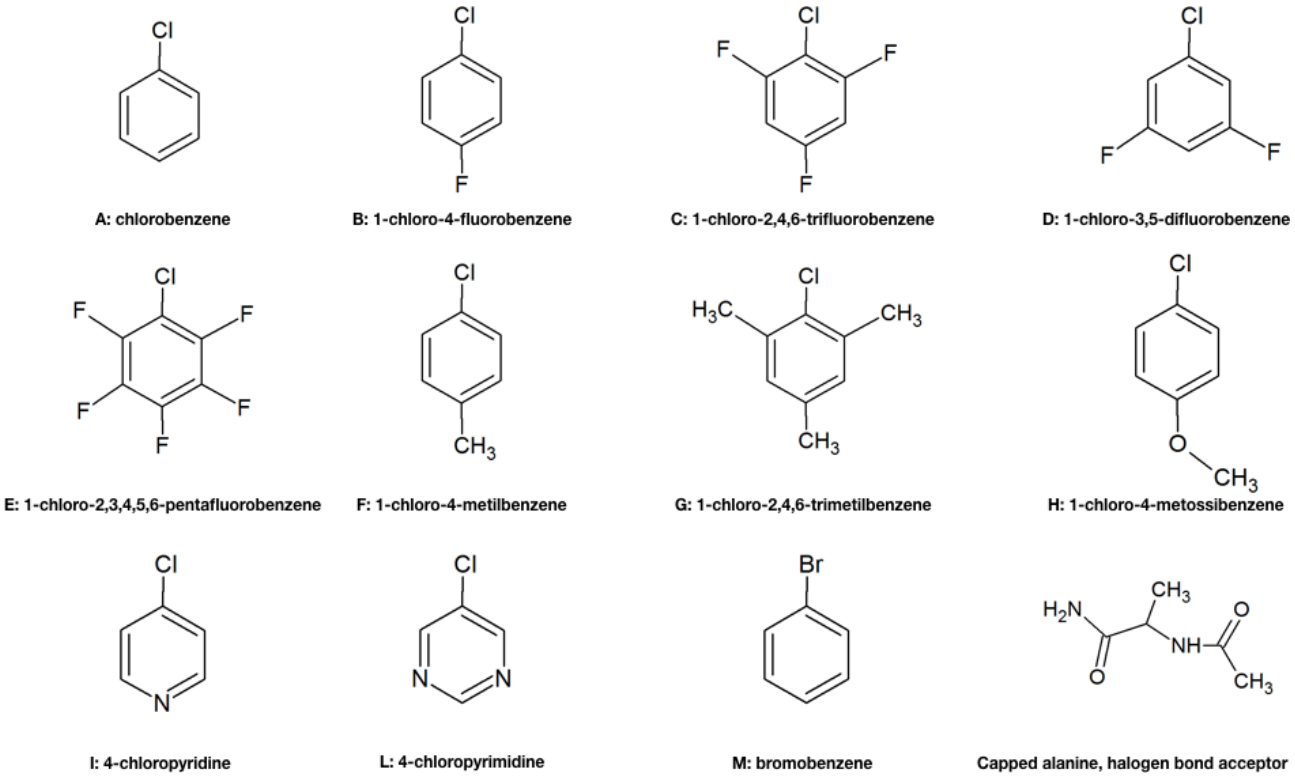

Figure 1. Chlorinated (A÷L) or brominated (M) model systems chosen to study halogen bond with the carbonyl oxygen of the capped alanine through the Pseudo-atom(s) strategy.

2.2 THEORETICAL BACKGROUND

Many approaches have been exploited to determine atomic charges in the framework of classical force field. As an example, it is possible to derive atomic charges from semiempirical or ab initio calculations by fitting them to reproduce electrostatic potential (ESP).

A drawback of ESP fitting method is the following: the points used in fitting the charges must lie outside the van der Waals surface of the molecule. Hence, "buried" charges (e.g. a sp^3 carbon) tend to be poorly determined. So, to enhance the potentialities of this strategy, an evolution has been optimized: the Restrained Electrostatic Potential (RESP). [76] This evolution relies on the addition of a penalty function (χ^2_{rstr}) defined as:

$$\chi^2_{rstr} = a \sum_j \left(\left(q_j^2 + b^2 \right)^{\frac{1}{2}} - b \right) \quad (1)$$

Where a and b stand for two numerical parameters, while q_j represents the Coulombic charge of atom j. In this way, the new function to be optimized in order to fit the quantum mechanical ESP is the following:

$$\chi^2 = \chi^2_{esp} + \chi^2_{rstr} \quad (2)$$

where χ^2_{esp} is the Figure of merit that was optimized in the ESP procedure by applying the least-squares method to ESP function.

The electrostatic charges derived in this way are then exploited to model the electrostatic term in the functional form of classical force field. The problem arises when a single point-charge has to be attributed to halogens, since they would require a sort of multipole function, rather than a single value, to correctly describe the anisotropy of their electrostatic potential which is responsible of the σ-hole. Several efforts have been undertaken to solve this issue, among which it is worth mentioning the solution proposed by Rendine et al.[20] Their approach was based on the

adding of an extra-point charge, that actually represents the halogen σ-hole, directly linked to the halogen, during both the RESP procedure and the following MD simulations. As a result of this Pseudo-atom introduction, it has been possible to correctly describe iodine and bromine halogen bonding in ligand-receptor systems (such as those mentioned above). However, this approach failed for chlorine (as it will be illustrated in the discussion session of this chapter) that requires a higher level of accuracy in order to be modelled in biological environments.

2.3 MATERIALS AND METHODS

Gaussian 09[53] has been exploited to perform quantum mechanical geometry optimizations in order to obtain the geometries of eleven halogenated molecules complexed by capped alanine (see Figure 1) that have been taken as a benchmark, throughout this chapter, for MM energy minimization results. Particularly, for all the eleven systems, DFT (BSSE free) computations have been carried out by adopting the M06-2X[77] functional, which is a hybrid meta-GGA highly suitable for describe non-covalent interaction such as halogen bonding.[56] The 6-311++G(d,p) basis set has been adopted for all the atoms of the complexes.

As mentioned in the previous section, to obtain either the electrostatic atomic point charges or the Pa's ones, RESP computations have been performed, as implemented in AMBER11, by using the electrostatic potential derived from previous RHF/6-31G(d,p) Gaussian09 computations. To prove the goodness of the RESP fitting to the RHF electrostatic potential, the relative root mean square error (RRMS) has been monitored.

In order to better describe the weak chlorine σ-hole two different dispositions of pseudo-atoms have been tried-out (see Figure 2). The first one ('1Pa' disposition, A) is based on a single pseudo-atom (Pa) linked to the X atom along the D–X bond extension, pointing towards the XB acceptor. Hence, several X–Pa distances have been tested as described in the next session. In the second disposition ('5Pa' disposition, B), five Pa's were added to the central halogen. The first one was placed in the same position as the one of the previous disposition, whilst the other four were located on the two directions perpendicular to the R-X bond axis, with the aim of describing in a more accurate way the negative belt of the ESP around the halogen atom. In this way, each of these four Pa's is the vertex of a square with the chlorine atom in the center.

In this case also, several distances between the halogen and the Pa's have been tried-out. To parametrize the halogenated molecules the GAFF3[78] force fields have been adopted, while for the capped aminoacidic residues the ff99SBildn force field has been exploited.[79]

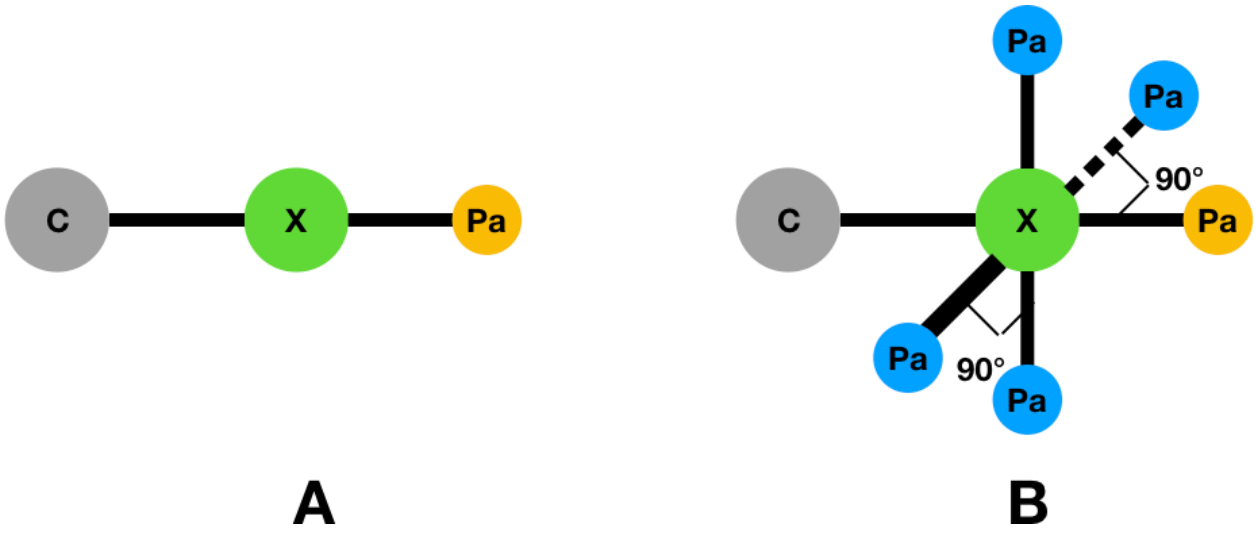

Figure 2. Dispositions of pseudo-atoms adopted to describe the anisotropy of electron density around the halogen atoms (X, Pa and C stand for halogen, pseudo-atom and carbon, respectively). A: '1Pa' disposition where one Pa is used to simulate the charge of the σ-hole. B: '5Pa' disposition, where one Pa (in yellow) is used to simulate the charge of the σ-hole and the other four surrounding the halogen are used to enhance the negative belt.

It has been also varied the value of the chlorine van der Waals radius parameter with respect to the force-field default one. This has been done in order to either assess our Pa's based model or to better reproduce the quantum mechanical geometrical parameters (interaction distances and angles). As the vdW parameter has been varied the well energy depth (the energy minimum for the vdW interaction) has been kept frozen to the chlorine default value equal to 0.265 kcal mol^{-1}.

These computations clearly prove that a lowering of the chlorine vdW radius parameter greatly improves the geometrical description of halogen bond, resulting in a better reproduction of the benchmark results. Also, this variation is fully consistent with a previous one made on bromine and iodine passing from the original Amber force field to the more recent one.[80]

The ACPYPE utility has been then exploited to pass the AMBER input files into the Gromacs ones. Hence, MM energy minimizations were carried out adopting Gromacs 5.0.7 package on all halogenated complexes either in the native form or after pseudo-atoms insertion for both Pa(s) dispositions. As computational protocol, 10000 steps of steepest descendent minimization, within 10 steps of conjugate gradient minimization for every step of steepest minimization, has been adopted.

Two figures of merit have been adopted to judge the MM energy minimization (em) results. They are the distance ($S_{distance}$) and angular (S_{angle}) percentage errors and are expressed by equations 1 and 2, respectively:

$$S_{\text{distance}} = \frac{|d_{em} - d_{DFT}|}{d_{DFT}} \qquad (1)$$

$$S_{\text{angle}} = \frac{|ang_{em} - ang_{DFT}|}{ang_{DFT}} \qquad (2)$$

where d_{em} and ang_{em} are the interaction distances and angles, respectively, obtained from the MM approach, while d_{DFT} and ang_{DFT} are the corresponding parameters obtained from M06-2X/6-311++G(d,p) (BSSE free) geometry optimization.

2.4 RESULTS AND DISCUSSION

In this project, ten chlorinated and one brominated systems (see Figure 1) have been studied performing Molecular Mechanics energy minimization calculations, with the aim of finding a new strategy to study chlorine halogen bond in the framework of classical force fields methods, as a result of the previously proposed methods.[20,21,72] As XB acceptor, the capped alanine has been chosen because of its representative structure that several times occurs in biological systems involving halogen bond.

The novelty of the approach here introduced relies on the introduction of a set of extra-point charges, called pseudo-atoms, Pa's, instead of a single one as already proposed for the description of heavier halogens XB (see Table 4 for an example).[20] The nature of the R groups has been selected to closely reproduce real halogenated ligands occurring in proteins, as underlined by a PBD survey.[81]

As mentioned previously, to benchmark the model systems, the BSSE-free M06-2X/6-311++G(d,p) optimized X···O distances and C–X···O angles have been used. Furthermore, to validate the strategy, several Pa's models have been considered by changing several parameters, such as the number of Pa's, their geometrical arrangements with respect to the central halogen and the vdW radius of the halogen itself. The case of no Pa has been as well considered. The geometrical disposition of the Pa's surrounding the halogen is depicted in Figure 2.

In the new Pa's scheme (Figure 2B), the central Pa is used to simulate the positive charge of the σ-hole, as in the previous model (Figure 2A), whereas the other four Pa's are exploited to reproduce the negative belt in the electrostatic potential around the halogen atom, as expected by the Politzer model.

As it is possible to observe from the ESP maps represented in Figure 3, the full set of extra-point charges are completely able to recover the quantum mechanical effect of the σ-hole, recurring to a classical method, differently to the no pseudo-atom case, which fails to recover the region of positive electrostatic charge on the halogen atom.

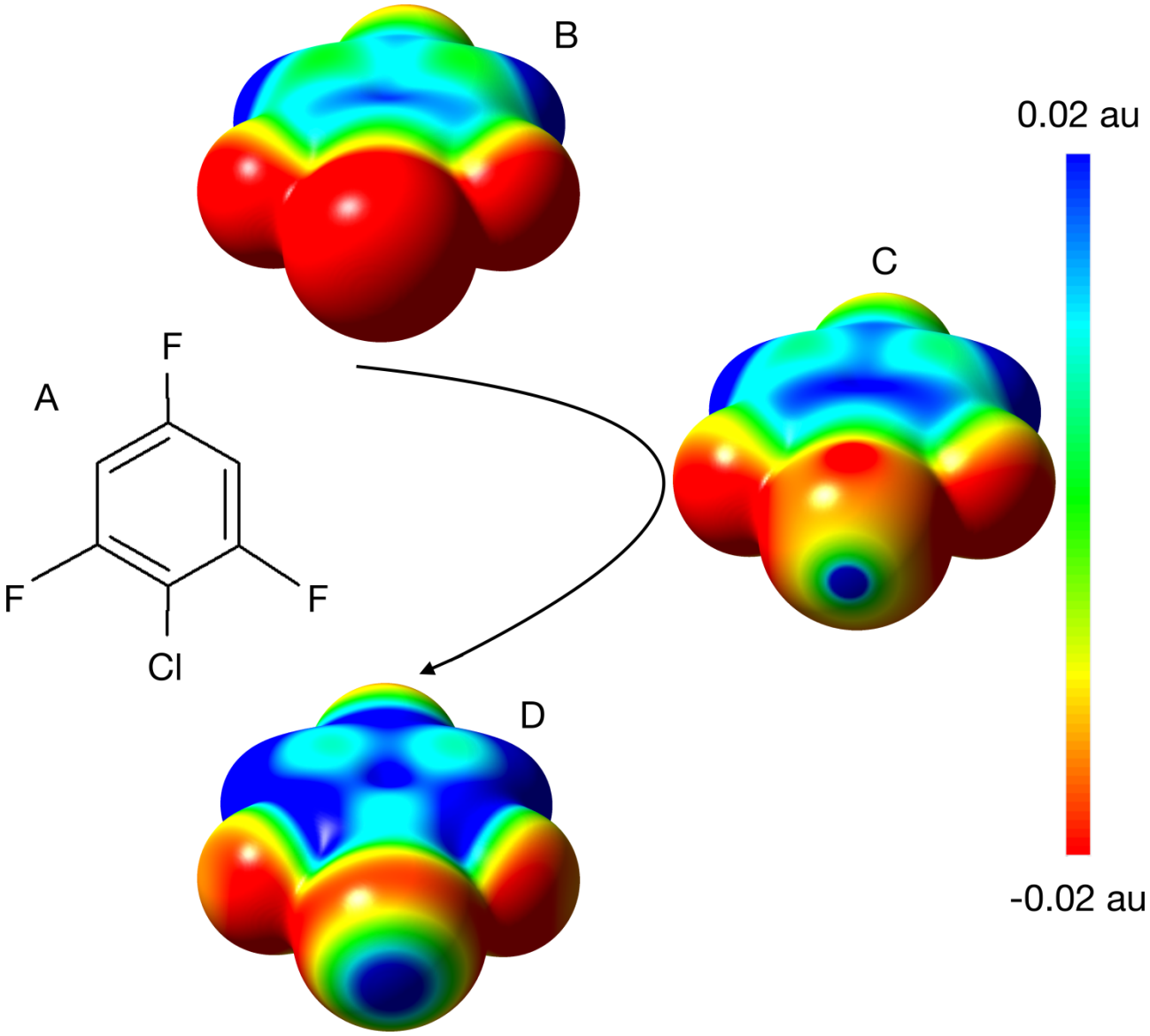

Figure 3. Electrostatic potential mapped onto the electron density surface (0.002 electrons au-3) of 1-chloro-2,4,6-trifluorobenzene (A), calculated at RHF/6-31G(d) level of theory (D) or using the RESP procedure without pseudo-atom(s) (B) and after five (C) pseudo-atoms addition at 1.8 Å from the chlorine atom.

Firstly, an important result of the present study is the following: for all the chlorinated systems the introduction of one or more Pa's allows to recover the XB interaction through classical energy minimization calculations, whilst the interaction is completely lost (meaningless geometrical parameters have been observed) if no pseudo-atom is added to the model (see Table 1 for results obtained on chlorobenzene using, as an example, 1.748 Å as vdW radius for chlorine and 1.8 Å as Cl–Pa(s) distance). Nevertheless, the addition of only one Pa, in most cases, results in completely misleading geometrical parameters, with respect to DFT results (see Figures 4 and 5-14, and Tables 2 and 3). This observation disagrees with what has been observed previously for brominated and iodinated systems,[20] pointing out the necessity for lighter halogens, as chlorine, to describe the ESP anisotropy in a more finer way, as an example, by introducing more than a single Pa. As a result of this observation, the '5Pa' strategy greatly improves the chlorine XB description, as demonstrated by a general lowering of the percentage errors associated with geometrical parameters.

The reason why '1Pa' approach fails in describing chlorine halogen bond by exploiting classical methods relies on the weakness of the chlorine halogen bonding with respect to the iodine and bromine ones, which is related to less intense σ-hole.

According to Hobza et al.,[72] the optimum distance of the pseudo-atom (explicit sigma hole, ESH, in their model) from the halogen should be shorter than the halogen vdW parameter to avoid numerical instabilities in simulations. On the other hand, it has been noted that placing the Pa too

close to the halogen could lead to an overestimation of the extra-point charge. Hence, it has been chosen to test the geometrical arrangements of the pseudo-atoms linked to chlorine by varying either their X–Pa length or the chlorine vdW parameters.

To accomplish our testing procedure, three different X–Pa distances (1.4, 1.6 and 2.0 Å) have been taken into account for both strategies (1Pa and 5Pa) and for all the vdW radius adopted, which has been varied from 1.95 Å, that is the default value, to 1.748 and 1.648 Å. The first modified vdW value (1.748 Å) has been chosen in order to reproduce the lowering of the same parameter of I and Br, passing to the new force field version. While, the second value (1.648 Å) has been tested to asses if the former lowering of Cl vdW parameter was enough.

As shown in Tables 2, 3 and in Figures 5 through 14, unfortunately it was not possible to highlight any trends in the behavior of the $S_{distance}$ and S_{angle} percentage errors upon variation of the X–Pa distances, denoting a sort of insensitiveness of the XB geometry with varying this parameter. However, it is easily observed that the chlorine GAFF VdW parameter is not suitable to correctly describe chlorine XB, because it brings almost always to the worst results (compared to the other two values: 1.748 and 1.648 Å). Therefore, it is evident the need for a re-parametrization of this parameter. This result is far more pronounced in the '5Pa' strategy with respect to the '1Pa' one, probably because in the latter the effect of a non-suitable vdW parameter is partially covered by the "noise" arising from a misleading description of the halogen ESP anisotropy.

As said above, the necessity to reduce the vdW radius with respect to the original GAFF default value, in order to correctly describe XB, was already evidenced for bromine and iodine, whose vdW radii have been in fact modified from 2.22 to 2.02 Å (Br) and from 2.35 to 2.15 Å (I) passing from the original[78] to the improved version of the force field.[80] Both of the new shorter GAFF vdW radii here tested for chlorine allow to improve the results obtained for all the model systems

studied, though no systematic differences are observed passing from 1.748 to 1.648 Å. This conclusion doesn't claim to be a rigorous re-parametrization of the chlorine GAFF vdW radius but it suggests that the present default value should be revised in future GAFF force field versions.

It is worth noting that the RESP procedure provides, as expected, a positive charge for the central Pa representing the σ-hole, whilst it results in negative charges for the 'lateral' Pa's of all chlorinated ligands or positive charges for bromobenzene (see Tables 5 and 6). This result is in good agreement with the charge density investigation carried out by Espinosa et al.,[82] that analyzed the difference between the chlorine and bromine σ-hole "architectures" based on the survey of the Laplacian of electron density, $\nabla^2\rho(r)$, for a series of halogenated derivatives. From the analysis it could be clearly devised that for chlorine it is possible to observe an extended valence shell charge concentration (VSCC) region, containing either the charge concentration (CC) or charge depletion (CD) sites, while for bromine a far more reduced VSCC region is observed, containing only the CC sites, while the CD sites belong to a large region of positive $\nabla^2\rho(r)$ (which corresponds to a large portion of positive electrostatic potential) surrounding the bromine atom. This topology of $\nabla^2\rho(r)$ agrees with the previous observation relative to bromobenzene, having positive RESP charge values of the four lateral Pa's. Moreover, it could be the reason why the '5Pa' arrangement results mandatory to correctly describe chlorine halogen bonding. Indeed, the use of only a single extra-point charge in the position of the σ-hole may induce an underestimation of the electrostatic charge related to the σ-hole (because of the extended VSSC region). Then, by introducing the other four lateral Pa's, with the aim of describing the "negative belt" of the ESP anisotropy around the halogen atom, the charge of the central Pa fits more closely the real σ-hole charge derived from QM calculations.

The inadequacy of exploiting only one extra-point charge in the description of the σ-hole was underlined also by Hage et al.[83] Particularly, his observation on the need of the quadrupolar contribution to better reproduce thermodynamic properties of halogen bonding (in particular for lighter halogens) by using hybrid (PC/MTP) approaches would help to corroborate the '5Pa' model here proposed.

Table 1. Halogen bonding interaction distances and angles for the chlorobenzene-capped alanine dimer, computed with molecular mechanics using 0, 1 and 5 pseudo-atoms and with M06-2X/6-311++G(d,p) geometry optimization.

Chlorobenzene	Distance/Å	Angle/°
No Pseudo-atom	Lost	Lost
1 Pseudo-atom	3.02	169.97
5 Pseudo-atoms	3.24	161.14
M06-2X/6-311++G(d,p)	3.17	160.11

MM calculations performed using 1.748 Å as VdW parameter for the chlorine atom and 1.8 Å as Pa(s) distances from chlorine.

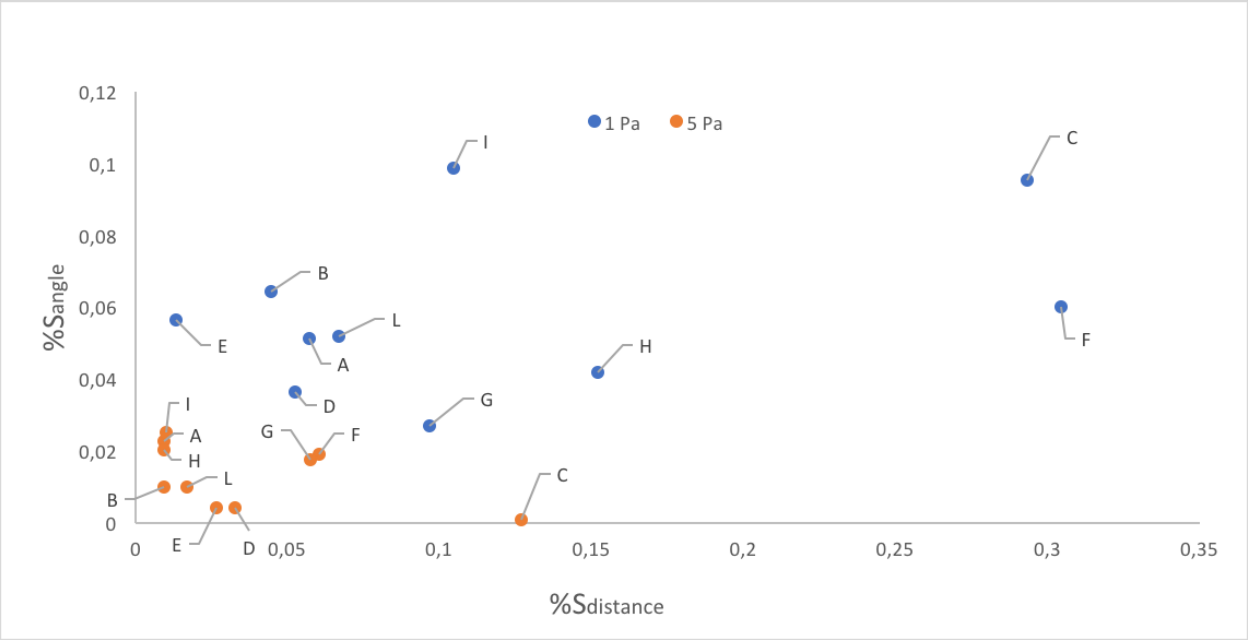

Figure 4. Percentage errors on halogen bonding distances (x-axis) and angles (y-axis), for the ten chlorinated systems studied in this work. '5Pa' strategy in red, '1Pa' strategy in blue (calculations performed using 1.748 Å as vdW parameter for the chlorine atom and 2.0 Å as Pa(s) distances from the central halogen).

Table 2. Halogen bonding interaction distances (Å, first column for each system) and angles (°, second column for each system) for complexes A÷E with alanine. These results have been reported for all the vdW parameters and Cl–Pa distances tested and for both 1Pa and 5Pa strategies.

vdW (Å)		X-Pa (Å)	**A**		**B**		**C**		**D**		**E**	
			dist	angle	dist	angle	dist	angle	dist	angle	Dist	angle
1.748	1Pa	2.0	2.96	173.98	3.00	174.07	3.97	144.50	3.21	175.04	3.03	169.00
		1.8	3.02	169.97	3.14	171.11	3.77	138.26	2.97	174.31	3.08	165.07
		1.6	3.10	160.00	3.02	170.19	3.92	126.99	3.03	173.88	3.12	161.75
		1.4	3.19	152.08	3.24	166.89	3.94	126.77	3.08	142.48	3.14	160.25
	5Pa	2.0	3.17	161.74	3.17	165.17	3.46	159.63	3.15	169.56	3.07	160.66
		1.8	3.24	161.14	3.19	163.96	3.29	160.59	2.94	170.35	3.05	160.48
		1.6	3.21	160.31	3.19	164.06	3.37	159.80	2.96	169.55	3.09	160.09
		1.4	3.21	160.73	3.19	163.84	3.32	160.26	2.98	169.27	3.09	159.12

1.648	1Pa	2.0	2.75	176.89	2.76	176.56	3.68	146.47	2.73	177.63	2.82	172.88
		1.8	2.87	173.01	2.91	172.95	3.52	144.83	2.84	175.44	2.93	168.10
		1.6	2.95	167.98	2.86	171.83	3.64	128.87	2.91	174.36	2.99	165.37
		1.4	3.02	156.96	3.09	168.61	3.68	127.92	2.96	174.13	3.01	162.29
	5Pa	2.0	3.11	162.55	3.10	165.96	3.42	160.87	3.05	169.87	2.99	161.66
		1.8	3.20	161.65	3.11	164.71	3.24	161.34	2.84	170.65	2.99	160.46
		1.6	3.15	160.79	3.12	165.12	3.31	160.49	2.87	170.18	3.00	160.41
		1.4	3.16	160.49	3.13	164.43	3.28	160.90	2.90	169.75	3.03	159.37
1.948	1Pa	2.0	3.45	154.57	3.45	168.26	4.25	137.87	3.21	175.04	3.03	169.00
		1.8	3.45	151.96	3.47	166.67	4.05	134.50	3.23	173.19	3.39	155.60
		1.6	3.47	147.07	3.52	165.00	4.10	122.06	3.29	168.51	3.12	161.75
		1.4	3.49	143.05	3.56	163.49	4.13	120.66	3.36	162.11	3.14	160.25
	5Pa	2.0	3.34	159.30	3.33	163.00	3.58	157.96	3.35	168.05	3.07	160.66
		1.8	3.36	159.00	3.31	163.04	3.42	159.02	3.13	169.43	3.20	158.60
		1.6	3.34	158.71	3.33	162.60	3.49	157.79	3.15	168.18	3.09	160.09
		1.4	3.34	158.58	3.33	162.08	3.42	158.26	3.15	168.48	3.09	159.12
M06-2X/6-311++G(d,p)			3.14	165.51	3.14	163.56	3.07	159.76	3.05	168.88	2.99	159.99

Table 3. Halogen bonding interaction distances (Å, first column for each system) and angles (°, second column for each system) for complexes F÷L with alanine. These results have been reported for all the vdW parameters and Cl–Pa distances tested and for both 1Pa and 5Pa strategies.

VdW (Å)		X-Pa (Å)	**F**		**G**		**H**		**I**		**L**	
			dist	angle	dist	angle	dist	angle	dist	angle	dist	angle
1.748	1Pa	2.0	4.33	157.99	3.69	170.49	3.64	169.27	2.79	180.09	2.84	177.53
		1.8	4.33	157.49	3.66	168.22	3.99	164.12	2.88	179.10	2.92	176.06
		1.6	4.59	152.88	3.82	164.88	4.22	164.45	2.93	177.53	2.96	174.36
		1.4	4.64	151.91	3.87	163.02	4.34	163.25	3.00	175.65	3.00	172.84

	5Pa	2.0	3.12	171.31	3.17	168.90	3.13	165.73	3.14	168.04	2.99	170.49
		1.8	3.12	169.84	3.19	169.64	3.20	163.42	3.20	166.15	3.05	170.19
		1.6	3.13	169.52	3.25	167.77	3.16	163.24	3.17	166.25	3.08	169.51
		1.4	3.15	169.10	3.25	168.04	3.20	162.07	3.18	165.78	3.09	168.90
1.648	1Pa	2.0	2.99	167.75	3.46	175.65	2.71	178.07	2.57	180.09	2.66	180.09
		1.8	3.55	159.64	3.59	170.94	3.59	170.94	2.72	179.30	2.78	176.16
		1.6	4.32	153.23	3.71	167.51	3.70	169.01	2.81	180.09	2.84	174.36
		1.4	4.49	151.03	3.77	164.45	4.05	165.51	2.86	177.53	2.89	172.84
	5Pa	2.0	3.03	171.72	3.11	169.51	3.05	166.31	3.06	168.61	2.85	172.39
		1.8	3.05	169.76	3.15	169.88	3.15	169.88	3.15	166.61	2.98	170.25
		1.6	3.04	170.00	3.20	168.61	3.08	164.19	3.11	166.74	3.00	170.15
		1.4	3.07	169.60	3.20	168.61	3.16	162.60	3.13	165.78	3.02	168.61
1.948	1Pa	2.0	4.78	155.61	3.99	162.26	4.80	160.31	3.11	177.53	3.13	175.65
		1.8	4.75	156.07	3.91	161.85	3.91	161.85	3.16	176.01	3.16	174.79
		1.6	4.79	153.56	4.02	159.63	3.70	169.01	3.21	173.81	3.18	173.81
		1.4	4.81	152.68	4.03	158.83	4.78	161.22	3.27	171.20	3.21	173.30
	5Pa	2.0	3.32	169.69	3.31	166.49	3.32	162.84	3.31	166.01	3.21	168.04
		1.8	3.30	168.70	3.32	167.39	3.32	167.39	3.33	164.50	3.21	168.44
		1.6	3.32	168.56	3.37	165.78	3.30	161.74	3.30	165.32	3.24	168.32
		1.4	3.32	168.11	3.36	166.01	3.35	160.10	3.30	164.88	3.24	169.99
M06-2X/6-311++G(d,p)			3.14	169.35	3.16	168.86	3.16	162.45	3.11	163.91	3.04	168.79

Table 4. Halogen bonding interaction distance (Å) and angle (°) for bromobenzene-alanine complex. The first row refers to energy minimization performed using molecular mechanics as described in the methodology section, while the second row refers to M06-2X/6-311++G(d,p) calculation.

	Bromobenzene_alanine	
	distance	angle
MM	3.51	155.69
M06-2X/6-311++G(d,p)	3.53	155.49

Table 5. Selected RESP derived atomic point charges (in amu) in chlorobenzene: Carbon linked to chlorine, chlorine, pseudo-atom representing the σ-hole and the four lateral pseudo-atoms. 1.8 Å as Pa(s) distances from chlorine have been used.

	C	Cl	'σ-hole' Pa	Pa	Pa	Pa	Pa
No Pa	-0.01	-0.13	-	-	-	-	-
1 Pa	0.02	-0.15	0.01	-	-	-	-
5 Pa	0.30	-0.23	0.04	-0.01	-0.01	-0.01	-0.01

Table 6. Selected RESP derived atomic point charges (in amu) in bromobenzene: Carbon linked to bromine, bromine, pseudo-atom representing the σ-hole and the four lateral pseudo-atoms. 1.8 Å as Pa(s) distances from chlorine have been used.

	C	Br	'σ-hole' Pa	Pa	Pa	Pa	Pa
No Pa	-0.12	-0.09	-	-	-	-	-
1 Pa	0.20	-0.30	0.06	-	-	-	-
5 Pa	0.15	-0.32	0.03	0.02	0.02	0.02	0.02

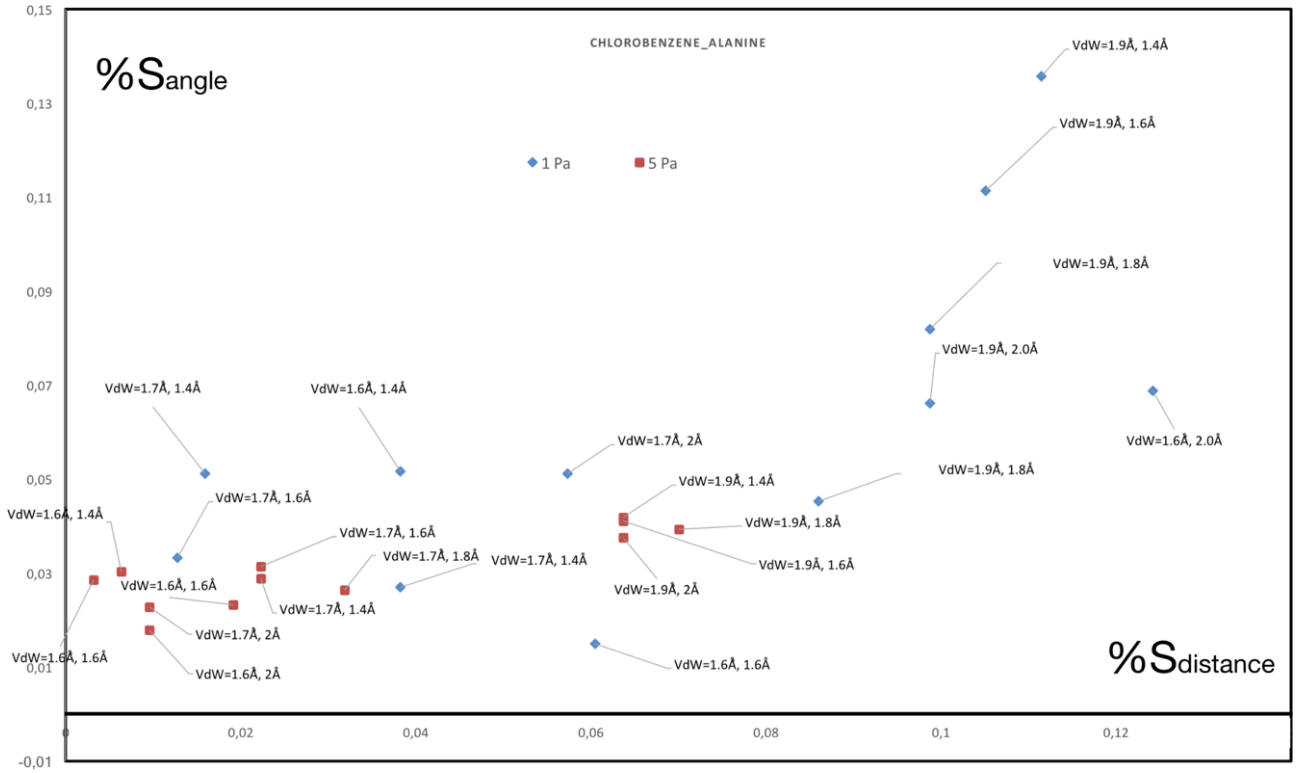

Figure 5. Chlorobenzene···alanine percentage errors on halogen bonding distances and angles on y and x-axis respectively. '5Pa(s)' strategy in red. '1Pa' strategy in blue.

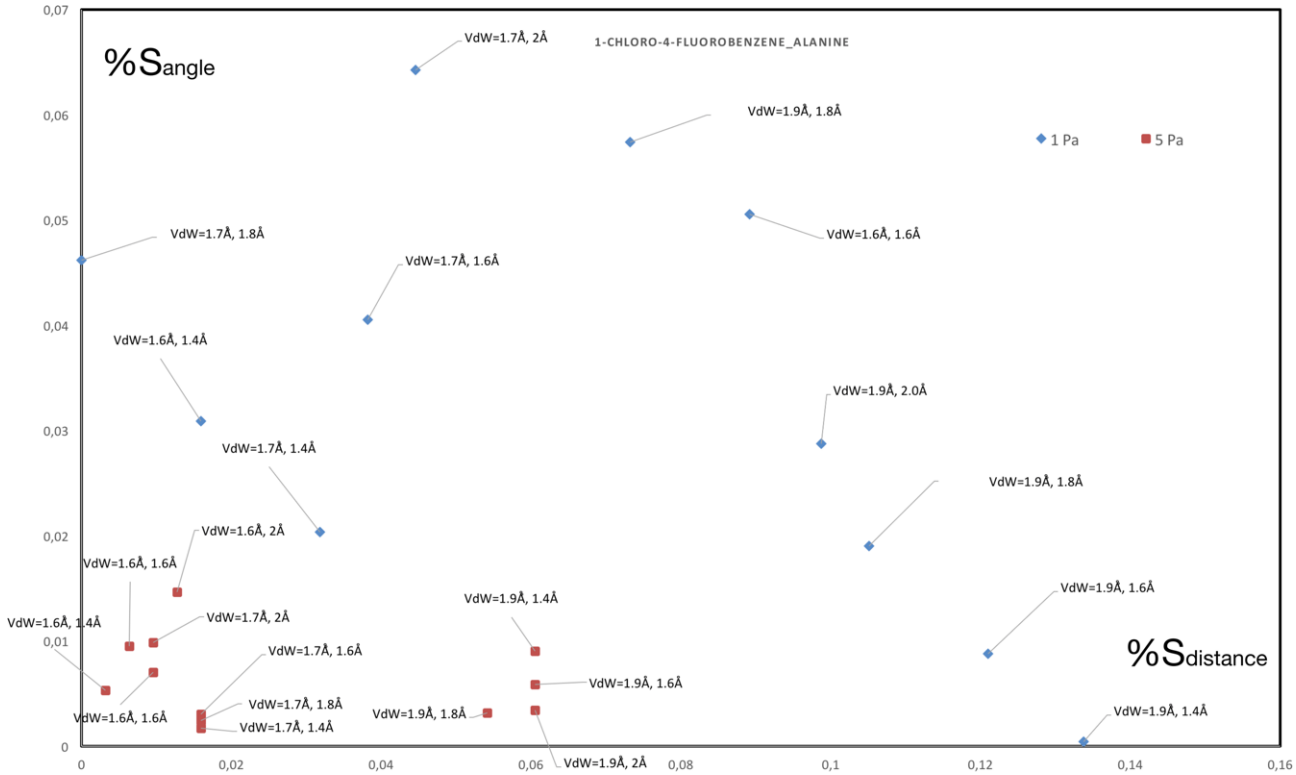

Figure 6. 1-chloro-4-fluorobenzene···alanine percentage errors on halogen bonding distances and angles on y and x-axis respectively. '5Pa(s)' strategy in red. '1Pa' strategy in blue.

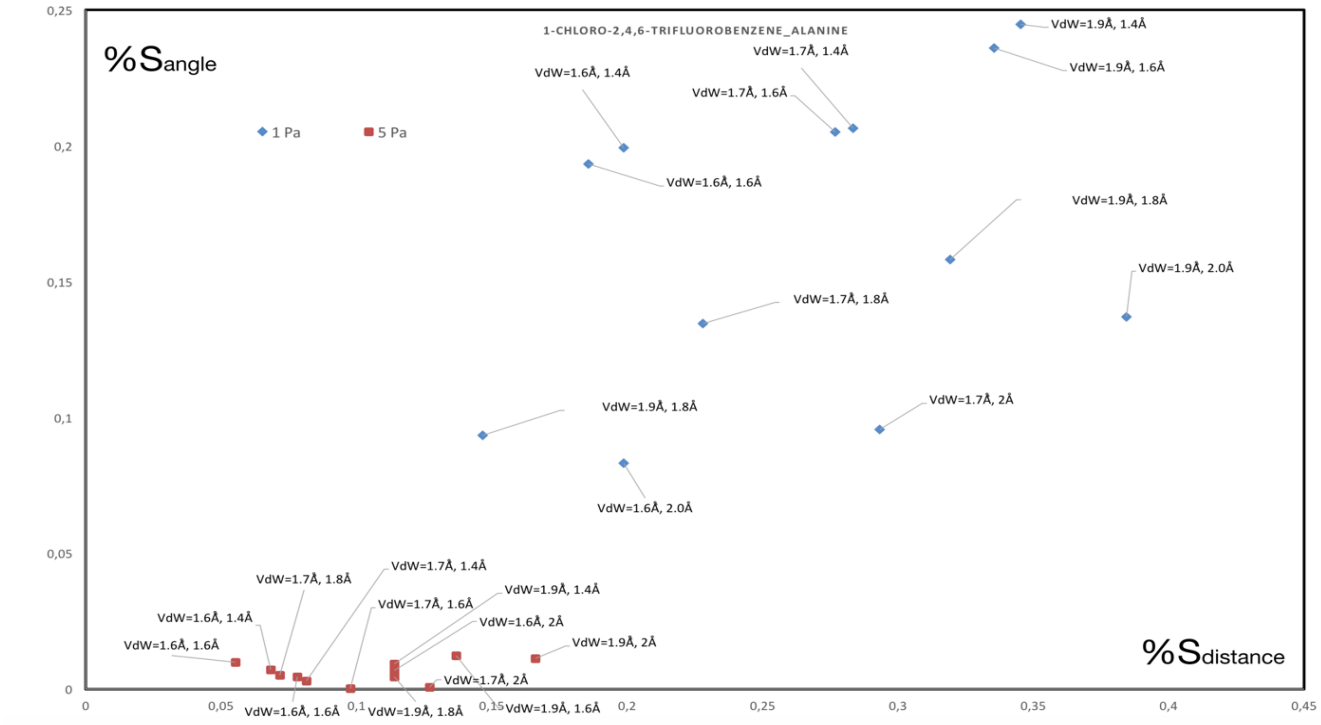

Figure 7. 1-chloro-2,4,6-trifluorobenzene···alanine percentage errors on halogen bonding distances and angles on y and x-axis respectively. '5Pa(s)' strategy in red. '1Pa' strategy in blue.

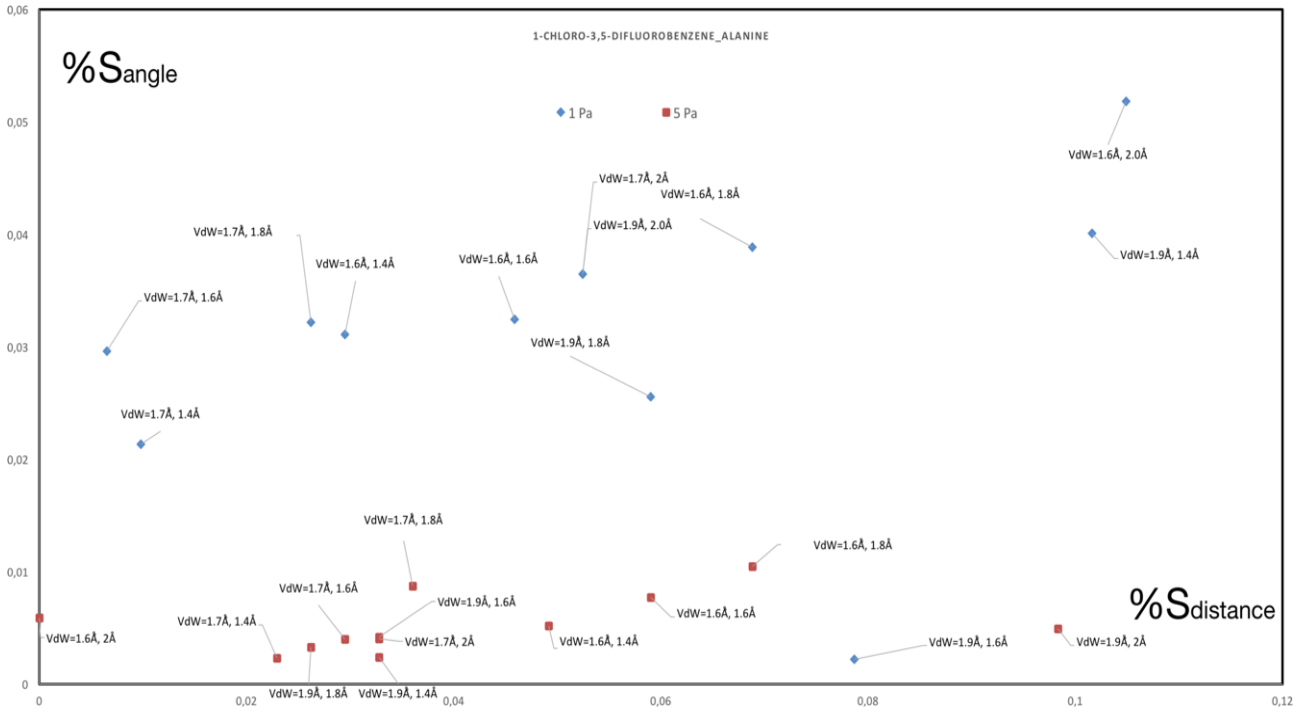

Figure 8. 1-chloro-3,5-difluorobenzene···alanine percentage errors on halogen bonding distances and angles on y and x-axis respectively. '5Pa(s)' strategy in red. '1Pa' strategy in blue.

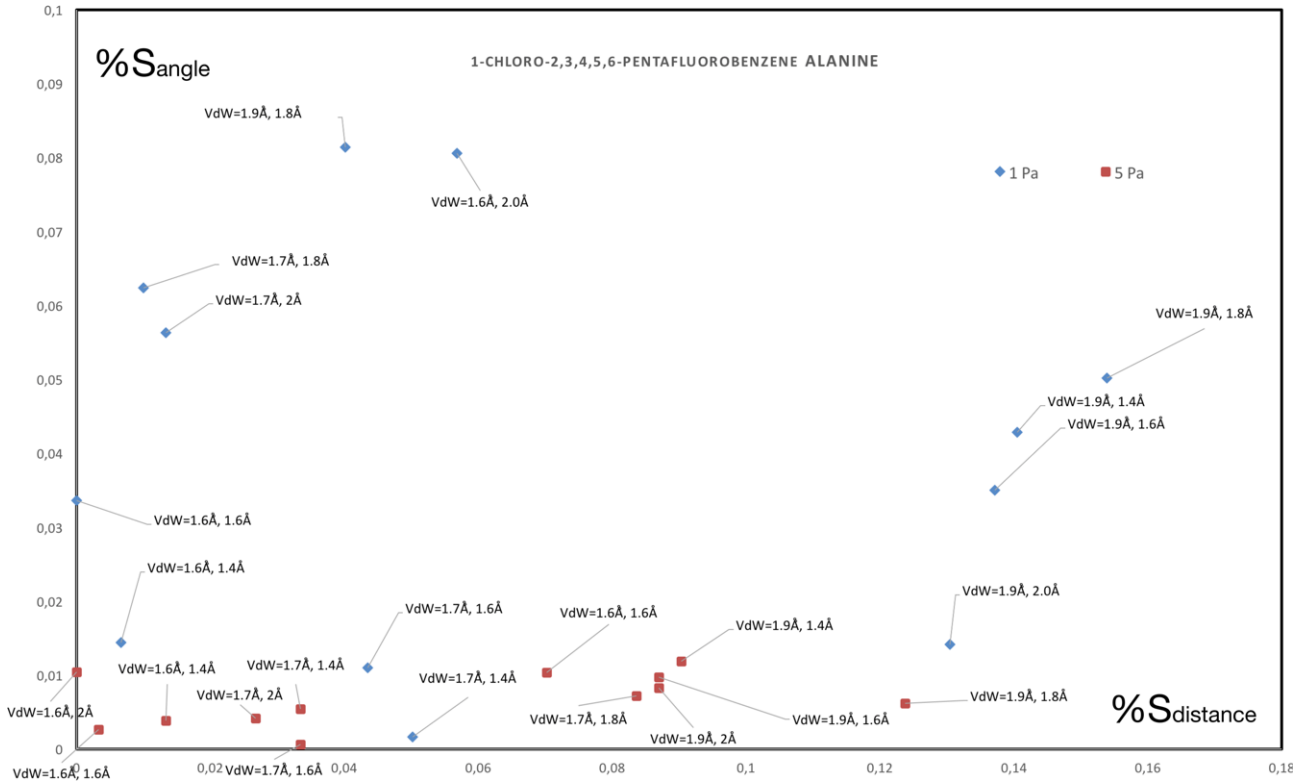

Figure 9. 1-chloro-2,3,4,5,6-pentafluorobenzene···alanine percentage errors on halogen bonding distances and angles on y and x-axis respectively. '5Pa(s)' strategy in red. '1Pa' strategy in blue.

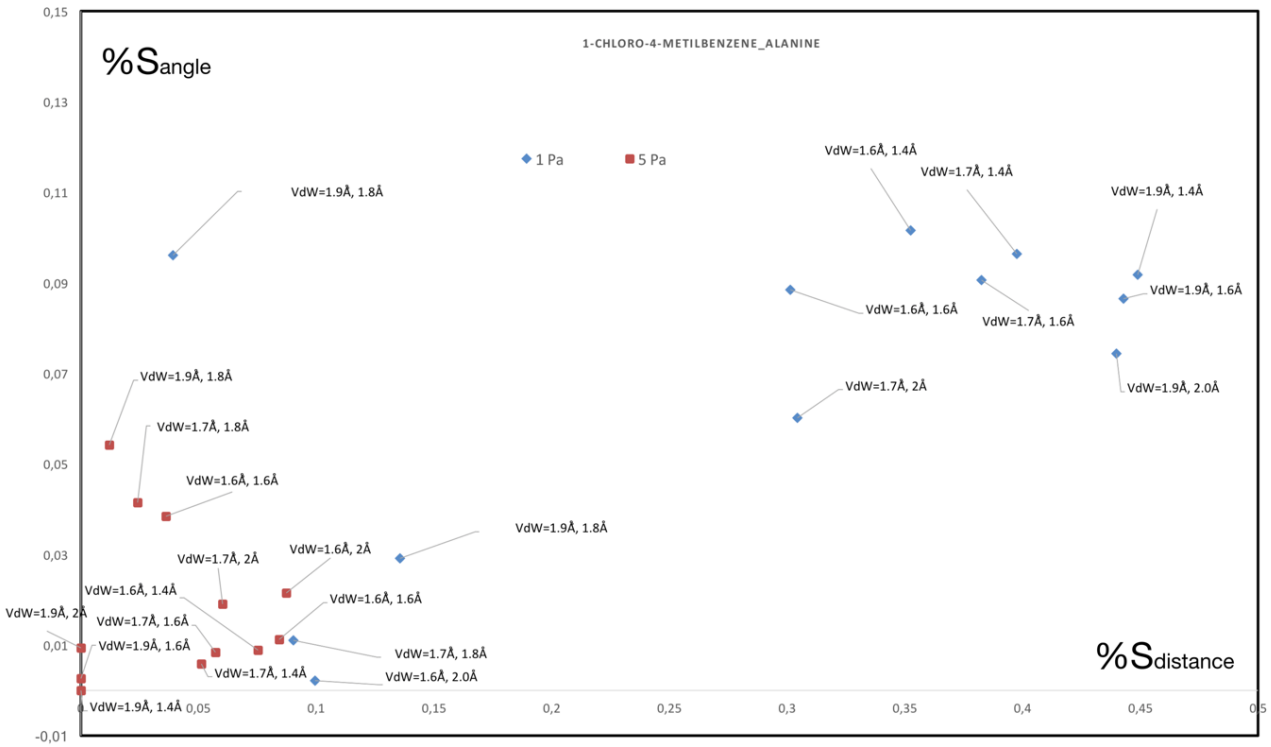

Figure 10. 1-chloro-4-metilbenzene···alanine percentage errors on halogen bonding distances and angles on y and x-axis respectively. '5Pa(s)' strategy in red. '1Pa' strategy in blue.

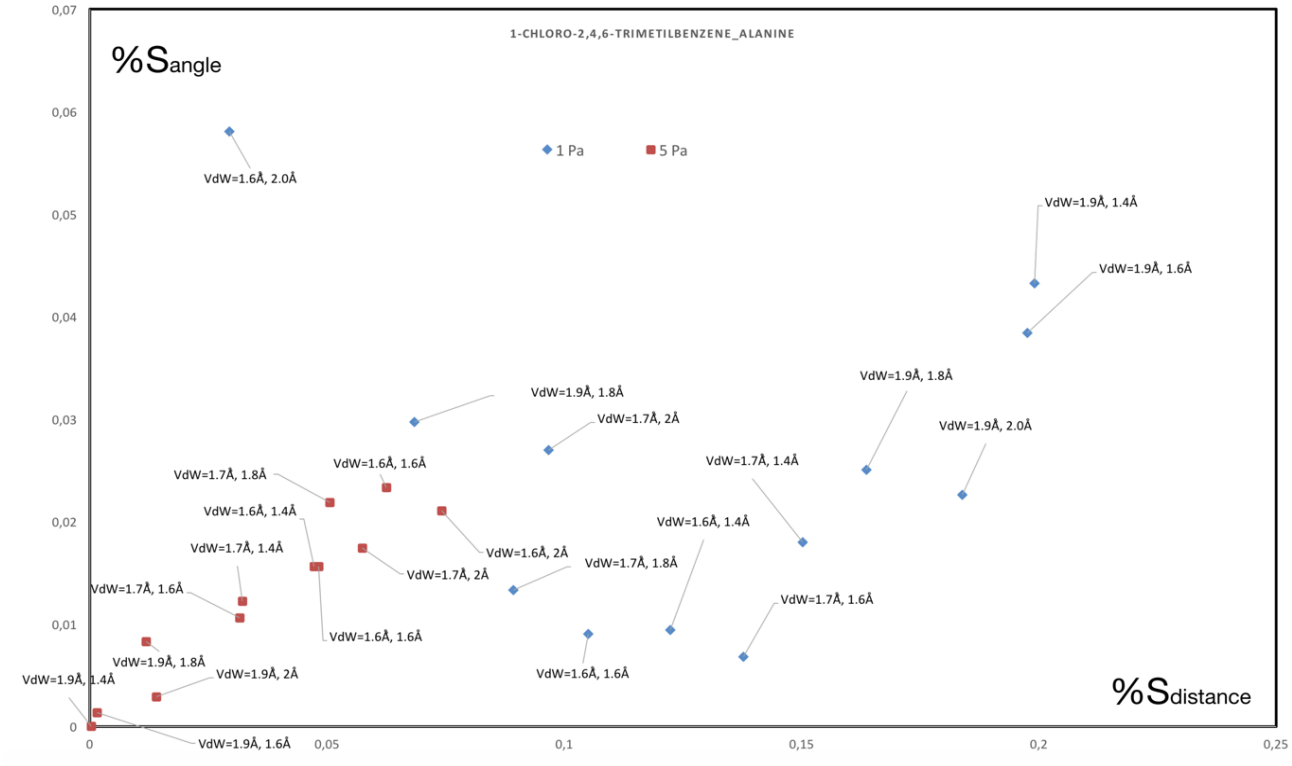

Figure 11. 1-chloro-2,4,6-trimetilbenzene···alanine percentage errors on halogen bonding distances and angles on y and x-axis respectively. '5Pa(s)' strategy in red. '1Pa' strategy in blue.

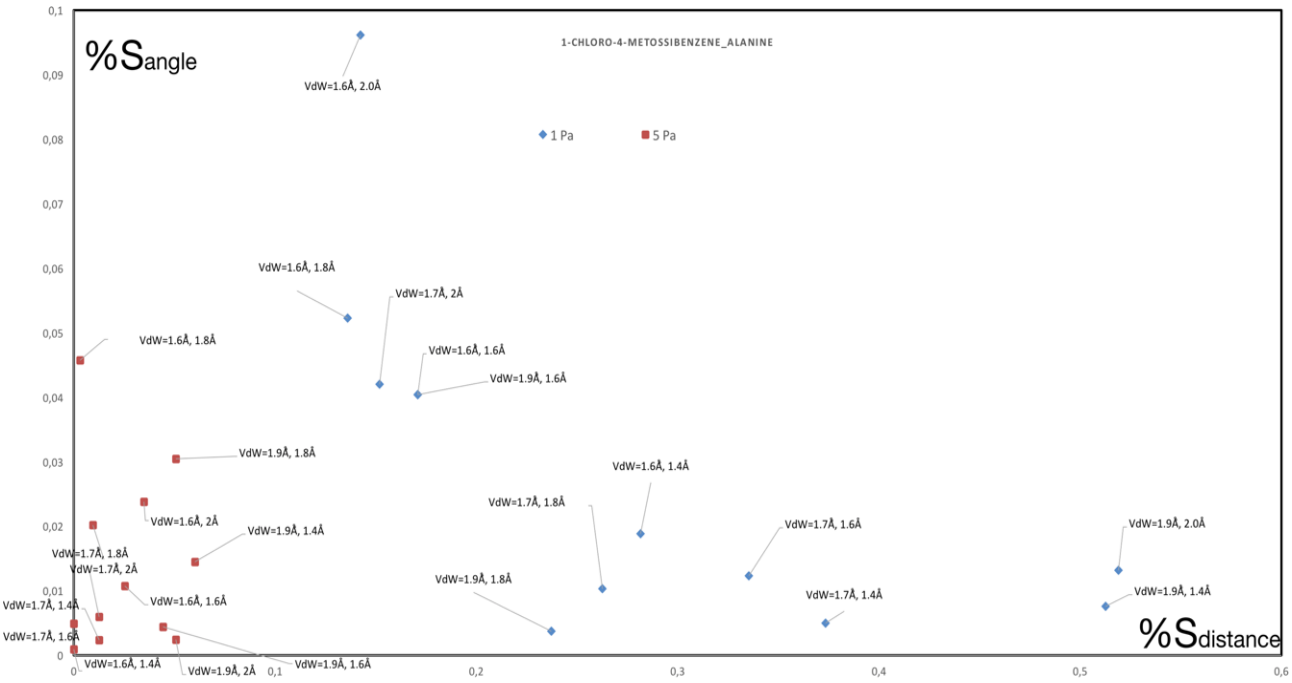

Figure 12. 1-chloro-4-metossibenzene···alanine percentage errors on halogen bonding distances and angles on y and x-axis respectively. '5Pa(s)' strategy in red. '1Pa' strategy in blue.

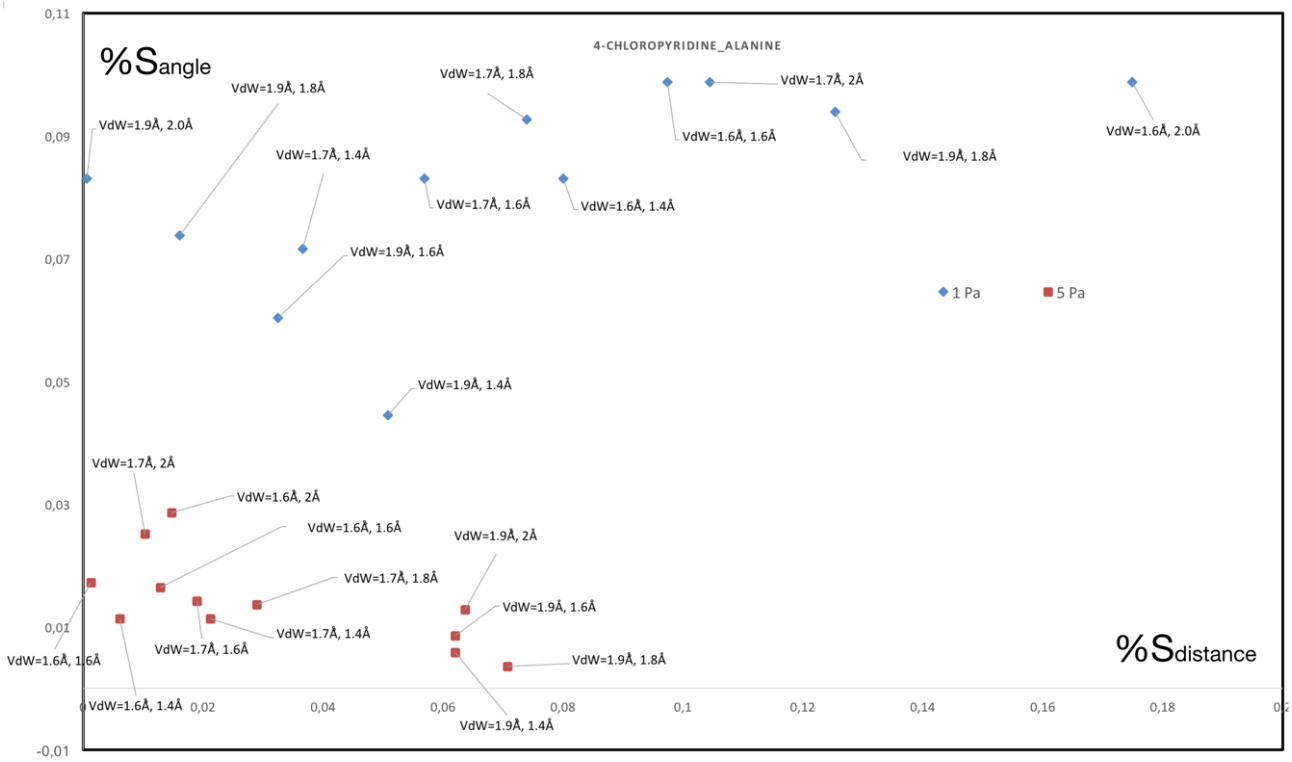

Figure 13. 4-chloropyridine···alanine percentage errors on halogen bonding distances and angles on y and x-axis respectively. '5Pa(s)' strategy in red. '1Pa' strategy in blue.

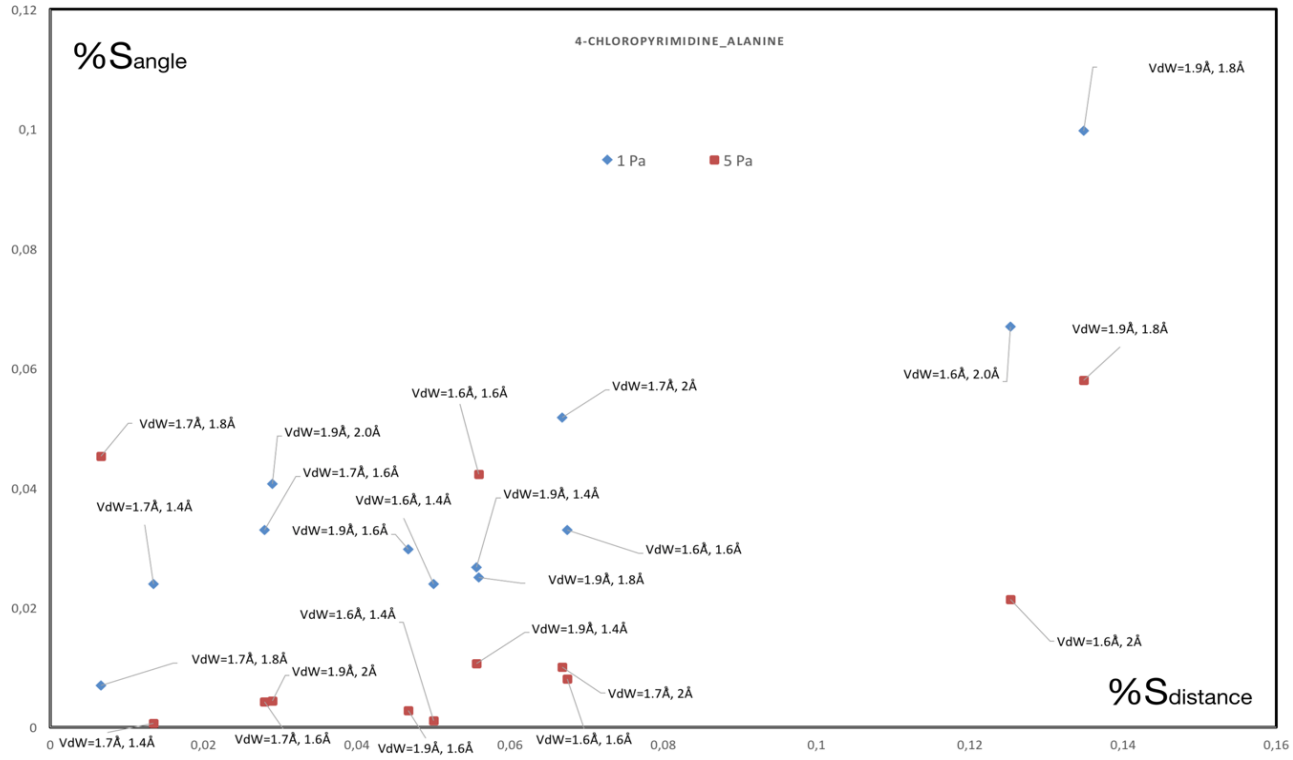

Figure 14. 4-chloropyrimidine···alanine percentage errors on halogen bonding distances and angles on y and x-axis respectively. '5Pa(s)' strategy in red. '1Pa' strategy in blue.

2.5 CONCLUSIONS

A set of halogenated molecules (principally chlorinated), specifically chosen to reproduce real halogenated ligands occurring in biological systems, have been studied by performing molecular mechanics energy minimizations exploiting extra-point charges (pseudo-atoms) to simulate the σ-hole and the negative "belt" of electrostatic potential surrounding the halogen atom.

Rather than the pseudo-atom ('1Pa') approach adopted so far to describe brominated and iodinated molecules, the '5Pa' method has been developed to better reproduce quantum mechanical geometrical parameters, such as interaction angle and distances, of chlorinated model systems, which requires a finer description of the electrostatic potential with respect to the brominated or iodinated ones. As halogen bond acceptor, the carbonyl oxygen of the capped alanine has been selected thanks to its occurrence in proteins.

Hence, both halogen bond donor and acceptor have been chosen to either reproduce real systems that are likely to be encountered in PDB or to test the strategy to a rather extended range of XB strengths.

The improvement of the multi-pseudo-atom approach, in the description of chlorine halogen bond by classical methods, is very evident from the comparison of MM results with either the 1Pa or "naked" halogen strategies.

Particularly, this improvement is evident from the lowering of the percentage errors associated with the interaction distances and angles, as referred to benchmark M06-2X/6-311++G(d,p) geometry optimizations, when going from the '1Pa' to the '5Pa' methodology. The same improvement was not observed in the case of bromobenzene, suggesting the correctness of the '1Pa' strategy in the description of halogen bonding when bromine atoms are involved.

Moreover, it has been demonstrated (through testing of different vdW radius values) that a re-parametrization of the chlorine GAFF van der Waals radius should be considered to improve XB description by means of classical force field.

Further development of this methodology will comprehend either testing our Pa's strategy on other model compounds (including different halogen bond acceptor) or performing molecular dynamics simulations on condensed phase systems (like complexes between proteins and chlorinated ligands).

3. SPIN-COUPLED STUDY OF HALOGEN BOND

3.1 INTRODUCTION

As mentioned in the introduction section, to the best of our knowledge, the theoretical models used to describe halogen bond relies on theories and calculations almost exclusively performed in the framework of Molecular Orbital (MO)-based techniques. Valence Bond (VB) strategies (and in particular the Spin-Coupled method) have been seldom exploited to get insight into such an interaction,[84] although, as a result of their intrinsic "chemical nature", they could provide deep understanding of the halogen bond features and of the essential attributes of the σ-hole. Indeed, in all VB techniques, molecular electronic structure is described in terms of orbitals that are mainly localized on atoms and that significantly overlap when bonding interactions occur, thus preserving the traditional chemical picture of bond as schematically depicted through the well-known Lewis molecular structures. Despite VB calculations are very time consuming, in the last years a "renaissance" of valence bond methods is taking place, as pointed out by Shaik.[85] On the contrary, this traditional description is completely lost in all those computational strategies based on MOs since, in general, the obtained orbitals are completely delocalized on the whole molecular system under exam. Several efforts have been made to recover traditional chemical concepts (e.g., bond, lone-pairs and resonance structures) also from MO-based calculations, by obtaining orbitals which are inherently localized on atoms or functional groups. For example, it is worth mentioning the a posteriori methods,[86–89] which allow the determination of Localized Molecular Orbitals (LMOs) as unitary transformation of canonical Hartree-Fock MOs, or the a priori techniques,[90,91,100,92–99] which exploit user-defined and chemically meaningful localization schemes to compute MOs that are extremely localized on small molecular fragments (atoms, bonds or functional groups) and that are easily transferable from a molecule to another. Attempts of exploiting localized MOs in a

Valence Bond way were also proposed[101–105] but, despite all these efforts, pure VB approaches remain the theoretical methods closest to traditional chemical concepts, although they are more computationally expensive than those based on MOs, as pointed out previously.

Therefore, in this chapter one of the first VB-based investigations on the nature of halogen bond is presented. To this aim, we have decided to exploit a particular Valence Bond strategy, the spin-coupled (SC) method,[106–108] the theoretical features of which will be briefly described in the next section. In particular, SC calculations have been performed by first on isolated halogenated molecules. As a result of this survey, it has been possible to draw some conclusions and find out remarkable results on the inherent nature of the σ-hole from a VB perspective, together with the variation of the σ-hole intensity by varying the functional group directly linked to the halogen.

Then, since it would be appealing to see the σ-hole "at work" (in terms of singly occupied SC orbitals), molding the halogen bond itself, Spin-Coupled calculations have been carried out on different RBr···NH_3 interacting dimers (R = –H, HCC–, –CN). In such dimers, halogen bond occurs between the ammonia lone pair (that behaves as a halogen bond acceptor, following the scheme proposed in the introduction chapter) and the bromine, that acts like the XB donor. In this way it was possible to draw conclusions about the formation and the strength of the halogen bond in the different cases in terms of spin-coupled orbitals, their overlaps and weights of the spin-coupled structures. The bromine has been chosen as a case study, on one hand, due to its σ-hole intensity (greater than the chlorine one and far more intense than that of fluorine) and, on the other hand, because it is easier to model than iodine from a computational point of view. Finally, the obtained results have been discussed in connection with the Politzer and the lump-hole models mentioned in the introduction chapter of this thesis, showing not only that VB calculations fully confirm them but that another interesting feature of the σ-hole could be devised from the behavior of the SC

orbitals. Indeed, one conclusion of the present investigation is that, from a valence-bond point of view, σ-hole could be actually seen as a σ-tunnel.

3.2 THEORETICAL BACKGROUND

Valence bond is one of the two main quantum chemical theories, together with the Molecular Orbitals one, which are exploited to theoretically study the nature of chemical bond.

Particularly, in this project the spin-coupled theory has been exploited. SC is a technique that describe the electronic structure of an N-electrons system using N non-orthogonal, singly occupied, orbitals. These orbitals can, eventually, couple and overlap together in different manners, to form what is called chemical bond.

As a result of what stated above, the wave function (ψ) for a system of N electrons is expressed by using non-orthogonal singly occupied SC orbitals that can interact by overlapping between themselves.

Owing to the non-orthogonality and the single occupancy of these spin-coupled orbitals there are, beside the case of 2 electrons, several modes for coupling the individual N electrons spin to obtain, as a result of the association, the total spin of the system (S). These modes of spin coupling correspond to different spin-coupled structures (always covalent). In particular, it is possible to show that, in case of a system of N electrons with total spin S, for each value M of the projection of S, we can write f_S^N linear independent spin-coupled structures (and spin-eigenfunctions), where f_S^N is defined as:

$$f_S^N = \frac{(2S+1)N!}{\left(\frac{1}{2}N+S+1\right)!\left(\frac{1}{2}N-S\right)!} \quad (1)$$

Consequently, by associating each possible spin-coupled structure with a particular N-electron function $\psi_{S,M;k}^N$, the global SC wave function for a system of N electrons in a spin-state (S, M) can be expressed as follows:

$$\psi_{SC}^{S,M} = \sum_{k=1}^{f_S^N} c_{Sk}\, \psi_{S,M;k}^{N} = \sum_{k=1}^{f_S^N} c_{Sk} \mathcal{A}\left(\Phi\, \Theta_{S,M;k}^{N}\right) \qquad (2)$$

where $\mathcal{A}$ is the antisymmetrizing operator, $\Theta_{S,M;k}^{N}$ is the k-th spin-eigenfunction for the N-electron system in the spin-state (S, M), Φ is the product of N spatial functions $\{\phi_i\}_{i=1}^{N}$ (namely, the spin-coupled orbitals)

$$\Phi\,(\mathbf{r}_1, \mathbf{r}_2, \ldots \mathbf{r}_N) = \phi_1(\mathbf{r}_1)\, \phi_2(\mathbf{r}_2) \ldots \phi_N(\mathbf{r}_N) \quad (3),$$

and $c_{S,k}$ are the spin-coupling coefficients that are used to weight the importance of each spin-coupled structure in the wave function $\psi_{SC}^{S,M}$. Since the spin-coupling orbitals are not orthogonal, in order to have an estimation of the importance of each structure in the wave-function the overlap between these structures has to be considered. A possible strategy consists in the determination of the Chirgwin-Coulson coefficients[109] defined as:

$$w_{S,k} = \left|c_{S,k}\right|^2 + \sum_{j \neq k}^{f_S^N} c_{S,k}\, c_{S,j}\, S_{kj} \quad (4)$$

with S_{kj} as the overlap integral between the spin-coupled structures $\psi_{S,M;k}^{N}$ and $\psi_{S,M;j}^{N}$.

It is worth noting that, to reduce the computational cost associated with the spin-coupled calculations (which otherwise would be prohibitive), a partition of the N electrons of the systems into two distinguished groups is advisable: a subset of $2N_1$ core electrons and a subset of N_v valence electrons. The former are described by frozen doubly occupied Molecular Orbitals previously obtained by means, as in our case, of a proper Hartree-Fock computation on the system under exam, while the latter are the ones that are treated at spin-coupled level. Therefore, after this partition, the spin-coupled wave function can be written as shown in the following equation:

$$\psi_{SC}^{S,M} = \sum_{k=1}^{f_S^{N_v}} c_{Sk}\, \psi_{S,M;k}^{N} = \sum_{k=1}^{f_S^{N_v}} c_{Sk}\, \mathcal{A}\left(\phi_1^c\, \overline{\phi}_1^c \ldots \phi_{N_1}^c\, \overline{\phi}_{N_1}^c\, \Phi_v\, \Theta_{S,M;k}^{N_v}\right) \qquad (5)$$

where c_{Sk} and $\mathcal{A}$ have the same meaning as the one seen for equation (2), ϕ_i^c is a frozen "core spin-orbital" with spatial part ϕ_i^c and spin part α, $\overline{\phi}_i^c$ is a frozen "core spin-orbital" with spatial part ϕ_i^c and spin part β, $\Theta_{S,M;k}^{N_v}$ is the k-th spin-eigenfunction for the N_v valence electrons in the spin-state (S, M), and Φ_v is the product of the N_v "valence spin-coupled orbitals", namely:

$$\Phi_v\left(\mathbf{r}_1, \mathbf{r}_2, \ldots \mathbf{r}_{N_v}\right) = \phi_1(\mathbf{r}_1)\, \phi_2(\mathbf{r}_2) \ldots \phi_{N_v}(\mathbf{r}_{N_v}) \qquad (6)$$

In the spin-coupled method, all the active SC orbitals are expanded over the traditional basis-sets of Quantum Chemistry ($\{\chi_\mu\}_{\mu=1}^{M}$, with M as the dimension of the basis):

$$\phi_i(r) = \sum_{\mu=1}^{M} C_{\mu i}\, \chi_\mu(\mathbf{r}) \qquad (7)$$

The coefficients $\{C_{\mu i}\}$ of the spin-coupled orbitals expansions are thus obtained together with the spin-coupling coefficients $\{c_{S,k}\}$ (see equations (2) and (5)) by variationally minimizing the following energy functional:

$$W\left[\{C_{\mu i}\}, \{c_{Sk}\}\right] = \frac{\langle \psi_{SC}^{S,M} | \hat{H} | \psi_{SC}^{S,M} \rangle}{\langle \psi_{SC}^{S,M} | \psi_{SC}^{S,M} \rangle} \qquad (8)$$

with $\hat{H}$ as the traditional non-relativistic Hamiltonian operator for a system of N electrons.

3.3 MATERIALS AND METHODS

To analyze the σ-hole established on the bromine atom (the reason why bromine has been chosen among all the halogens has been outlined in the introduction part of this chapter), spin coupled calculations have been performed on three brominated molecules RBr, depicted in Figure 1.

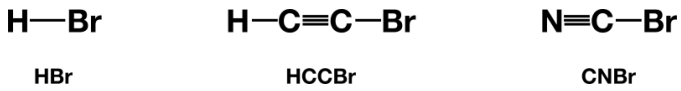

Figure 1. three brominated dimers studied performing SC calculations.

The -R groups have been chosen to tune the σ-hole intensity and monitor the variation of the SC orbitals associated to σ-hole.

To obtain the monomer geometries, Restricted Hartree-Fock calculations (RHF) have been performed, exploiting the 6-31G(d,p)[110] basis set and using Gaussian09[53]. Only the eight electrons associated with the R-Br bond and bromine lone pairs has been treated at spin-coupled level, while the others have been kept frozen as illustrated in the theory section. For sake of comparison, the SC computation has been performed also on the isolated bromine atom.

Then in order to probe the establishment and strength of the halogen bond in RBr···NH_3 dimers, we have considered the same –R substituents bonded to the bromine atom as those depicted in Figure 1: –H, HCC– (acetylene group) and –CN (cyano group), clearly characterized by an increasing electron withdrawing power and, consequently, responsible for stronger halogen bonds. Halogen bond interaction in the RBr···NH_3 dimers has been monitored performing spin-coupled calculations at different geometries previously obtained through relaxed geometry scans at Restricted Hartree-Fock (RHF) / 6-31G(d,p)[110] level in which we varied the Br ···N distance (from 2.39 Å to 7.79 Å for (CN)Br···NH_3, from 2.51 Å to 5.01 Å for HCCBr···NH_3 and from 2.58 Å to 5.68 Å for HBr···NH_3. These values have been obtained from the starting interaction distance,

adding or subtracting 0.5 Å per step) and in which we constrained the R-Br···N angle to 180°. Finally, for each dimer (-R = -H, HCC- and -CN), the asymptotic structures, basically composed by the two isolated monomers RBr and NH_3 at very large distance, have also been analyzed in order to compare the orbitals of the non-interacting monomers with those of the systems in which halogen bond occurs.

The equilibrium geometries for the RBr···NH_3 dimers have been afterwards exploited to perform single point spin-coupled calculations with only 10 active electrons (corresponding to valence electrons in equations (5) and (6)). The remaining electrons (core electrons in equations (5) and (6)) were described through doubly occupied Molecular Orbitals resulting from previous RHF calculations (see equation (5)), as already done for the monomers.

For this reason, in all our SC computations, only ten spin-coupled orbitals were directly optimized. They were those describing the three-bromine lone-pairs, the nitrogen lone-pair and the R-Br bond electron-pair (the same as those of the monomeric brominated molecules with the adding of the ammonia lone pair). For the sake of completeness, it is also worthwhile to mention that the guess for the 10 spin-coupled orbitals were localized MOs, which were previously obtained by applying the traditional localization technique[89] proposed by Pipek-Mezey to the RHF Molecular Orbitals of the systems to be examined. This procedure results to be mandatory to detect unequivocally the orbitals associated with the 10 electrons which have been chosen for the valence-bond investigation.

The 10 (8 for the monomers study) singly occupied spin-coupled orbitals (see Figure 2 for a graphical representation of the squared SC orbitals used throughout the chapter) resulting from our computations were afterwards classified (either for monomers or dimers), by observing their components expressed in atomic orbitals basis, and labeled in this way (assuming the R-Br bond

axis as the z-axis):

- ϕ_1: sp_z hybrid orbital mainly localized on the bromine atom and deformed toward the substituent R.
- ϕ_2: sp_z hybrid orbital mainly localized on the carbon atom ((CN)Br and HCCBr) or the hydrogen atom (HBr) and deformed toward the bromine atom.
- ϕ_3, ϕ_4: orbitals describing the sp_z hybrid lone-pair localized on the bromine atom. ϕ_3 is more contracted along the z-axis, while ϕ_4 is more spread towards the two directions perpendicular to the z-axis.
- ϕ_5, ϕ_6: orbitals describing the p_x lone-pair localized on the bromine atom. ϕ_5 is slightly more contracted towards the bromine atom than ϕ_6.
- ϕ_7, ϕ_8: orbitals describing the p_y lone-pair localized on the bromine atom. They are symmetry related to orbitals ϕ_5 and ϕ_6.
- ϕ_9, ϕ_{10}: orbitals describing the p_z lone-pair localized on the nitrogen atom. ϕ_{10} is more spread towards the direction of the bromine atom than orbital ϕ_9. Obviously, these two SC orbitals have been considered only for the halogen bond interacting dimers.

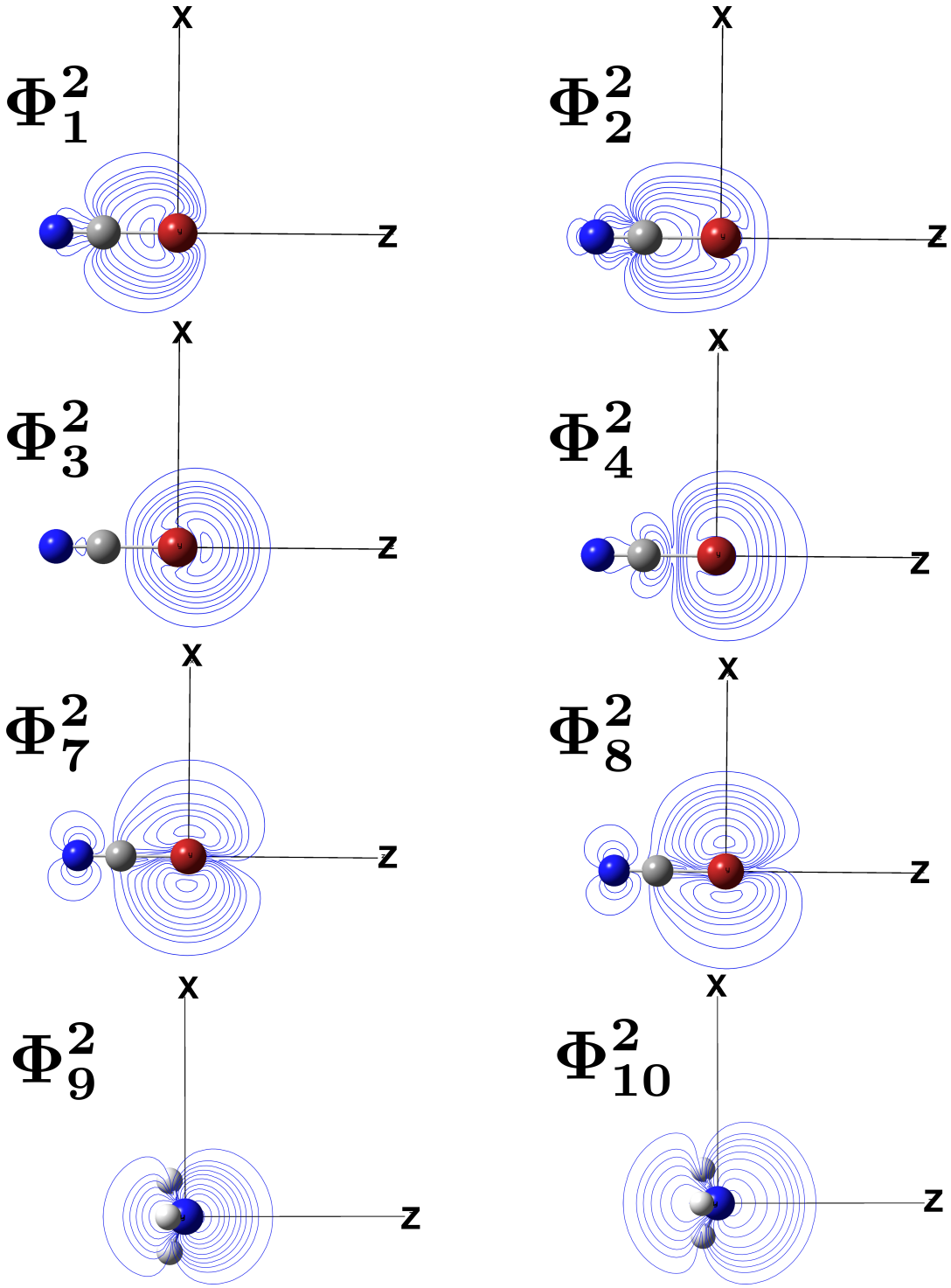

Figure 2. Symmetry independent squared spin-coupled orbitals plotted in the XZ plane (where Z is the interaction axis in the R-Br···NH3 interaction scheme). These orbitals refer to (CN)-Br···NH3 interacting dimer, however their shapes are analogous for the other two dimers and monomers discussed in this chapter. The contours values increase

in steps of 2 × 10n, 4 × 10n and 8 × 10n, with n ranging from -3 to 0 and increasing by 1 at every step. The contours levels of 5 × 10-4 au and 1 × 10-4 au have been added for the sake of completeness, both for the negative and positive contours.

Afterwards, the orbitals were analyzed by monitoring some of their overlaps and some of their squared moduli differences, both in function of the Br···N distance and in function of the substituent group R. As it will be explained in the Results Section, this allowed us, for the dimers, to detect partial delocalizations clearly associated with the presence of a halogen-bond interaction, while the analysis carried out on the monomers allows to infer some important conclusion about the intensity of the σ-hole from a valence bond perspective.

Moreover, it is worth noting that, according to equation (1), the 8 (10) active electrons (and consequently the 8 (10) associated SC orbitals mentioned above) in a singlet state can be spin-coupled in 5 (42) different ways, which correspond to 5 (42) different spin-coupled structures contributing to the global SC wave function (see Equation (5)) for the brominated monomers (dimers) case. In order to have a direct connection with the traditional Lewis chemical structures[42,111] the Rumer Spin Eigen-function basis has been exploited. The Chirgwin-Coulson weights, defined by equation (4), of all the structures have been also carefully monitored in function of the Br···N distance and in function of the substituent group R to study the formation and the strength of the halogen-bond in the investigated systems. For the brominated monomers depicted in Figure 1, only one structure among the possible 5 given by equation (1), corresponding to the so-called perfect pairing, has a weight significantly different from zero.

To obtain the dimers geometries the Gaussian09[53] software has been used, while for the SC calculations the code developed in our research group has been used.[108]

3.4 RESULTS AND DISCUSSION

The first important result of the present spin-coupled analysis of the σ-hole deals with the demonstration that our computational VB approach fully confirms the previous models, such as the Politzer one[22], based on the concept of σ-hole and anisotropy of electrostatic potential around halogens or the lump-hole model[24], based on the QTAIM[45] interpretation of the Laplacian of electron density as regions of concentration or depletion of electron density depending on its sign. Or even, the interpretation of σ-hole by exploiting the Fukui function[112] that is shown, for the three monomers studied herein, in Figure 3.

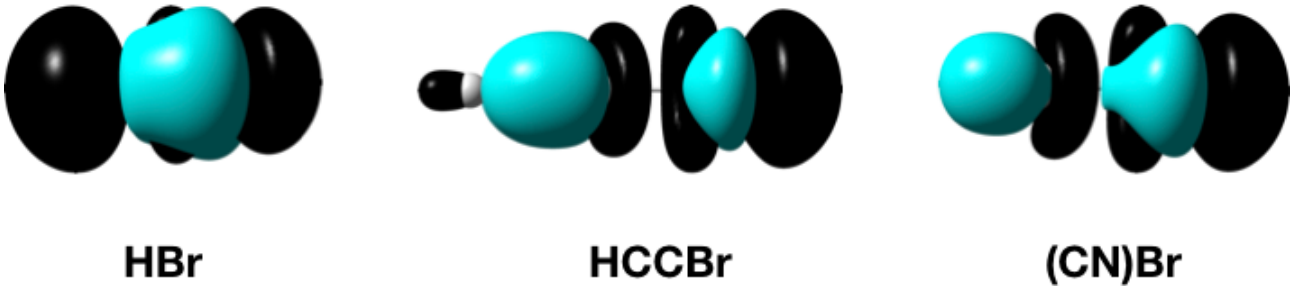

Figure 3. Fukui (f^+ in black and f^- in light blue) function, based on frontier molecular orbitals (FMO) isosurfaces (0.0004 a.u.) evaluated at RHF/6-31G(d,p) level.

Anyway, the task of reproducing these models through SC calculations has been totally accomplished, as it can be verified observing the Figure 4, 5 and 6, where the electrostatic potential and the Laplacian of electron density, derived from the SC wavefunction, following the equation (9), have been shown.

$$\rho(\boldsymbol{r}) = \rho_{core}(\boldsymbol{r}) + \rho_{SC}(\boldsymbol{r}) = 2\sum_{t=1}^{N_{core}} |\phi_t(\boldsymbol{r})|^2 + \frac{1}{\Delta}\sum_{t,u=1}^{N} \phi_t(\boldsymbol{r})\,\phi_u(\boldsymbol{r})\,D(t|u) \qquad (9)$$

From these Figures, it is possible to observe that for all the monomers the SC approach is able not only to correctly recover the concept of σ-hole as derived from MO theories, such as MP2 or RHF, but also to precisely predict the σ-hole intensity trend in function of the electron-withdrawing power of the -R substituent.

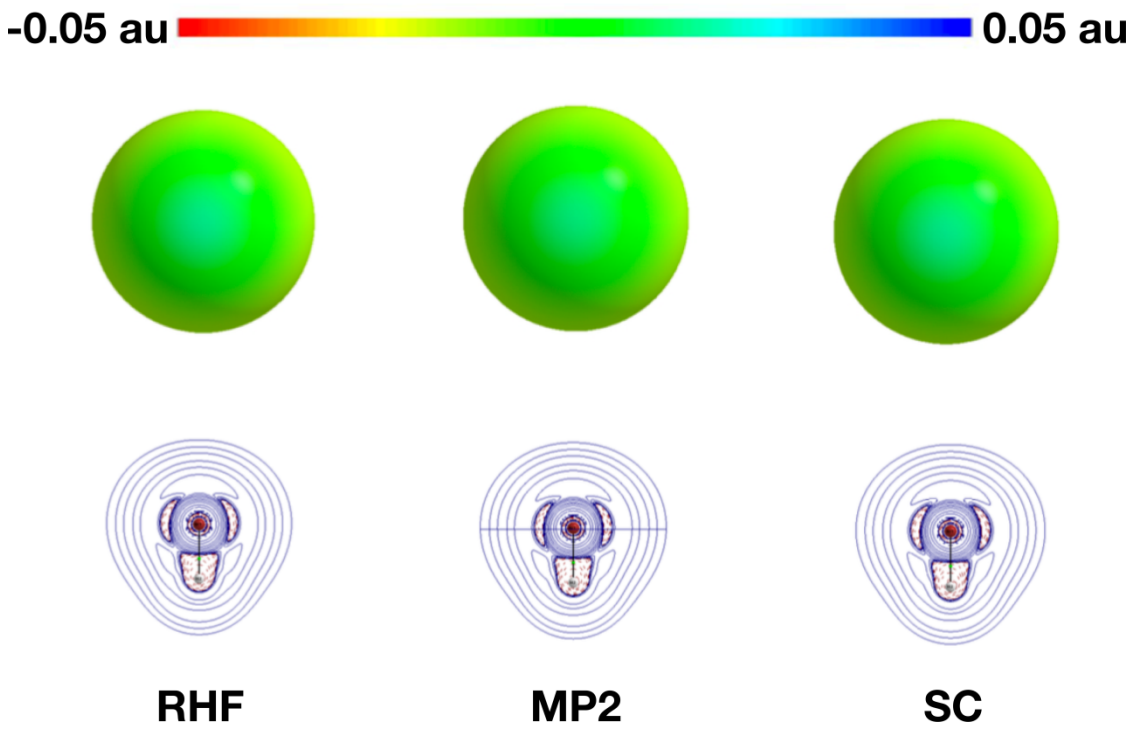

Figure 4. Top: HBr ESP surface, plotted onto the ρ(r)=0.0004 au iso-surface. Down: HBr $\nabla^2\rho(r)$. The contours values increase in steps of 2 × 10n, 4 × 10n and 8 × 10n, with n ranging from -3 to 0 and increasing by 1 at every step. Blue (red) contours represent positive (negative) $\nabla^2\rho(r)$. RHF, MP2 and SC surfaces and contours have been reported for sake of comparison.

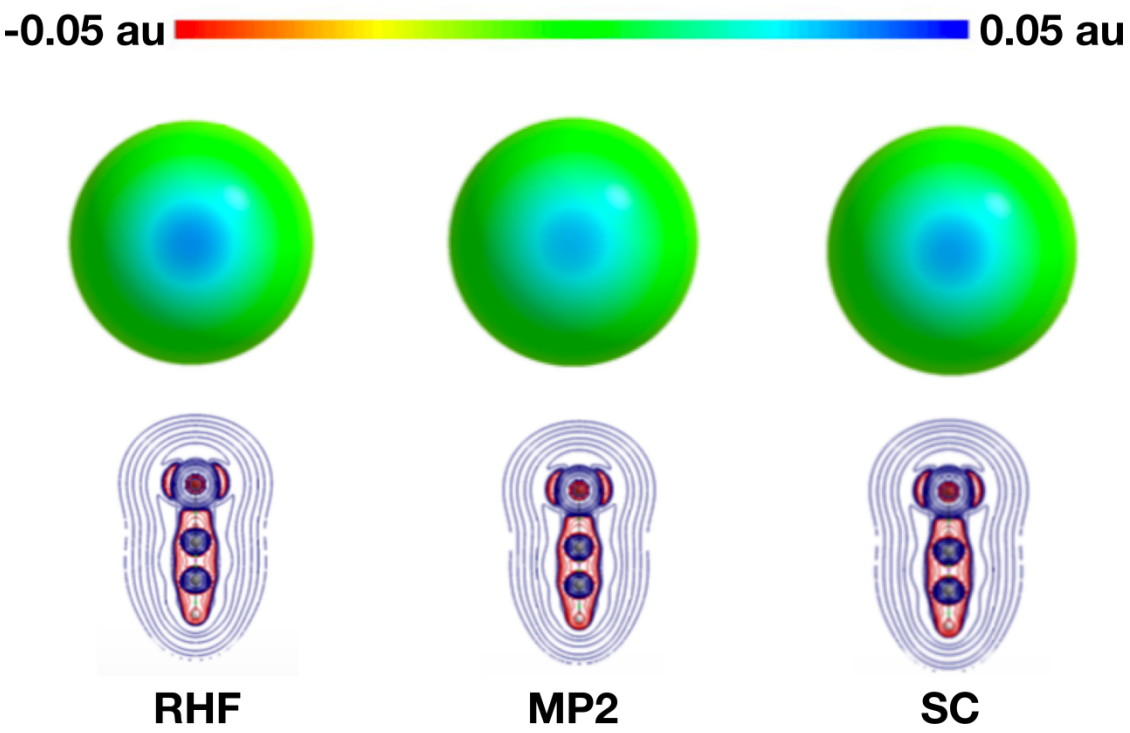

Figure 5. Top: HCCBr ESP surface, plotted onto the ρ(r)=0.0004 au iso-surface. Down: HCCBr $\nabla^2\rho(r)$. The contours values increase in steps of 2 × 10n, 4 × 10n and 8 × 10n, with n ranging from -3 to 0 and increasing by 1 at every step. Blue (red) contours represent positive (negative) $\nabla^2\rho(r)$. RHF, MP2 and SC surfaces and contours have been reported for sake of comparison.

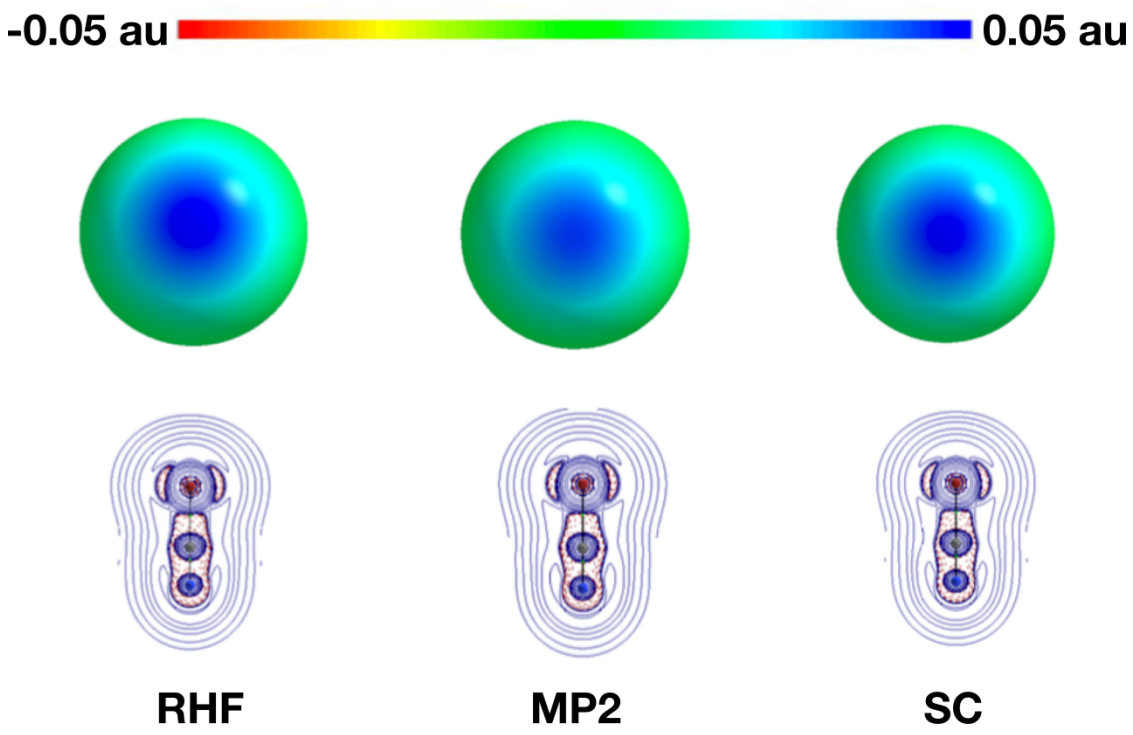

Figure 6. Top: (CN)Br ESP surface, plotted onto the ρ(r)=0.0004 au iso-surface. Down: (CN)Br $\nabla^2\rho(r)$. The contours values increase in steps of 2 × 10n, 4 × 10n and 8 × 10n, with n ranging from -3 to 0 and increasing by 1 at every step. Blue (red) contours represent positive (negative) $\nabla^2\rho(r)$. RHF, MP2 and SC surfaces and contours have been reported for sake of comparison.

Once verified (through the electron densities comparison) that the spin-coupled approach can describe correctly halogen bond (see the previous pictures), this approach has been exploited to study the process of establishment of the σ-hole. Then, as a result of the spin coupled calculations carried on the isolated bromine atom and on the RBr monomers, some useful information on this process have been devised, as can be seen from Figure 7.

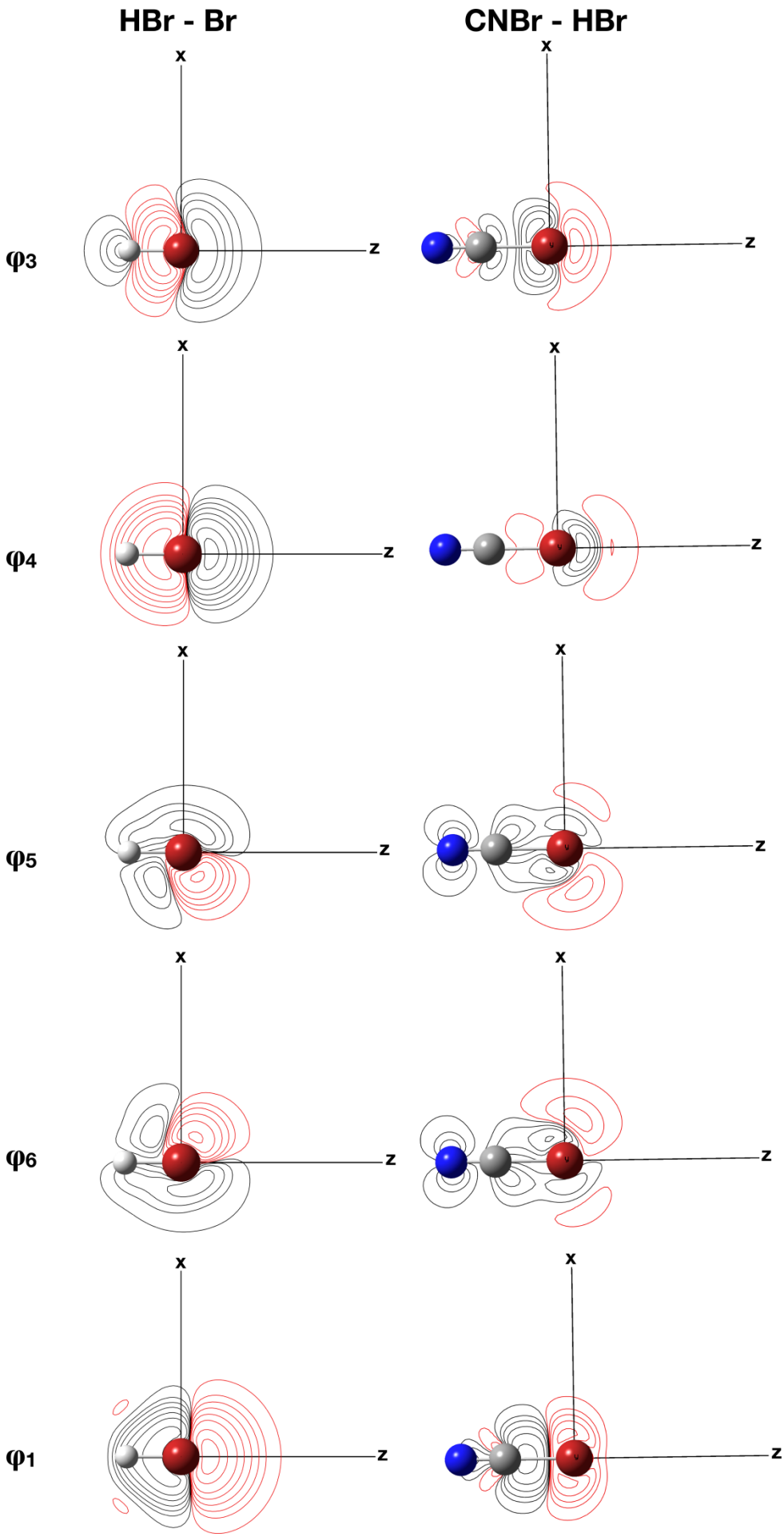
HBr - Br
CNBr - HBr
φ3
φ4
φ5
φ6
φ1
x
z

Figure 7. (HBr – Br) and ((CN)Br – HBr) Spin-coupled squared orbitals differences. The contours values increase in steps of 2 × 10n, 4 × 10n and 8 × 10n, with n ranging from -3 to 0 and increasing by 1 at every step. The contours levels of 5 × 10-4 au and 1 × 10-4 au have been added for the sake of completeness, both for the negative and positive contours. Red and black contours correspond to negative and positive values respectively.

Firstly (by observing Figure 7), ϕ_1 is far more contracted in the region outside the halogen, following the formation of R-Br bond, as can be seen from the analysis of the difference between ϕ_1^2 relative to HBr and the corresponding SC orbital of the isolated bromine. This observation is in perfect agreement with what Politzer states about the depletion of p_z electron density as a result of the R-Br bond instauration. Furthermore, this depletion of ϕ_1 orbital is also observed to increase passing from R=H to the more electron-withdrawing species such as R=CN. Consequently, also the trend of the σ-hole intensity upon the R group variation is fully devised by spin-coupled calculations.

The contraction mentioned above is observed also for ϕ_3 and ϕ_4 passing from R=H to R=CN. Surprisingly, this is not the case for the difference of ϕ_3^2 and ϕ_4^2 relative to HBr with the same orbital referred to Br. However, this observation could be interpreted as a sign of the weakness of HBr σ-hole due to the low electronegativity of the hydrogen atom. Moreover, ϕ_3 and ϕ_4 could be interpreted as the s^2 orbitals of the Politzer model (although their nature, according to SC calculation, is closer to hybrid sp_z orbitals as stated in the previous section) that are not the direct responsible of the σ-hole establishment, differently from ϕ_1 that can be associated, as mentioned before, with the p_z orbital of that model.

Finally, the observed behavior of the differences between the square of SC orbitals relative to the two lone pairs located on the perpendicular directions to the z-axis (ϕ_5 and ϕ_6 and the symmetry related ϕ_7 and ϕ_8) could be easily associated with the formation of the negative ESP belt observed

around the halogens by the previous mentioned model.

To conclude, SC calculations carried out on isolated brominated monomers fully confirm in a more formal way (as stated from Figure 7) the model proposed by Politzer.

Once verified that the SC approach is able to correctly describe the σ-hole established in halogenated molecules, it has been decided to perform spin-coupled computations on brominated dimers with ammonia. Indeed, as described in the previous section, several SC calculations have been carried out on different points of the halogen bond "interaction coordinate", with the aim of capturing the main features occurring as a result of the XB formation.

As pointed out before, several valence-bond, and particularly spin-coupled, descriptors were adopted to analyze the formation and the strength of the halogen bond occurring in the studied $RBr\cdots NH_3$ dimers: overlap between the SC orbitals, their shape and the Chirgwin-Coulson weights of the 5 spin-coupled structures associated to the non-covalent interaction.

Firstly, the focus of the survey was on the study of the overlap integrals between the 10 orbitals, already depicted in the previous section, optimized through SC calculations. In particular, since ϕ_9 and ϕ_{10} orbitals are the ones prevalently localized on the nitrogen atom (describing the ammonia lone-pair), it has been decided to observe their overlaps with the other eight SC orbitals (mainly localized on Br and R-Br bond) in function of the distance between bromine and nitrogen, with the aim of, eventually, interpreting their expansions towards the bromine atom (or contraction on the nitrogen) as a clue of the establishment of the halogen bond. All calculations point out to the fact that, for all the "interaction coordinate" points representing the different Br···N distances, the greatest overlaps of ϕ_9 and ϕ_{10} (the orbitals describing the nitrogen lone-pair) were with z-symmetry bromine orbitals (ϕ_1, ϕ_2, ϕ_3 and ϕ_4), while those between the same nitrogen SC

orbitals and the other orbitals on bromine (associated with the perpendicular bromine lone pairs) were almost negligible. In particular, the largest overlaps of the nitrogen associated orbitals (ϕ_9 and ϕ_{10}) are with ϕ_1, which, from a spin-coupled point of view, could be addressed as the main responsible for the halogen bond interaction (indeed, it is the one that in the Politzer model gives rise to the σ-hole, allowing halogen bond establishment). In Figure 8, it has also graphically depicted the trend of the overlaps of ϕ_9 (Figure 8A) and ϕ_{10} (Figure 8B) with ϕ_1, ϕ_2, ϕ_3 and ϕ_4 in function of the Br···N distance for the (CN)Br···NH_3 dimer. It is easily possible to observe that, both for ϕ_9 and ϕ_{10}, the overlaps increase as the two monomers approach each other, thus testifying the presence of XB interaction at shorter distances. Analogous trends turn out for the HCCBr···NH_3 and HBr···NH_3 dimers (see Figures 9 and 10), although the magnitudes of the orbitals considered (when substituents HCC– and –H are considered) sensibly drop with respect to those observed in (– CN), which is in good agreement with the halogen bond strength variation upon substituent variation. This observation could be also devised from Table 1, reporting the overlaps at the equilibrium distances for the three studied dimers. These results further confirm that the strength of XB decreases as the electron-withdrawing character of the R substituent reduces.

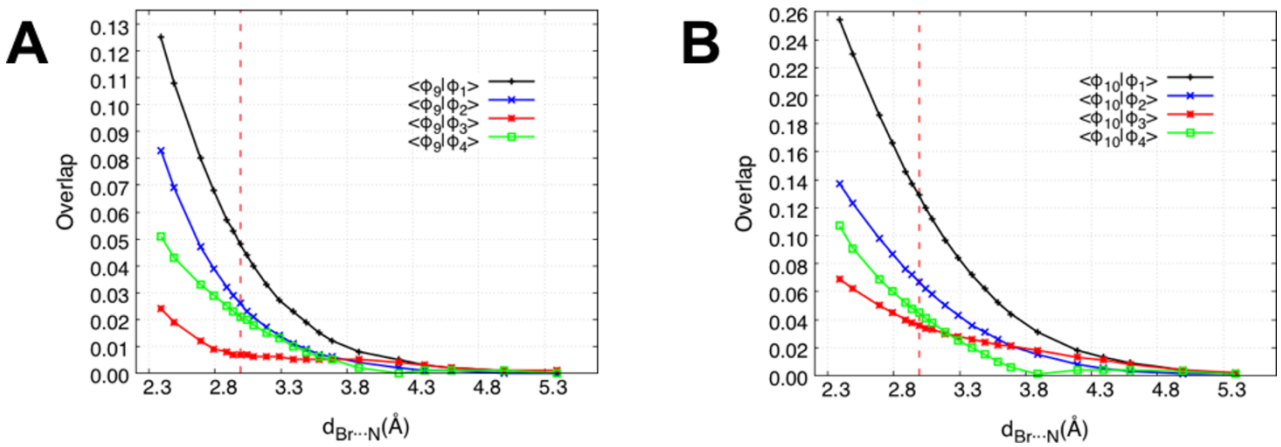

Figure 8. Overlaps of the spin-coupled orbitals ϕ_9 and ϕ_{10} with the spin-coupled orbitals ϕ_1, ϕ_2, ϕ_3 and ϕ_4 in function of the Br···N distance for the (CN)Br···NH_3 dimer. The vertical red dotted lines indicate the Br···N equilibrium distance.

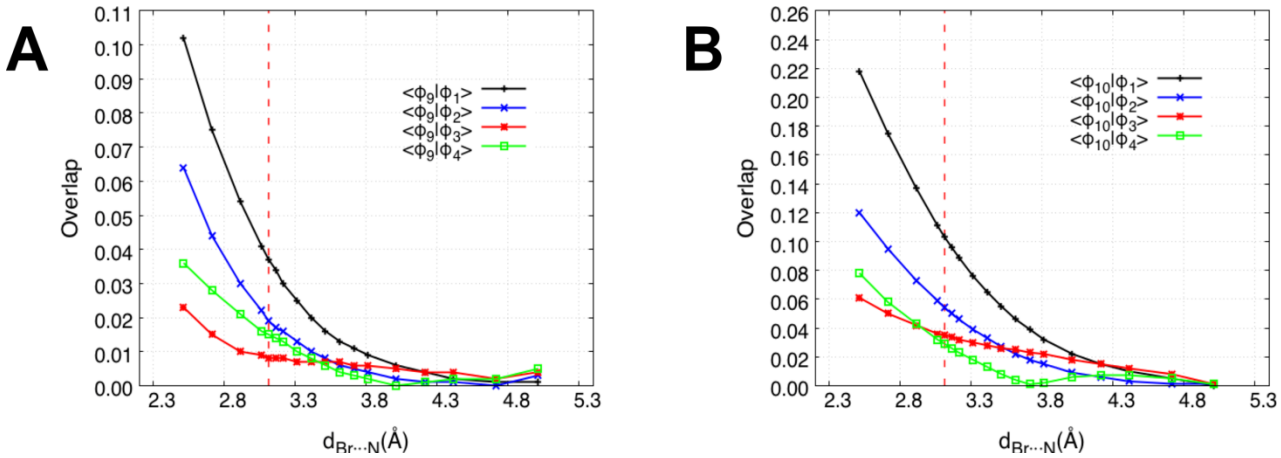

Figure 9. Overlaps of the spin-coupled orbitals ϕ_9 and ϕ_{10} with the spin-coupled orbitals ϕ_1, ϕ_2, ϕ_3 and ϕ_4 in function of the Br···N distance for the HCCBr···NH_3 dimer. The vertical red dotted lines indicate the Br···N equilibrium distance.

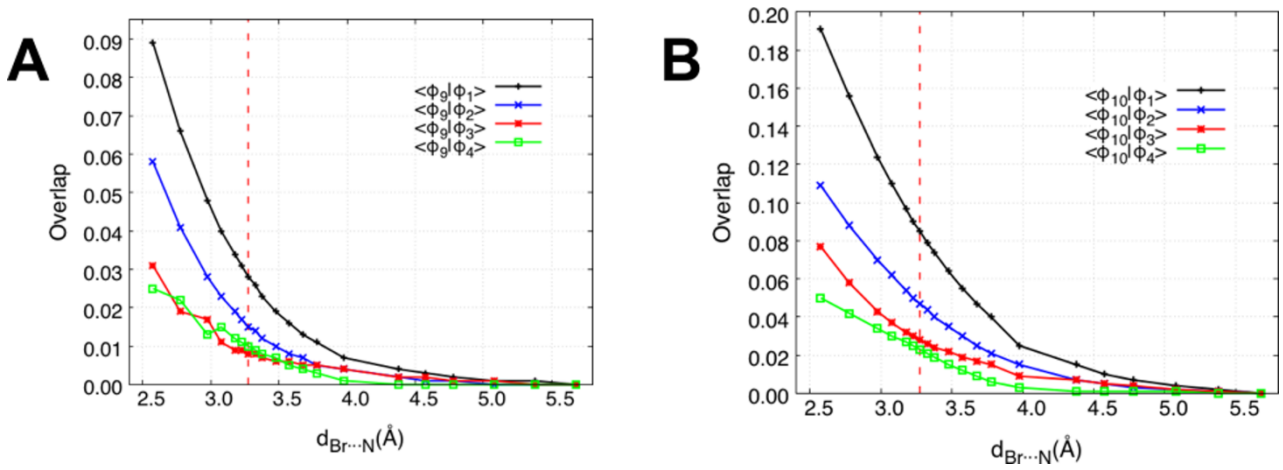

Figure 10. Overlaps of the spin-coupled orbitals ϕ_9 and ϕ_{10} with the spin-coupled orbitals ϕ_1, ϕ_2, ϕ_3 and ϕ_4 in function of the Br···N distance for the $HBr\cdots NH_3$ dimer. The vertical red dotted lines indicate the Br···N equilibrium distance.

Table 1. Absolute values of the overlaps of the spin-coupled orbitals ϕ_9 and ϕ_{10} with the spin-coupled orbitals ϕ_1, ϕ_2, ϕ_3 and ϕ_4 at the equilibrium distances for the dimers $(CN)Br\cdots NH_3$, $HCCBr\cdots NH_3$ and $HBr\cdots NH_3$

	$(CN)Br\cdots NH_3$		$HCCBr\cdots NH_3$		$HBr\cdots NH_3$	
	ϕ_9	ϕ_{10}	ϕ_9	ϕ_{10}	ϕ_9	ϕ_{10}
ϕ_1	0.048	0.129	0.037	0.103	0.028	0.085
ϕ_2	0.026	0.067	0.019	0.054	0.015	0.047
ϕ_3	0.021	0.045	0.008	0.035	0.010	0.023
ϕ_4	0.007	0.036	0.015	0.029	0.008	0.028

Another brand new (in the framework of halogen bond studies) descriptor adopted to reveal the presence of a halogen bond in the examined systems were the shapes of the obtained spin coupled orbitals. Firstly, the ϕ_9 and ϕ_{10} orbitals have been considered, which are the ones associated with the nitrogen atom. For each of them, the differences between their squared moduli at the equilibrium (eq) and asymptotic (∞) distances (i.e., $\left|\phi_9^{eq}\right|^2 - |\phi_9^{\infty}|^2$ and $\left|\phi_{10}^{eq}\right|^2 - |\phi_{10}^{\infty}|^2$) have been computed and then plotted. The differences relative to the (CN)Br···NH3 dimer are illustrated in Figures 11A and 11B. It can be observed that both orbitals ϕ_9 and ϕ_{10} are more localized on the nitrogen atom at the asymptotic distance, while they clearly undergo a shift towards the bromine atom as the two monomers approach the equilibrium distance. Moreover, this effect is far more pronounced for ϕ_{10} than for ϕ_9 orbital. Also, these observations can be interpreted as another clue of the formation of a halogen bond interaction RX···B at the equilibrium distance and could be rationalized throughout a classical chemical mechanism in which one electron of the lone-pair localized on the acceptor atom B shifts towards electrophilic region located on the halogen, while the second electron of the pair tends to remain localized on the base (the nitrogen in this thesis). Furthermore, it is appealing and unexpected that, during the establishment of the halogen bond, ϕ_{10}, that is the SC orbital describing the electron donated by the nitrogen atom, is localized also in the region of the C-Br bond and not only outward this bond (see Figures 11B, 11D and 11F). Consequently, the following conclusion on the nature of halogen bonding is drawn from a valence-bond point of view: the σ-hole, which is usually observed along the z-axis, in the region outward the halogen atom, exists also behind the halogen in the direction of the substituent group R. The RHF/6-31G(d,p) derived electrostatic potential plot in the xz plane indeed shows (see Figure 12) that the depletion of electron density along the z-axis around the halogen atom is not only localized outward the halogen atom, but it, actually, consists of an extended positive region of electrostatic

potential along the R-Br bond. Therefore, the σ-hole could be actually seen as a "σ-tunnel" in terms of spin-coupled orbitals. This region of positive electrostatic potential attracts negative electron density from acceptor B, mainly represented by ϕ_{10} in this Chapter, and this is the reason why in all spin-coupled calculations performed at the equilibrium distances, the largest overlaps for the "shifted" (see Figure 8, 9 and 10) orbitals ϕ_9 and ϕ_{10} have been observed with orbital ϕ_1, which is the orbital localized on the R-Br region (see Figure 2).

For the sake of completeness, in Figure 11 it has also reported the differences between the squared moduli of orbitals ϕ_9 and ϕ_{10} at the equilibrium and asymptotic distances for the dimers HCCBr···NH_3 (Figures 11C and 11D) and HBr···NH_3 (Figures 11E and 11F). Although at lower extent, the trends are analogous to those observed for (CN)Br··· NH_3, further indicating that the strength of the XB interaction reduces when a less strong electron-withdrawing group is bonded to the halogen atom.

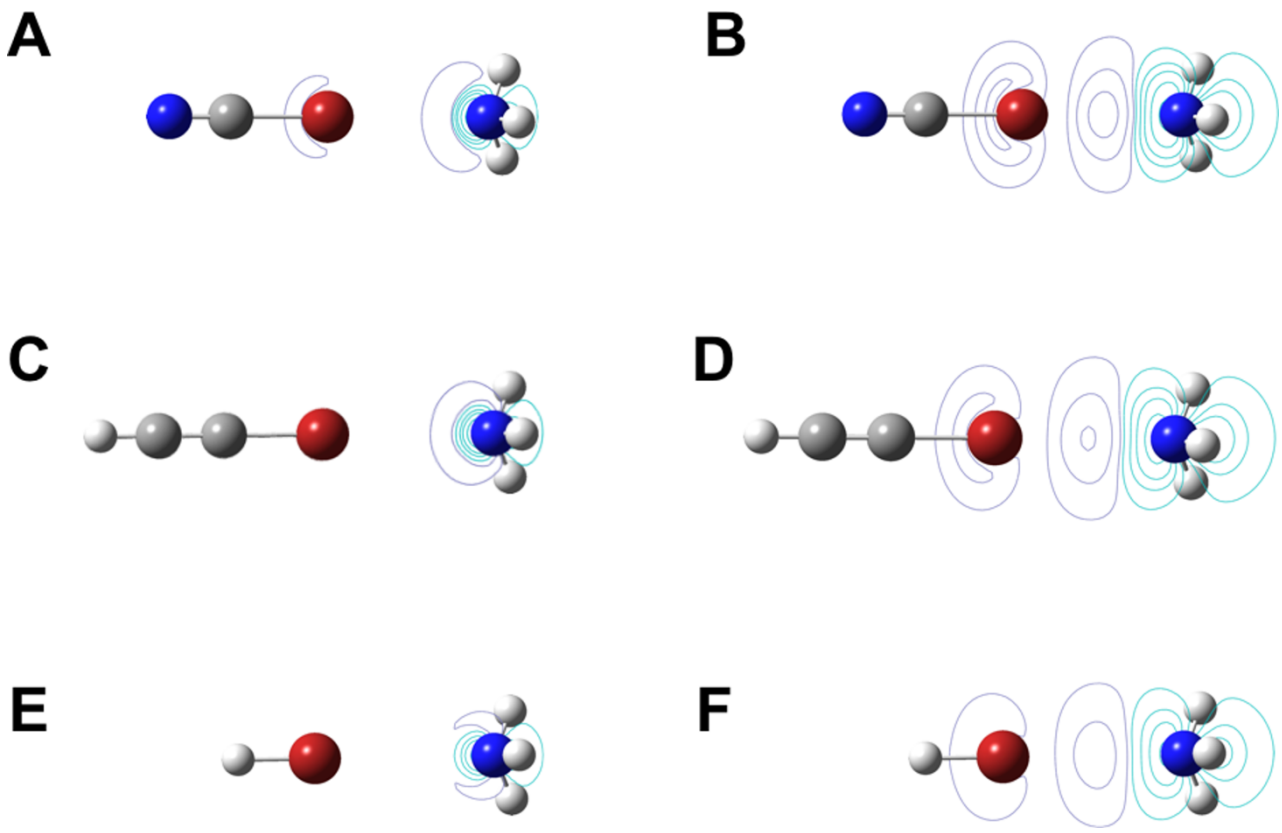

Figure 11. Differences between the squared moduli of the spin-coupled orbitals ϕ_9 (A, C and E) and ϕ_{10} (B, D and F) at the equilibrium and asymptotic distances for the dimers (CN)Br···NH_3 (A, B), HCCBr···NH_3 (C, D) and HBr···NH_3 (E, F). Positive and Negative contour levels are depicted in purple and light blue, respectively. The absolute values (in au) of the positive and negative contours increase in steps of 2 × 10n, 4 × 10n and 8 × 10n, with n ranging from -3 to 0 and increasing by 1 at every step. The contours levels of 5 × 10-4 au and 1 × 10-4 au have been added for the sake of completeness, both for the negative and positive contours.

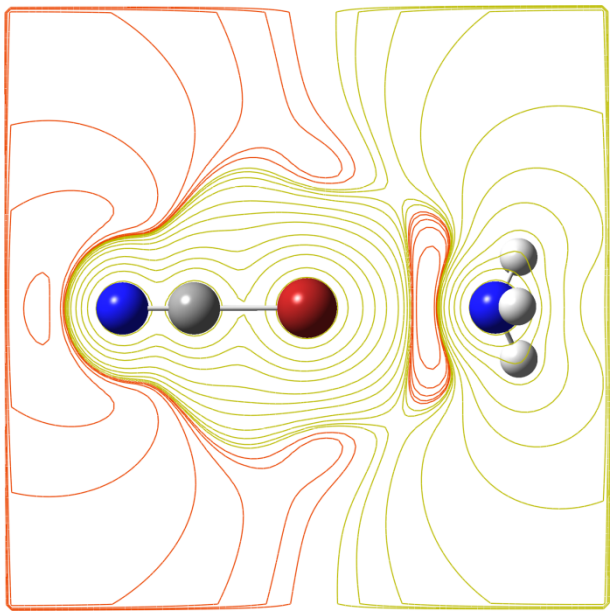

Figure 12. Contour levels of the Electrostatic Potential in the xz plane for the (CN)Br··· NH_3 dimer at the RHF level. Positive and Negative contour levels are depicted in yellow and orange colours, respectively. The absolute values (in au) of the positive and negative contours increase in steps of 2 × 10n, 4 × 10n and 8 × 10n, with n ranging from -3 to 0 and increasing by 1 at every step. The contours levels of 5 × 10-4 au and 1 × 10-4 au have been added for the sake of completeness, both for the negative and positive contours.

Finally, the z-symmetry orbitals ϕ_1, ϕ_2 and ϕ_4, localized on bromine have been analyzed. As previously, the differences between their squared moduli at the equilibrium and asymptotic geometries have been plotted. The results obtained for the three dimers (CN)Br···NH_3 (Figure 13), HCCBr···NH_3 (Figue 14) and HBr···NH_3 (Figure 15) are completely analogous and the conclusion is the same: the three examined spin-coupled orbitals shift/delocalize towards the substituent group R. This leaves a depletion of charge around the bromine atom that can be easily associated with the σ-hole of the Politzer model.

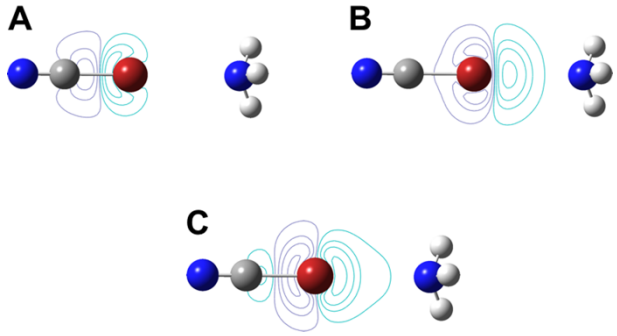

Figure 13. Differences between the squared moduli of the spin-coupled orbitals ϕ_1 (A), ϕ_3 (B) and ϕ_4 (C) at the equilibrium and asymptotic distances for the (CN)Br···NH_3 dimer. Positive and Negative contour levels are depicted in purple and light blue, respectively. The absolute values (in au) of the positive and negative contours increase in steps of 2 × 10n, 4 × 10n and 8 × 10n, with n ranging from -3 to 0 and increasing by 1 at every step. The contours levels of 5 × 10-4 au and 1 × 10-4 au have been added for the sake of completeness, both for the negative and positive contours.

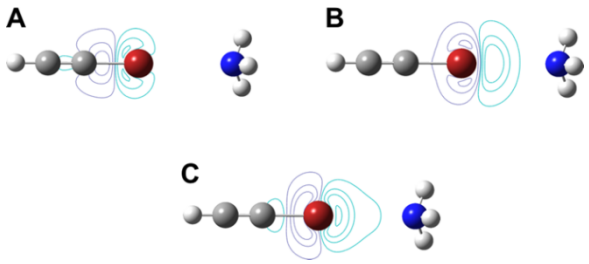

Figure 14. Differences between the squared moduli of the spin-coupled orbitals ϕ_1 (A), ϕ_3 (B) and ϕ_4 (C) at the equilibrium and asymptotic distances for the HCCBr···NH_3 dimer. Positive and Negative contour levels are depicted in purple and light blue, respectively. The absolute values (in au) of the positive and negative contours increase in steps of 2 × 10n, 4 × 10n and 8 × 10n, with n ranging from -3 to 0 and increasing by 1 at every step. The contours levels of 5 × 10-4 au and 1 × 10-4 au have been added for the sake of completeness, both for the negative and positive contours.

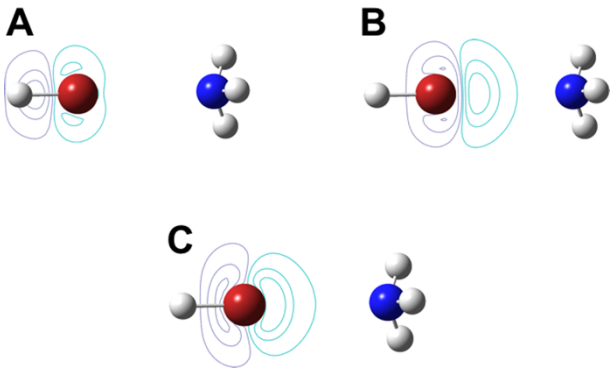

Figure 15. Differences between the squared moduli of the spin-coupled orbitals ϕ_1 (A), ϕ_3 (B) and ϕ_4 (C) at the equilibrium and asymptotic distances for the HBr···NH_3 dimer. Positive and Negative contour levels are depicted in purple and light blue, respectively. The absolute values (in au) of the positive and negative contours increase in steps of 2 × 10n, 4 × 10n and 8 × 10n, with n ranging from -3 to 0 and increasing by 1 at every step. The contours levels of 5 × 10-4 au and 1 × 10-4 au au have been added for the sake of completeness, both for the negative and positive contours.

To complete this Valence Bond survey of the bromine halogen bond interaction, the Chirgwin-Coulson weights of the different SC structures that contribute to the global spin-coupled wave functions have been calculated and studied. Particularly, only the absolute values trends of the Chirgwin-Coulson coefficients associated with the different SC structures associated with halogen bonding have been monitored upon the varying of the Br···N distance in the three different cases. It has already pointed out that the 10 active electrons of our singlet-state systems can be potentially spin-coupled in 42 different ways corresponding to 42 spin-coupled structures in wave function. The structures taken into account are the followings: i) the perfect pairing structure, namely the structure corresponding to spin-coupling $\phi_1 - \phi_2 \;\; \phi_3 - \phi_4 \;\; \phi_5 - \phi_6 \;\; \phi_7 - \phi_8 \;\; \phi_9 - \phi_{10}$ (from now on indicated as structure 1); ii) structure 2, corresponding to spin-coupling $\phi_1 - \phi_4 \;\; \phi_2 - \phi_3 \;\; \phi_5 - \phi_6 \;\; \phi_7 - \phi_8 \;\; \phi_9 - \phi_{10}$; iii) structure 3, corresponding to spin-coupling $\phi_1 - \phi_9 \;\; \phi_2 - \phi_{10} \;\; \phi_3 - \phi_4 \;\; \phi_5 - \phi_6 \;\; \phi_7 - \phi_8$; iv) structure 4, corresponding to spin-coupling

$\phi_1 - \phi_4$ $\phi_2 - \phi_{10}$ $\phi_3 - \phi_9$ $\phi_5 - \phi_6$ $\phi_7 - \phi_8$; v) structure 5, corresponding to spin-coupling $\phi_1 - \phi_2$ $\phi_3 - \phi_9$ $\phi_4 - \phi_{10}$ $\phi_5 - \phi_6$ $\phi_7 - \phi_8$).

The first two structures correspond to the ones associated with the isolated monomers, while structures 3, 4 and 5 are actually the ones that, from a traditional chemical point of view, can be easily associated with the formation of the halogen bonding interaction. Indeed, each of them involves the pairing of a SC orbital localized on the nitrogen atom with one or more z-symmetry SC orbitals localized on the bromine atom.

Although quite small, for all the investigated dimers, the Chirgwin-Coulson coefficients of structures 3-5 consistently increase as the two monomers approach and become significantly different from zero around the equilibrium distance (see Figure 16 dimer and Figures 17 and 18 for the (CN)Br···NH_3, HCCBr···NH3 and HBr···NH_3 dimers, respectively). This could be a further indication of the existence of a halogen bond for the different systems at their equilibrium geometries. Furthermore, also in this case, there are clear evidences that the strength of the XB interaction increases with the electron-withdrawing power of the substituent group R. In fact, if we consider the weights of structures 3-5 at the Br···N equilibrium distances (see Table 2), it can be easily noted that the largest and smallest values are observed for R=–CN and R=–H, respectively, in agreement with the predicted trend according to the σ-hole model proposed by Politzer.

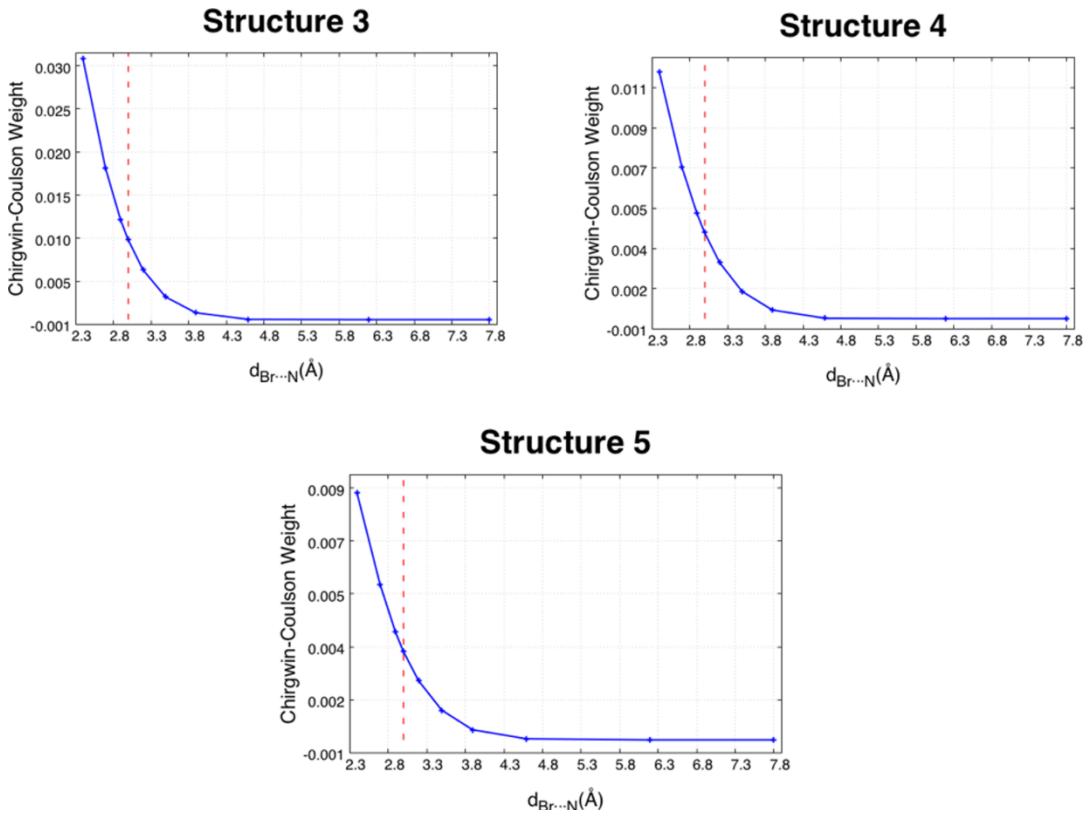

Figure 16. Absolute values of the Chirgwin-Coulson coefficients associated with structures 3, 4 and 5 of the $(CN)Br\cdots NH_3$ dimer in function of the Br···N distance. The vertical red dotted lines indicate the Br···N equilibrium distance.

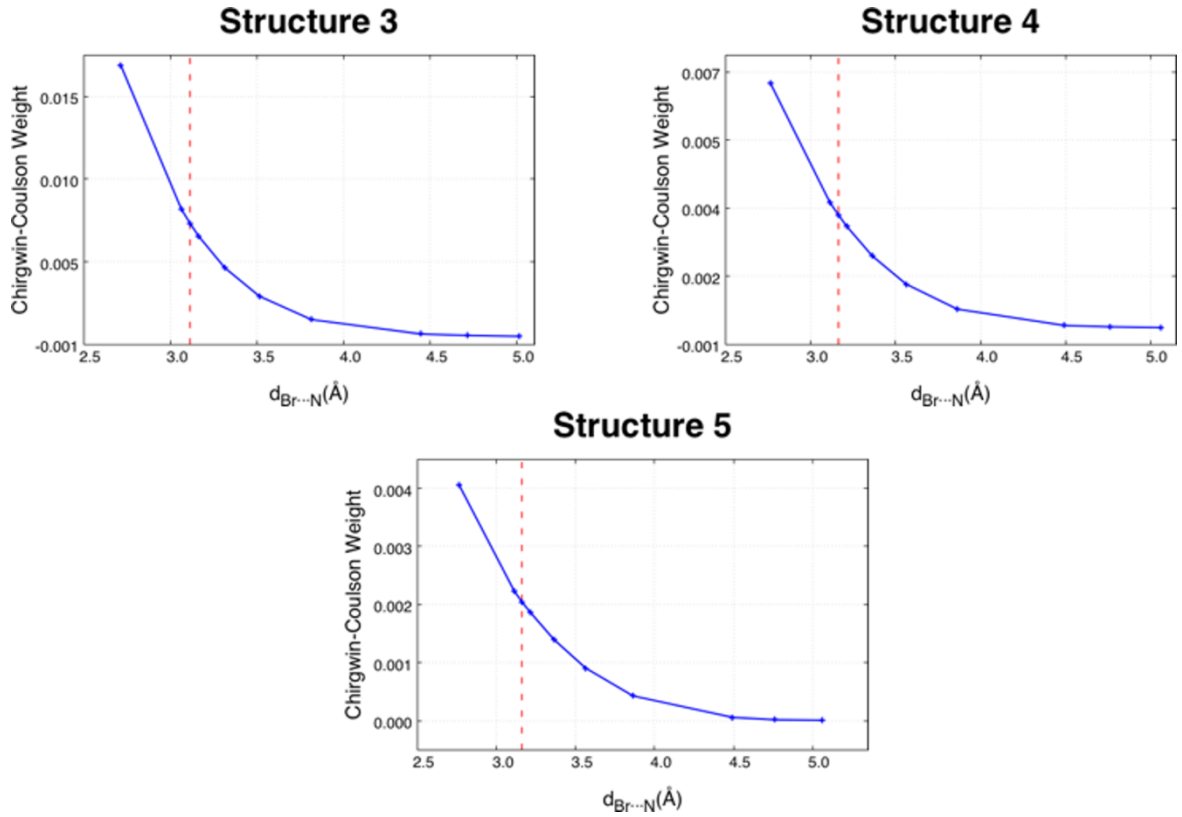

Figure 17. Absolute values of the Chirgwin-Coulson coefficients associated with structures 3, 4 and 5 of the HCCBr···NH_3 dimer in function of the Br···N distance. The vertical red dotted lines indicate the Br···N equilibrium distance.

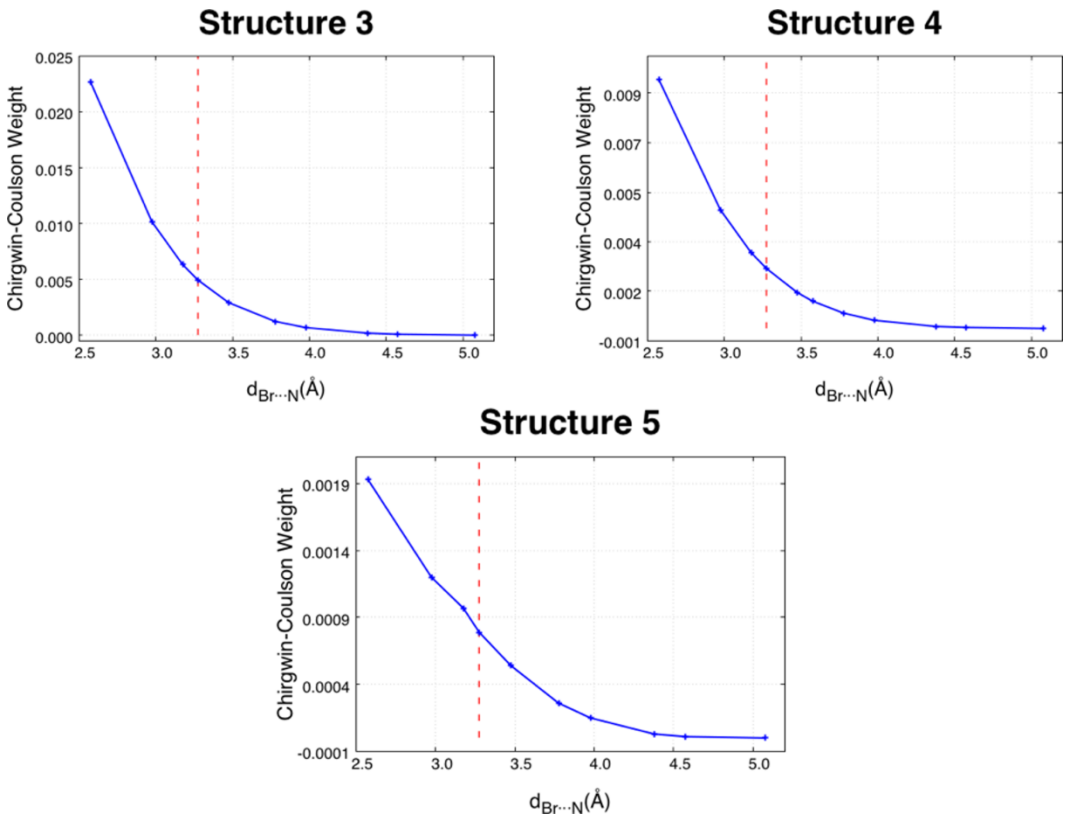

Figure 18. Absolute values of the Chirgwin-Coulson coefficients associated with structures 3, 4 and 5 of the HBr···NH_3 dimer in function of the Br···N distance. The vertical red dotted lines indicate the Br···N equilibrium distance.

Table 2. Absolute values of the Chirgwin-Coulson weights for spin-coupled structures 3, 4 and 5 of dimers (CN)Br···NH_3, HCCBr··· NH3 and HBr··· NH_3 at their Br···N equilibrium distances.

	(CN)Br···NH_3	HCCBr···NH_3	HBr··· NH_3
Structure 3	9.35×10-3	6.82×10-3	4.93×10-3
Structure 4	4.30×10-3	3.31×10-3	2.42×10-3
Structure 5	3.34×10-3	2.04×10-3	7.9×10-4

3.5 CONCLUSIONS

At first, the models developed in the past to describe the σ-hole, such as the Politzer model and the lump-hole one, have been fully confirmed by our spin-coupled calculations on brominated molecules, then proving SC to constitute a valuable tool to provide an insight in halogen bond nature.

Consequently, the attention has been focused on the study of halogen bonded systems, such as (CN)Br···NH3, HCCBr···NH3 and HBr···NH3. Herein, halogen bonding interaction was established between the ammonia lone pair and bromine, the different substituents have been chosen to cover different degrees of electron-withdrawing power, with the aim of tuning the intensity of the bromine σ-hole to study different kinds of XB interaction.

Moreover, in order to study the process of halogen bonding formation, SC calculation have been carried out on several points of the "interaction coordinate" provided by RHF relaxed energy scan computations along the interaction axis. Then, the analysis of different descriptors associated with the spin-coupled technique, such as the overlap between the spin-coupled orbitals, their shapes and the Chirgwin-Coulson weights of the spin-coupled structures, has allowed to draw some important conclusion:

- The SC descriptors, mentioned above, are able to account for the different strength in XB interaction upon variation of the substituent R, confirming them to be useful to feature such non-covalent interactions.
- Moreover, analyzing our results it could also be observed that the spin-coupled orbital describing one of the electrons of the donor's lone pair, as a result of the halogen bond formation, is localized on the halogen atom in the direction pointing towards the substituent group R of the halogen so that the σ-hole becomes a σ-tunnel for the spin-coupled orbitals. This observation represents a remarkable step forward in the theoretical description of halogen bond.

As a consequence of our results, it would be interesting to use the spin-coupled theory to describe other kinds of halogen bonding systems, varying the halogen or the acceptor molecules in order to generalize our model.

4. X-RAY CONSTRAINED SPIN-COUPLED

The direct definition of Quantum Crystallography (QCr) includes all those methods in which the information intrinsically contained in experimental crystallographic data is used as an external constraint to enhance the information usually provided by the traditional Quantum Chemistry calculations. In this introductive chapter, after a review on the pioneering techniques within the first aspects of the original definition of QCr, it will be introduced in detail the X-ray constrained wave function approach originally proposed by Jayatilaka.[113–118] In this chapter, after a brief introduction of the X-Ray Constrained Wavefunction (XCW) philosophy, it will be illustrated the method developed in collaboration with Dr. Alessandro Genoni, named X-Ray Constrained Spin-Coupled (XCSC),[31] that allows to obtaine an experimental constrained spin-coupled[106] wavefunction, which is the first attempt of recovering these kind of information in the framework of valence bond methods. Then, first preliminary results of the proposed method will be shown, with the aim of shedding light on the potentialities of this new tool.

4.1 X-RAY WAVEFUNCTION METHODS

All the current versions of the XCW approach can be applied only to molecular crystals. In this context, it has to be considered a fictitious crystalline system in which each crystal molecular unit does not interact with the other ones, but for which, at the same time, the global electron density is identical to the one of the corresponding real interacting crystalline system (see Figure 1).

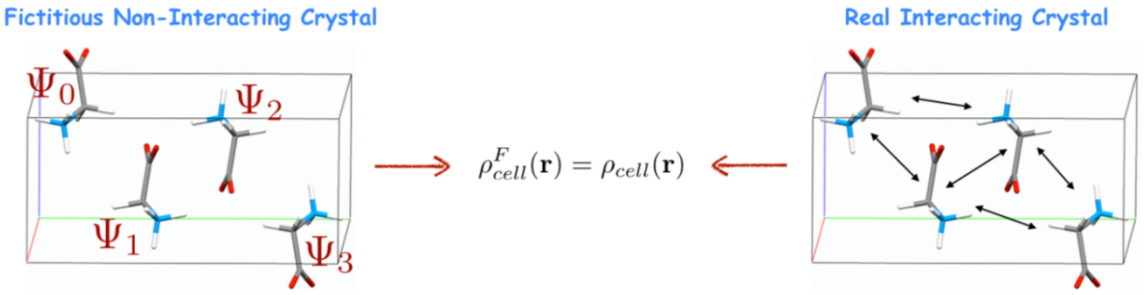

Figure 1. Schematic representation of the basic assumptions of the XCW approach.

The first assumption allows us to write the global wave function of the crystal as:

$$|\Psi_{cryst}\rangle = \prod_k |\Psi_k\rangle \qquad (1)$$

where all the crystal-unit wave functions $|\Psi_k\rangle$ are formally identical and related to each other through the crystal symmetry operations. The choice of the functional form for $|\Psi_k\rangle$ is completely arbitrary and it can be considered as a further assumption of the technique since it will eventually determine the type of X-ray constrained wave function (e.g., Hartree-Fock, ELMO, CI, MCSCF, etc.) that is desired.

Considering all the non-interacting units as symmetry-unique portions of the crystal unit-cell, the unit-cell electron distribution can be simply computed as sum of N_m crystal-unit charge densities $\rho_k(\boldsymbol{r})$ that are related to reference electron density $\rho_0(\boldsymbol{r})$ through the unit-cell symmetry operations $\{\boldsymbol{R}_k, \boldsymbol{r}_k\}$:

$$\rho_{cell}(\boldsymbol{r}) = \sum_{j=1}^{N_m} \rho_j(\boldsymbol{r}) = \sum_{j=1}^{N_m} \rho_0\left[\boldsymbol{R}_j^{-1}(\boldsymbol{r} - \boldsymbol{r}_j)\right] \qquad (2)$$

Charge distribution $\rho_0(\boldsymbol{r})$ is associated with wave function $|\Psi_0\rangle$ for the reference unit. Following Jayatilaka, this wave function is obtained not only minimizing the energy of the reference crystal-unit, but also reproducing a set of experimental structure factor amplitudes. In other words, $|\Psi_0\rangle$ is the wave function that minimizes the following functional:

$$J[\Psi_0] = \langle \Psi_0 | \hat{H}_0 | \Psi_0 \rangle + \lambda(\chi^2 - \Delta) = E_0[\Psi_0] + \lambda(\chi^2[\Psi_0] - \Delta) \qquad (3)$$

with $\hat{H}_0$ as the non-relativistic Hamiltonian operator for the reference unit, while the second term considers the constraint of the experimental data. In particular, λ is an external multiplier that is manually adjusted during the calculations and that gives the strength of the experimental constraints, Δ is the desired agreement between theoretical and observed values (usually set equal to 1) and χ^2 represents a measure of the statistical agreement between the calculated and the theoretical structure factors amplitudes:

$$\chi^2 = \frac{1}{N_r - N_p} \sum_{\boldsymbol{h}} \frac{\left(\eta\left|F_{\boldsymbol{h}}^{calc}\right| - \left|F_{\boldsymbol{h}}^{exp}\right|\right)^2}{\sigma_{\boldsymbol{h}}^2} \qquad (4)$$

It is worthwhile to point out that it is the presence of the experimental constraint in functional $J[\Psi_0]$ that allows to fulfil the starting assumption that the global electron density of the fictitious non-interacting system is identical to the one of the real interacting crystal. Of course, the accuracy of the assumption is strictly related to the quality and completeness of the experimental X-ray diffraction data used in the calculations.

4.2 X-RAY CONSTRAINED SPIN-COUPLED THEORY AND APPLICATION

Before starting this section, two disclaimers are necessary:

- Some of the equations treated in the previous section will be repeated for sake of clarity
- The theory of the XCSC approach has been mainly developed by Dr. Alessandro Genoni. My main duties within this project (mainly carried out during my stay in Metz at University of Lorraine) have been the following: to interface the existing SC program[108] with the XCW part, to test and debug the new XCSC software and, then, to apply it in order to study a well-known crystalline system, with the aim of testing the potentiality of this new method.[31]

As is well known, in theoretical chemistry there exist two main approaches to investigate molecular electronic structure: the Valence Bond (VB) and the Molecular Orbital (MO) theories. The former has been strictly related to the traditional chemical perception since its origin and significantly contributed to the definition of concepts (e.g., Lewis structures, resonance structure, hybridization, local bonds, electronegativity, *etc.*) that, even today, are of customary use among chemists and constitute the basis of the traditional chemical reasoning to interpret bonding and reactivity. On the contrary, the latter provides pictures of the electronic structure that are generally delocalized over the whole molecules under exam and that are consequently far from the traditional chemical notions. Despite this fact, the MO-based methods have become more and more predominant in electronic structure investigations, mainly due to their high predictive power, their intrinsic lower computational cost (at least for the basic strategies) and the ease with which they could be implemented into working computer codes. Nevertheless, owing to the unquestionable higher chemical interpretability associated with the VB theory, different Valence Bond approaches have been continuously proposed over the years, each of them with its own features and with its main fields of application. Herein, it will be particularly considered the Spin-Coupled (SC) method,[106–108] a technique that uses a very general single configuration-type wave function by including all the possible spin-coupling modes and without imposing any constraints (e.g., orthogonality constraints) on the orbitals expansions. This

approach provides a correlated description of the electronic structure, but still interpretable in terms of one-particle functions. For example, from the shapes of the SC orbitals it is generally possible to draw conclusions on the spatial arrangements of the electronic clouds and the hybridization of atoms. Furthermore, from the weights associated with the different spin-coupling modes, one can get insights into the relative importance of the resonance structures for the molecule under exam.

Given the wealth of traditional chemical information intrinsically contained in the SC wave functions, the idea at the basis of the method proposed in this chapter is to combine the original Spin-Coupled method with Jayatilaka's X-ray constrained wave function (XCW) approach in order to directly extract the same kind of information from experimental X-ray diffraction data. In fact, nowadays, the XCW strategy is the most reliable and widely used method among the techniques that aim at obtaining wave functions or density matrices compatible with experimental diffraction or scattering measurements.[119,120] It mainly consists in determining wave functions that not only minimize the energy of the investigated systems, but that also maximize the agreement between calculated and experimental structure factors amplitudes. So far, the approach has been mainly proposed within the Molecular Orbital theory, especially in the framework of the Hartree-Fock formalism,[113,116] but also including relativistic corrections.[121] Therefore, in its original form, the Jayatilaka strategy generally provides completely delocalized pictures of electronic structures that can be rationalized in terms of traditional chemical concepts by only applying *a posteriori* Quantum Chemical Topology methods, such as the Quantum Theory of Atoms in Molecules (QTAIM),[122] the Electron Localization Function (ELF),[123] the Electron Localizability Indicator (ELI)[124] and the Localized Orbital Locator (LOL).[125] The only attempts to recover the traditional chemical perception in the context of the XCW approach without resorting to *a posteriori* techniques are the more recent XC-ELMO[100,126,127] and XC-ELMO-VB[104,128] strategies. Nevertheless, in the former, Extremely Localized Molecular Orbitals[97,98,103] (ELMOs) corresponding to atoms, bonds and functional groups are directly extracted from X-ray diffraction data, but a localization scheme is actually imposed *a priori* on the electronic structure before starting the calculations. In the latter, only the weights of resonance structures are determined

from the experimental data, while the Slater determinants (and consequently the orbitals) used for the expansion of a pseudo Valence Bond wave function are obtained by means of preliminary ELMO calculations and are strictly kept frozen during the minimization-fitting process. Therefore, in this method, it is introduced a technique (from now indicated as X-ray constrained Spin-Coupled (XCSC) technique) that goes beyond the limitations of the previous two methods. In fact, by using a SC wave function *ansatz* in the context of the XCW approach, it is possible at simultaneously obtaining Spin-Coupled orbitals and weights of resonance structures that are compatible with the collected X-ray diffraction data and not biased by information introduced *a priori*. Furthermore, unlike the XC-ELMO-VB strategy, through the new XCSC method it can be also considered all the possible spin-coupling modes associated with the spin-state of the system under exam.

In analogy with original Jayatilaka's approach, also in the new X-ray constrained Spin-Coupled technique it has been assumed to work with a fictitious molecular crystal constituted by non-interacting molecular units, each of them described by formally identical and symmetry related wave functions. Under this assumption and the additional hypothesis that each non-interacting unit corresponds to a symmetry-unique portion of the crystal unit-cell, the unit-cell electron density can be written as a sum of N_m crystal-unit electron densities $\rho_j(\boldsymbol{r})$ related to the reference distribution $\rho_0(\boldsymbol{r})$ through the unit-cell symmetry operations $\{\boldsymbol{R}_j, \boldsymbol{r}_j\}$:

$$\rho_{cell}(\boldsymbol{r}) = \sum_{j=1}^{N_m} \rho_j(\boldsymbol{r}) = \sum_{j=1}^{N_m} \rho_0\left[\boldsymbol{R}_j^{-1}(\boldsymbol{r} - \boldsymbol{r}_j)\right] \qquad (1)$$

Equation (1) is exact if and only if electron density $\rho_0(\boldsymbol{r})$ is not obtained through an isolated computation on the reference crystal-unit. To fulfill this condition, in the XCW approaches $\rho_0(\boldsymbol{r})$ corresponds to the reference molecular-unit wave function Ψ_0 that not only minimizes the energy of the reference crystal unit, but that also reproduces a set of experimental structure factors amplitudes $\{|F_{\boldsymbol{h}}^{exp}|\}$ within the limit imposed by the experimental uncertainties.

In the novel XCSC method, wave function Ψ_0 for the reference unit has the analytical form of a Spin-Coupled wave function for a system of N electrons in the spin-state (S, M), as described in the previous chapter:

$$\Psi_0 = \sum_{k=1}^{f_S^N} c_{S,k}\, \psi_{S,M;k}^N = \sum_{k=1}^{f_S^N} c_{S,k}\, \mathcal{A}\left(\mathbf{\Phi}\, \Theta_{S,M;k}^N\right) \qquad (2)$$

or:

$$\Psi_0 = \sum_{k=1}^{f_S^{Nv}} c_{S,k}\, \psi_{S,M;k}^N = \sum_{k=1}^{f_S^{Nv}} c_{S,k}\, \mathcal{A}\left(\phi_1^c\, \bar{\phi}_1^c \ldots \phi_i^c\, \bar{\phi}_i^c \ldots \phi_{N_1}^c\, \bar{\phi}_{N_1}^c\, \mathbf{\Phi}_{\mathrm{v}}\, \Theta_{S,M;k}^{N_v}\right) \qquad (3)$$

Equation (3) is actually the one currently used as *ansatz* in the new X-ray constrained Spin-Coupled approach and, considering that the active SC orbitals are expanded over traditional basis-sets of Quantum Chemistry $\{\chi_\mu\}_{\mu=1}^M$, namely

$$\phi_i(\boldsymbol{r}) = \sum_{\mu=1}^{M} C_{\mu i}\, \chi_\mu(\boldsymbol{r}) \qquad (4),$$

the goal of the new technique is to find the coefficients $\{C_{\mu i}\}$ of the Spin-Coupled orbitals expansions and the spin-coupling coefficients $\{c_{S,k}\}$ that minimize the following functional:

$$J[\{C_{\mu i}\}, \{c_{S,k}\}] = W[\{C_{\mu i}\}, \{c_{S,k}\}] + \lambda\left(\chi^2[\{C_{\mu i}\}, \{c_{S,k}\}] - \Delta\right) \qquad (5).$$

In equation (5), the first term W is the energy part of the functional, namely

$$W[\{C_{\mu i}\}, \{c_{S,k}\}] = \frac{\langle \Psi_0 | \widehat{H}_0 | \Psi_0 \rangle}{\langle \Psi_0 | \Psi_0 \rangle} \qquad (6),$$

with $\widehat{H}_0$ as the non-relativistic Hamiltonian operator for the reference unit, while the second term takes into account the constraint of the experimental data. In particular, λ is an external multiplier that is manually adjusted during the calculations and that gives the strength of the experimental constraints, Δ is the desired agreement between theoretical and observed values (usually set equal to

1) and χ^2 represents a measure of the statistical agreement between the calculated and the theoretical structure factors amplitudes:

$$\chi^2 = \frac{1}{N_r - N_p} \sum_{\boldsymbol{h}} \frac{\left(\eta \left|F_{\boldsymbol{h}}^{calc}\right| - \left|F_{\boldsymbol{h}}^{exp}\right|\right)^2}{\sigma_{\boldsymbol{h}}^2} \qquad (7)$$

with N_r as the number of reflections used as external constrains, N_p as the number of adjustable parameters, $\boldsymbol{h}$ as the triad of Miller indexes labeling the reflection, $\sigma_{\boldsymbol{h}}$ as the experimental uncertainty associated with the generic experimental structure factor amplitude $\left|F_{\boldsymbol{h}}^{exp}\right|$ and η as an overall scale-factor, which is determined by minimizing the χ^2 value and which multiplies each computed structure factor amplitude $\left|F_{\boldsymbol{h}}^{calc}\right|$.

In order to determine the Spin-Coupled orbitals and the spin-coupling coefficients that minimize functional (5), it has been implemented the new XCSC method in a working Spin-Coupled program[108] that uses a second-order protocol based on a modified Newton-Raphson minimization scheme and that particularly exploits a minimization-algorithm proposed by Goldfield *et al.*[129] In this algorithm, first and second derivatives of functional (5) are computed analytically and convergence is considered attained when the norm of the gradient is lower than $1 \cdot 10^{-6}$ and all the eigenvalues of the Hessian are positive.

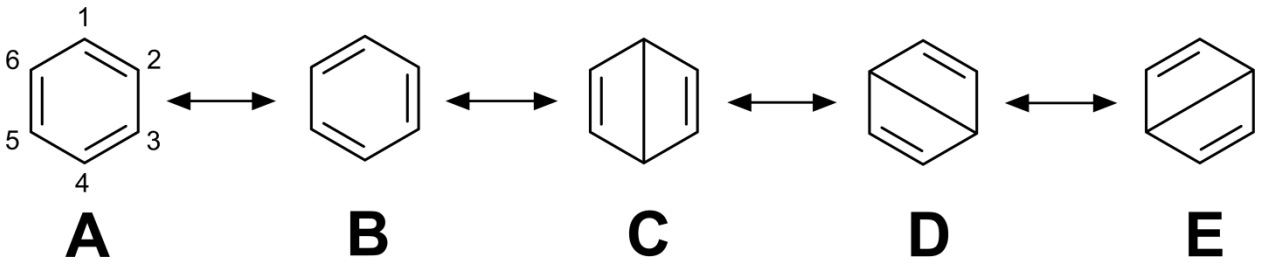

Figure 2. Spin-Coupled/resonance structures of benzene considered in the unconstrained and X-ray constrained Spin-Coupled calculations (A-B: Kekulé resonance structures; C-E: Dewar resonance structures). The adopted labels for the carbon atoms of the aromatic ring are also shown in structure A.

The X-ray constrained Spin-Coupled technique has been afterwards tested exploiting the high-resolution X-ray diffraction data collected for benzene at 100 K by Bürgi and coworkers.[130] In

particular, using the crystallographic geometry it has been carried out both traditional and X-ray constrained Spin-Coupled calculations with the DZP-Dunning basis-set. For both types of Spin-Coupled computations, only the 6 π electrons of the aromatic ring have been considered as active electrons and have thus been described by means of SC orbitals, while both the core electrons of the carbon atoms and the electrons associated with the C-H and C-C σ bonds of the molecule have been described with frozen doubly occupied molecular orbitals initially obtained from RHF calculations. Furthermore, as described in the theory section on Chapter 3, the 6 active electrons of the system in the singlet state have been Spin-Coupled in 5 different ways, which correspond to the 5 Spin-Coupled structures considered in our unconstrained and X-ray constrained SC computations and, consequently, to the 5 possible resonance structures of benzene shown in Figure 2. The first two correspond to the traditional Kekulé resonance structures (see Figures 2A and 2B), while the other three are those of Dewar (see Figures 2C-2E). Finally, only for the XCSC calculations, it has been exploited the unit-cell data, the Anisotropic Displacement Parameters (ADPs) and all the structure factors amplitudes associated with the crystallographic structure of benzene (particularly, 2412 structure factor amplitudes used as constraints). The X-ray constrained calculations have been carried out by progressively varying the external multiplier λ from 0 (unconstrained Spin-Coupled calculation) to 1 with steps of 0.05. To this purpose it is worth noting that, in the X-ray constrained wave function computations, the convergence towards the desired statistical agreement (generally, $\chi^2 = 1$) is sometimes slow and complicated. Therefore, in order not to push our XCSC calculations until quite large values of λ that might provide only minimal improvements of the χ^2 statistical agreement and sometimes even unphysical changes in the energy and in the electron density distribution, it has been decided to stop the XCSC minimization-fitting process by adopting the empirical termination criteria already proposed to establish the end of the XC-ELMO calculations:

$$\begin{cases} \chi^2 \leq 1 \\ \left|\dfrac{\chi_i^2 - \chi_{i-1}^2}{\lambda_i - \lambda_{i-1}}\right| < 0.5 \\ \dfrac{\left|E_{\lambda_i}^{el} - E_{\lambda=0}^{el}\right|}{\left|E_{\lambda=0}^{el}\right|} > 5 \cdot 10^{-4} \end{cases} \qquad (8)$$

As in the XC-ELMO method, the XCSC computations are terminated when one of the three previous conditions is fulfilled. The first one is the traditional and desirable one, namely calculations were stopped when the statistical agreement $\chi^2 = 1$ was reached. The second condition checks the incremental ratio of χ^2 with respect to λ in order to avoid minimal changes of the agreement statistics when the external multiplier increases, while the third one controls that the XCSC electronic energy does not increase excessively compared to the corresponding unconstrained value.

After performing the XCSC calculations, it has initially considered the trend of χ^2 in function of the external multiplier λ. In Figure 3 it is possible to observe that, as in any X-ray constrained wave function computation, the statistical agreement decreases monotonically as λ increases and the first steps are the ones characterized by the sharpest decreases in the χ^2 value. Furthermore, it can also be noted that, in this case, the XCSC calculations were slowly converging towards $\chi^2 = 1$. Due to the fulfillment of the second criterion in equation (8), it has been thus decided to stop the calculations at $\lambda = 0.40$, as indicated by the vertical red dotted line depicted in Figure 3. For the sake of completeness, the χ^2 values resulting from the unconstrained and X-ray constrained Spin-Coupled calculations are reported in Table 1 together with the corresponding electronic energies. As already observed for other XCW strategies, also in the Spin-Coupled case, the energy associated with the experimentally constrained wave function is higher than the corresponding unconstrained energy. This is due to the fact that, when an X-ray constrained Spin-Coupled wave function is determined, additional constraints are introduced without taking into account new variational parameters. Therefore, the obtained Spin-Coupled orbitals and spin-coupling coefficients correspond to a minimum point on the hyper-surface of functional (5) and not to a minimum point for the energy of the system.

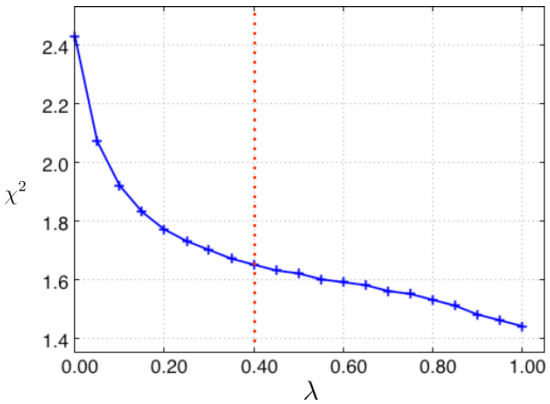

Figure 3. Variation of the χ^2 statistical agreement in function of the external multiplier λ for the X-ray constrained Spin-Coupled calculations.

Table 1. χ^2 statistical agreement and electronic energy values for the analyzed unconstrained and X-ray constrained Spin-Coupled wave functions.

Method	χ^2	Energy (E_h)
Spin-Coupled	2.43	-230.808252
XCSC ($\lambda = 0.20$)	1.77	-230.778317
XCSC ($\lambda = 0.40$)	1.65	-230.752291

After the previous standard analysis, it has been studied more in detail the effects of the experimental constraints on the Spin-Coupled wave function by comparing the results of the unconstrained and X-ray constrained Spin-Coupled calculations. Furthermore, in order to better show how the effects of the X-ray diffraction data are progressively considered in the computations, in our comparisons it has not considered only the converged XCSC wave function, but also the intermediate one obtained for $\lambda = 0.20$.

Initially the attention was focused on the Spin-Coupled orbitals and, in Figure 4, other than depicting the unconstrained (symmetry unique) ones, it has also been shown their differences with those resulting from the X-ray constrained calculations. It is easy to observe that, for all the orbitals, the main effect of the experimental X-ray diffraction data is a shift of the electronic clouds from the bonding regions to the carbon atoms. In other words, the XCSC orbitals are more localized on the carbon atoms than the corresponding unconstrained ones. Moreover, it is also possible to note that

the effect becomes more and more significant as λ increases, namely as the experimental constraints become more and more important.

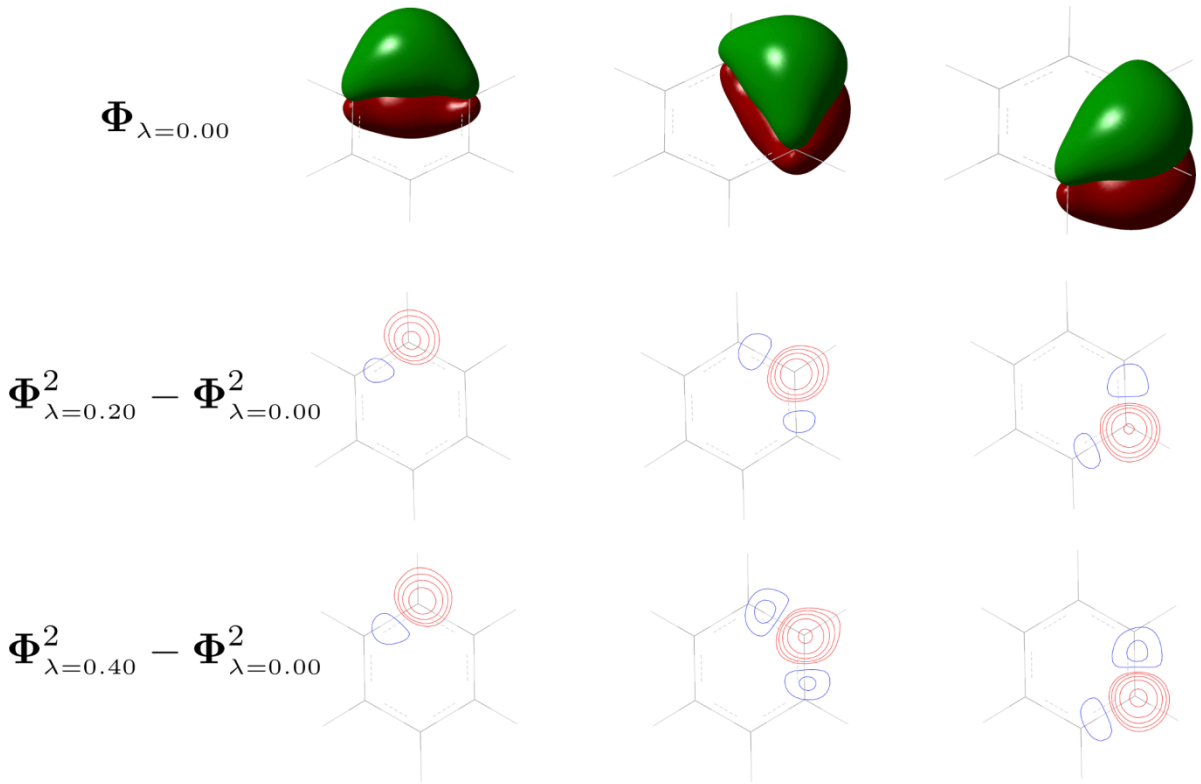

Figure 4. First row: three-dimensional plots of the symmetry unique unconstrained Spin-Coupled orbitals (0.06 e/bohr^3 isovalues are plotted). Second row: two-dimensional plots of the differences between the square moduli of the X-ray constrained ($\lambda = 0.20$) and unconstrained Spin-Coupled orbitals. Third row: two-dimensional plots of the differences between the square moduli of the X-ray constrained ($\lambda = 0.40$) and unconstrained Spin-Coupled orbitals. For each two-dimensional plot, the contours are drawn at $\pm 1 \cdot 10^{-3}$ e/bohr^3 and at $\pm 2, 4, 8 \cdot 10^{n}$ e/bohr^3 (with n as an integer ranging from -3 to 0) in a plane parallel to and 0.5 Å above the one defined by the carbon atom on which the orbital is mainly localized and the other two carbon atoms bonded to it. Red and blue contours indicate positive and negative values, respectively.

At a second stage the attention has also been focused on the spin-coupling coefficients and, more particularly, on the corresponding Chirgwin-Coulson weights that directly measure the relative importance of the different resonance structures. As it can be observed in Table 2, in gas phase (namely, in the unconstrained Spin-Coupled wave functions) the resonance structures that have a predominant weight are the Kekulé ones, each of them contributing for about 40% (note that the

labels of the structures correspond to those indicated in Figure 2). Nevertheless, after introduction of the experimental constraints in the computations, structures A and B still remain the most significant, but they gradually lose their importance in favor of a Dewar resonance structure (particularly, resonance structure E) whose weight passes from about 6% in gas phase to 9% in the intermediate XCSC wave function ($\lambda = 0.20$) and to about 11% in the final XCSC wave function ($\lambda = 0.40$).

Table 2. Chirgwin-Coulson weights (in %) of the benzene Spin-Coupled/resonance structures, as obtained from unconstrained ($\lambda = 0.0$) and X-ray constrained Spin-Coupled calculations.

	Chirgwin-Coulson weights		
Resonance Structure	$\lambda = 0.0$	$\lambda = 0.20$	$\lambda = 0.40$
A	40.45	39.13	38.22
B	40.45	39.17	38.26
C	6.34	5.90	5.63
D	6.23	6.79	6.76
E	6.53	9.01	11.12

Finally, to further study the effects of the wave function fitting, it has also been compared the unconstrained Spin-Coupled electron densities with the XCSC ones obtained for $\lambda = 0.20$ and $\lambda = 0.40$. In Figure 5 are plotted the differences between the X-ray constrained electron distributions and the reference unconstrained Spin-Coupled electron distributions both on a plane above the aromatic ring (first row in Figure 5) and on a plane below the aromatic ring (second row in Figure 5). The reason behind these plots of the differences both above and below the benzene aromatic ring is to show that the difference-maps fully respect the symmetry of the inversion center of the molecule. In fact, the benzene crystallographic geometry used for our calculations is not exactly planar and the plots only on one side of the ring result in non-centrosymmetric pictures. However, the differences shown in Figure 5 indicate that the introduction of the constraint of the X-ray diffraction data entails a redistribution of the molecular electron density, mainly from the C-C bonds to the carbon atoms, thus confirming what it has already been observed by analyzing the differences between the unconstrained and X-ray constrained SC orbitals. Furthermore, also in this case, it can be noted that

the entity of the charge redistribution increases as the experimental constraints become more and more important in the functional to minimize.

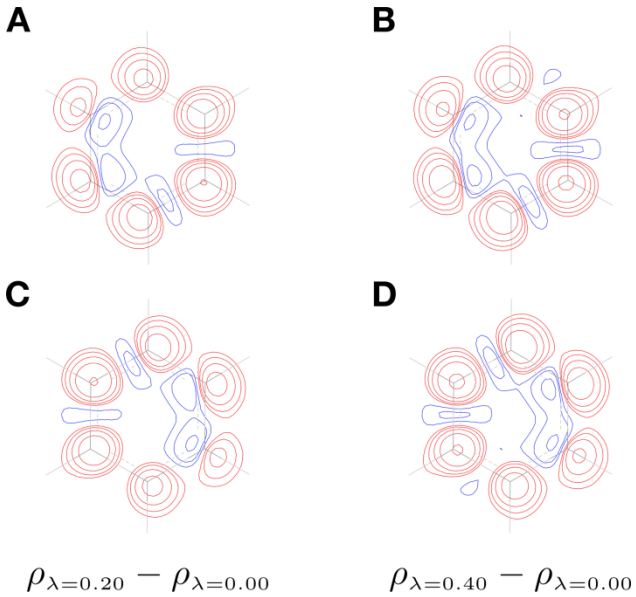

Figure 5. Two-dimensional plots of the differences between X-ray constrained and unconstrained Spin-Coupled electron densities. Plots above the aromatic ring (in a plane parallel to and 0.5 Å above the one defined by atoms C1, C2 and C6): (A) $\rho_{XCSC/\lambda=0.20} - \rho_{SC/\lambda=0.00}$, (B) $\rho_{XCSC/\lambda=0.40} - \rho_{SC/\lambda=0.00}$. Plots below the aromatic ring (in a plane parallel to and 0.5 Å below the one defined by atoms C1, C2 and C6): (C) $\rho_{XCSC/\lambda=0.20} - \rho_{SC/\lambda=0.00}$, (B) (D) $\rho_{XCSC/\lambda=0.40} - \rho_{SC/\lambda=0.00}$. For each plot the contours are drawn at $\pm 1 \cdot 10^{-3}$ e/bohr^3 and at $\pm 2, 4, 8 \cdot 10^{n}$ e/bohr^3 (with n as an integer ranging from -3 to 0). Red and blue contours indicate positive and negative values, respectively.

To summarize, in this chapter it has been proposed the first fully VB-like X-ray constrained wave function method. The new technique allows the extraction of traditional chemical information (e.g., weights of the resonance structures, spatial extensions of the electronic clouds around the atoms) from X-ray diffraction data, information that cannot be generally obtained through usual strategies of Quantum Crystallography, such as the more traditional multipole model methods or other wave function-based approaches. This preliminary test calculations on benzene have shown that the new technique is indeed able to significantly capture the crystal field effects on the electronic structure, as testified by the observed differences in the obtained Spin-Coupled orbitals, by the variation of the resonance structure weights and the global changes in the electron density distribution. Furthermore,

since the Spin-Coupled wave functions are exact spin-eigenfunctions also for open-shell systems, it can be envisaged the further extension of the method to perform simultaneous refinements of X-ray and Polarized Neutron diffraction data, as alternative to the strategies already devised both in the framework of the multipole models of charge density and in the context of the wave functions-based techniques to obtain experimental spin densities. Finally, it is also worth noting that, if the very preliminary XC-ELMO-VB strategy is excluded, the new method can be really considered as the first multi-determinant X-ray constrained wave function method. For this reason, the new approach could be also exploited in the near future to extract two-electron density matrices from scattering experiment, but also to investigate more precisely if the XCW approach is able to capture electron correlation from X-ray diffraction data, a still open problem that, so far, has been faced only in an effective way by mainly analyzing the effects of the wave function fitting on the electron density. Several efforts have to be done to improve this technique: one of this is the improvement of the spin-couple code to treat bigger molecular crystalline systems and to reduce the computational cost of the calculations. Moreover, very high-quality diffraction data have to be used to obtain chemically meaningful results. However, the performances of the technique illustrated in this chapter are very promising and the author strongly believe that this tool will be of great help in the development of crystal engineering. Eventually, it can also be exploited to study halogen bonded crystalline systems.

BIBLIOGRAPHY

1. Cavallo, G. *et al.* The Halogen Bond. *Chem. Rev.* **116,** 2478–2601 (2016).
2. Chemistry International -- Newsmagazine for IUPAC. Available at: http://www.iupac.org/publications/ci/2010/3202/pp1_2009-032-1-100.html. (Accessed: 2nd August 2018)
3. Desiraju, G. R. *et al.* Definition of the halogen bond (IUPAC Recommendations 2013). *Pure Appl. Chem.* **85,** 1711–1713 (2013).
4. Metrangolo, P. (Pierangelo), Resnati, G. (Giuseppe) & Arman, H. D. (Hadi D. . *Halogen bonding : fundamentals and applications*. (Springer, 2008).
5. Metrangolo, P. & Resnati, G. CHEMISTRY: Halogen Versus Hydrogen. *Science (80-.).* **321,** 918–919 (2008).
6. Ramasubbu, N., Parthasarathy, R. & Murray-Rust, P. Angular Preferences of Intermolecular Forces around Halogens Centers: Preferred Directions of Approach of Electrophiles and Nucleophiles around the Carbon-Halogen Bond. *J. Am. Chem. Soc.* **108,** 4308–4314 (1986).
7. Dumas, J.-M., Gomel, M. & Guerin, M. Molecular interactions involving organic halides. in *Halides, Pseudo-Halides and Azides: Part 2 (1983)* 985–1020 (John Wiley & Sons, Ltd.). doi:10.1002/9780470771723.ch2
8. Forni, A., Rendine, S., Pieraccini, S. & Sironi, M. Solvent effect on halogen bonding: The case of the I···O interaction. *J. Mol. Graph. Model.* **38,** 31–39 (2012).
9. Legon, A. C. Prereactive Complexes of Dihalogens XY with Lewis Bases B in the Gas Phase: A Systematic Case for the Halogen Analogue B···XY of the Hydrogen Bond B···HX. *Angew. Chemie Int. Ed.* **38,** 2686–2714 (1999).
10. Lu, Y., Wang, Y. & Zhu, W. Nonbonding interactions of organic halogens in biological systems: implications for drug discovery and biomolecular design. *Phys. Chem. Chem. Phys.* **12,** 4543 (2010).
11. Auffinger, P., Hays, F. A., Westhof, E. & Ho, P. S. Halogen bonds in biological molecules. *Proc. Natl. Acad. Sci. U. S. A.* (2004). doi:10.1073/pnas.0407607101
12. Voth, A. R., Hays, F. A. & Ho, P. S. Directing macromolecular conformation through halogen bonds. *Proc. Natl. Acad. Sci.* (2007). doi:10.1073/pnas.0610531104
13. Cariati, E. *et al.* Tuning second-order NLO responses through halogen bonding. *Chem. Commun.* **0,** 2590 (2007).
14. Cariati, E. *et al.* Self-Complementary Nonlinear Optical-Phores Targeted to Halogen Bond-Driven Self-Assembly of Electro-Optic Materials. *Cryst. Growth Des.* **11,** 5642–5648 (2011).
15. Mango, D. *et al.* Electrophysiological and metabolic effects of CHF5074 in the hippocampus: Protection against in vitro ischemia. *Pharmacol. Res.* **81,** 83–90 (2014).
16. Andrea Mele, †, Pierangelo Metrangolo, *,†, Hannes Neukirch, †, Tullio Pilati, ‡ and & Giuseppe Resnati*, †. A Halogen-Bonding-Based Heteroditopic Receptor for Alkali Metal Halides. (2005). doi:10.1021/JA054862H
17. Beale, T. M., Chudzinski, M. G., Sarwar, M. G. & Taylor, M. S. Halogen bonding in solution: thermodynamics and applications. *Chem. Soc. Rev.* **42,** 1667–1680 (2013).
18. Thallapally, P. K. *et al.* 1,3-Dibromo-2,4,6-trinitrobenzene (DBTNB). Crystal engineering and perfect polar alignment of two-dimensional hyperpolarizable chromophores. *Chem. Commun.* **0,** 1052–1053 (2002).
19. Mukherjee, A., Tothadi, S. & Desiraju, G. R. Halogen Bonds in Crystal Engineering: Like Hydrogen Bonds yet Different. *Acc. Chem. Res.* **47,** 2514–2524 (2014).

20. Rendine, S., Pieraccini, S., Forni, A. & Sironi, M. Halogen bonding in ligand–receptor systems in the framework of classical force fields. *Phys. Chem. Chem. Phys.* **13,** 19508 (2011).
21. Ibrahim, M. A. A. Molecular mechanical study of halogen bonding in drug discovery. *J. Comput. Chem.* **32,** 2564–2574 (2011).
22. Clark, T., Hennemann, M., Murray, J. S. & Politzer, P. Halogen bonding: the σ-hole. *J. Mol. Model.* **13,** 291–296 (2007).
23. Brinck, T., Murray, J. S. & Politzer, P. Surface electrostatic potentials of halogenated methanes as indicators of directional intermolecular interactions. *Int. J. Quantum Chem.* **44,** 57–64 (1992).
24. Eskandari, K. & Zariny, H. Halogen bonding: A lump–hole interaction. *Chem. Phys. Lett.* **492,** 9–13 (2010).
25. Bader, R. F. W. *Atoms in molecules : a quantum theory*. (Clarendon Press, 1990).
26. Koritsanszky†, T. S. & Coppens*, P. Chemical Applications of X-ray Charge-Density Analysis. (2001). doi:10.1021/CR990112C
27. Tognetti, V. & Joubert, L. Electron density Laplacian and halogen bonds. *Theor. Chem. Acc.* **134,** 90 (2015).
28. Massa, L., Huang, L. & Karle, J. Quantum crystallography and the use of kernel projector matrices. *Int. J. Quantum Chem.* **56,** 371–384 (1995).
29. Grabowsky, S., Genoni, A. & Bürgi, H.-B. Quantum crystallography. *Chem. Sci.* **8,** 4159–4176 (2017).
30. QUANTUM CRYSTALLOGRAPHY DISCUSSION MEETING - CECAM Discussion Meeting on Quantum Crystallography. Available at: https://qcrystcecam.weebly.com/.
31. Genoni, A., Franchini, D., Pieraccini, S. & Sironi, M. X-ray constrained Spin-Coupled wavefunction: a new tool to extract chemical information from X-ray diffraction data. *Chem. - A Eur. J.* (2018). doi:10.1002/chem.201803988
32. Bianchi, R., Forni, A. & Pilati, T. The Experimental Electron Density Distribution in the Complex of (E)-1,2-Bis(4-pyridyl)ethylene with 1,4-Diiodotetrafluorobenzene at 90 K. *Chem. - A Eur. J.* **9,** 1631–1638 (2003).
33. Bianchi, R., Forni, A., Pilati, T. & IUCr. Experimental electron density study of the supramolecular aggregation between 4,4'-dipyridyl- *N* , *N* '-dioxide and 1,4-diiodotetrafluorobenzene at 90 K. *Acta Crystallogr. Sect. B Struct. Sci.* **60,** 559–568 (2004).
34. Ansgar Bach, *,†, Dieter Lentz, ‡ and & Luger†, P. Charge Density and Topological Analysis of Pentafluorobenzoic Acid. (2001). doi:10.1021/JP004626N
35. David E. Hibbs, *,†, Jacob Overgaard, †, James A. Platts, ‡, Mark P. Waller, † and & Hursthouse§, M. B. Experimental and Theoretical Charge Density Studies of Tetrafluorophthalonitrile and Tetrafluoroisophthalonitrile. (2004). doi:10.1021/JP037700L
36. Deepak Chopra, †, T. S. Cameron, ‡, Joseph D. Ferrara, § and & Tayur N. Guru Row*, †. Pointers toward the Occurrence of C−F···F−C Interaction: Experimental Charge Density Analysis of 1-(4-Fluorophenyl)-3,6,6-trimethyl-2-phenyl-1,5,6,7-tetrahydro-4H-indol-4-one and 1-(4-Fluorophenyl)-6-methoxy-2-phenyl-1,2,3,4-tetrahydroisoquinoline. (2006). doi:10.1021/JP0625309
37. Hathwar, V. R. & Guru Row, T. N. Charge Density Analysis of Heterohalogen (Cl···F) and Homohalogen (F···F) Intermolecular Interactions in Molecular Crystals: Importance of the Extent of Polarizability. *Cryst. Growth Des.* **11,** 1338–1346 (2011).
38. Pavan, M. S., Durga Prasad, K. & Guru Row, T. N. Halogen bonding in fluorine: experimental charge density study on intermolecular F···F and F···S donor–acceptor contacts. *Chem. Commun.* **49,** 7558 (2013).
39. Johansson, M. P. & Swart, M. Intramolecular halogen–halogen bonds? *Phys. Chem. Chem.*

Phys. **15,** 11543 (2013).
40. Tognetti, V., Yahia-Ouahmed, M. & Joubert, L. Comment on "Analysis of CF···FC Interactions on Cyclohexane and Naphthalene Frameworks". *J. Phys. Chem. A* **118,** 9791–9792 (2014).
41. Chopra, D. & Row, T. N. G. Role of organic fluorine in crystal engineering. *CrystEngComm* **13,** 2175 (2011).
42. Simonetta, M., Gianinetti, E. & Vandoni, I. Valence-Bond Theory for Simple Hydrocarbon Molecules, Radicals, and Ions. *J. Chem. Phys.* **48,** 1579–1594 (1968).
43. Hansen, N. K., Coppens, P. & IUCr. Testing aspherical atom refinements on small-molecule data sets. *Acta Crystallogr. Sect. A* **34,** 909–921 (1978).
44. M. A. Blanco, *, A. Martín Pendás, and & Francisco, E. Interacting Quantum Atoms: A Correlated Energy Decomposition Scheme Based on the Quantum Theory of Atoms in Molecules. (2005). doi:10.1021/CT0501093
45. Popelier, P. L. A. The QTAIM Perspective of Chemical Bonding. in *The Chemical Bond: Fundamental Aspects of Chemical Bonding* (2014). doi:10.1002/9783527664696.ch8
46. No Title. *Bruker (2012). Progr. name(s). Bruker AXS Inc., Madison, Wisconsin, USA. [Older versions should Ref. to Siemens Anal. X-ray Instruments Inc. instead Bruker AXS.]*
47. Bruker (2001). Program name. Bruker AXS Inc., Madison, Wisconsin, U. No Title.
48. Sheldrick, G. M. Experimental phasing with SHELXC/D/E: combining chain tracing with density modification. *Acta Cryst. D* 479–485. (2010).
49. Bianchi, R., Forni, A. & IUCr. *VALTOPO* : a program for the determination of atomic and molecular properties from experimental electron densities. *J. Appl. Crystallogr.* **38,** 232–236 (2005).
50. Forni, A. Experimental and Theoretical Study of the Br···N Halogen Bond in Complexes of 1,4-Dibromotetrafluorobenzene with Dipyridyl Derivatives. *J. Phys. Chem. A* **113,** 3403–3412 (2009).
51. Stewart, R. F., Bentley, J. & Goodman, B. Generalized x-ray scattering factors in diatomic molecules. *J. Chem. Phys.* **63,** 3786 (1975).
52. Becker, P. J. & Coppens, P. Extinction within the limit of validity of the Darwin transfer equations. I. General formalism for primary and secondary extinction and their applications to spherical crystals. *Acta Crystallogr. Sect. A* **30,** 129–147 (1974).
53. Frisch, M. J. *et al.* Gaussian09. *Gaussian 09* (2009).
54. Forni, A., Pieraccini, S., Franchini, D. & Sironi, M. Assessment of DFT functionals for QTAIM topological analysis of halogen bonds with benzene. *J. Phys. Chem. A* (2016). doi:10.1021/acs.jpca.6b07578
55. Forni, A., Pieraccini, S., Rendine, S., Gabas, F. & Sironi, M. Halogen-Bonding Interactions with π Systems: CCSD(T), MP2, and DFT Calculations. *ChemPhysChem* **13,** 4224–4234 (2012).
56. Forni, A., Pieraccini, S., Rendine, S. & Sironi, M. Halogen bonds with benzene: An assessment of DFT functionals. *J. Comput. Chem.* **35,** 386–394 (2014).
57. Riley, K. E. & Hobza, P. The relative roles of electrostatics and dispersion in the stabilization of halogen bonds. *Phys. Chem. Chem. Phys.* **15,** 17742–17751 (2013).
58. Feller, D. The role of databases in support of computational chemistry calculations. *J. Comput. Chem.* **17,** 1571–1586 (1996).
59. Karen L. Schuchardt, *,† *et al.* Basis Set Exchange: A Community Database for Computational Sciences. (2007). doi:10.1021/CI600510J
60. Glukhovtsev, M. N., Pross, A., McGrath, M. P. & Radom, L. Extension of Gaussian-2 (G2) theory to bromine- and iodine-containing molecules: Use of effective core potentials. *J. Chem. Phys.* **103,** 1878–1885 (1995).

61. Feller, D. The role of databases in support of computational chemistry calculations. *J. Comput. Chem.* **17,** 1571–1586 (1996).
62. Boys, S. F. & Bernardi, F. The calculation of small molecular interactions by the differences of separate total energies. Some procedures with reduced errors. *Mol. Phys.* 553–566 (1970).
63. Keith, T. A. AIMAll, Version 12.05.09; TK Gristmill Software: Overland Park, KS, 2012, http://aim. tkgristmill. com. No Title.
64. R. Dovesi, R. Orlando, A. Erba, C. M. Zicovich-Wilson, B. Civalleri, S. Casassa, L. Maschio, M. Ferrabone, M. De La Pierre, P. D'Arco, Y. Noel, M. Causa, M. Rerat, B. K. & Int. J. Quantum Chem. 114, 1287 (2014). No Title.
65. Gatti, C. Topond 13. (2013).
66. Pendás, A. M., Francisco, E., Blanco, M. A. & Gatti, C. Bond Paths as Privileged Exchange Channels. *Chem. - A Eur. J.* **13,** 9362–9371 (2007).
67. Espinosa, E., Molins, E. & Lecomte, C. Hydrogen bond strengths revealed by topological analyses of experimentally observed electron densities. *Chem. Phys. Lett.* **285,** 170–173 (1998).
68. Spackman, M. A. How Reliable Are Intermolecular Interaction Energies Estimated from Topological Analysis of Experimental Electron Densities? *Cryst. Growth Des.* **15,** 5624–5628 (2015).
69. Gavezzotti, A. Non-conventional bonding between organic molecules. The 'halogen bond' in crystalline systems. *Mol. Phys.* **106,** 1473–1485 (2008).
70. Franchini, D., Dapiaggi, F., Pieraccini, S., Forni, A. & Sironi, M. Halogen bonding in the framework of classical force fields: The case of chlorine. *Chem. Phys. Lett.* **712,** 89–94 (2018).
71. Wilcken, R., Zimmermann, M. O., Lange, A., Joerger, A. C. & Boeckler, F. M. Principles and applications of halogen bonding in medicinal chemistry and chemical biology. *Journal of Medicinal Chemistry* **56,** 1363–1388 (2013).
72. Kolář, M. & Hobza, P. On Extension of the Current Biomolecular Empirical Force Field for the Description of Halogen Bonds. *J. Chem. Theory Comput.* **8,** 1325–1333 (2012).
73. Ibrahim, M. A. A. Molecular mechanical study of halogen bonding in drug discovery. *J. Comput. Chem.* **32,** 2564–2574 (2011).
74. Clark, T. & Hebelmann, A. The coulombic σ-hole model describes bonding in CX3I···Y− complexes completely. *Phys. Chem. Chem. Phys.* **20,** 22849–22855 (2018).
75. Scholfield, M. R. *et al.* Force Field Model of Periodic Trends in Biomolecular Halogen Bonds. *J. Phys. Chem. B* **119,** 9140–9149 (2015).
76. Bayly, C. I., Cieplak, P., Cornell, W. D. & Kollman, P. A. A well-behaved electrostatic potential based method using charge restraints for deriving atomic charges: The RESP model. *J. Phys. Chem.* **97,** 10269–10280 (1993).
77. Zhao, Y. & Truhlar, D. G. The M06 suite of density functionals for main group thermochemistry, thermochemical kinetics, noncovalent interactions, excited states, and transition elements: two new functionals and systematic testing of four M06-class functionals and 12 other functionals. *Theor. Chem. Acc.* **120,** 215–241 (2008).
78. Wang, J., Wolf, R. M., Caldwell, J. W., Kollman, P. A. & Case, D. A. Development and testing of a general amber force field. *J. Comput. Chem.* **25,** 1157–1174 (2004).
79. Lindorff-Larsen, K. *et al.* Improved side-chain torsion potentials for the Amber ff99SB protein force field. *Proteins Struct. Funct. Bioinforma.* **78,** NA-NA (2010).
80. Özpınar, G. A., Peukert, W. & Clark, T. An improved generalized AMBER force field (GAFF) for urea. *J. Mol. Model.* **16,** 1427–1440 (2010).

81. Lu, Y. *et al.* Halogen Bonding?A Novel Interaction for Rational Drug Design? *J. Med. Chem.* **52,** 2854–2862 (2009).
82. Brezgunova, M. E. *et al.* Charge Density Analysis and Topological Properties of Hal $_3$ - Synthons and Their Comparison with Competing Hydrogen Bonds. *Cryst. Growth Des.* **12,** 5373–5386 (2012).
83. El Hage, K., Bereau, T., Jakobsen, S. & Meuwly, M. Impact of Quadrupolar Electrostatics on Atoms Adjacent to the Sigma-Hole in Condensed-Phase Simulations. *J. Chem. Theory Comput.* **12,** 3008–3019 (2016).
84. Wang, C., Danovich, D., Mo, Y. & Shaik, S. On The Nature of the Halogen Bond. *J. Chem. Theory Comput.* **10,** 3726–3737 (2014).
85. Shaik, S. A personal story on a renaissance in valence bond theory: A theory coming of age! *Comput. Theor. Chem.* **1116,** 2–31 (2017).
86. Boys, S. F. Construction of Some Molecular Orbitals to Be Approximately Invariant for Changes from One Molecule to Another. *Rev. Mod. Phys.* **32,** 296–299 (1960).
87. Foster, J. M. & Boys, S. F. Canonical Configurational Interaction Procedure. *Rev. Mod. Phys.* **32,** 300–302 (1960).
88. Edmiston, C. & Ruedenberg, K. Localized Atomic and Molecular Orbitals. *Rev. Mod. Phys.* **35,** 457–464 (1963).
89. Pipek, J. & Mezey, P. G. J. No Title. *chem. phys.* **90,** 4916–4926 (1989).
90. Huzinaga, S. & Cantu, A. A. Theory of Separability of Many-Electron Systems. *J. Chem. Phys.* **55,** 5543–5549 (1971).
91. Adams, W. H. On the Solution of the Hartree-Fock Equation in Terms of Localized Orbitals. *J. Chem. Phys.* **34,** 89–102 (1961).
92. Gilbert, T. L. Multiconfiguration self-consistent-field theory for localized orbitals. II. Overlap constraints, Lagrangian multipliers, and the screened interaction field. *J. Chem. Phys.* **60,** 3835–3844 (1974).
93. Matsuoka, O. Expansion methods for Adams–Gilbert equations. I. Modified Adams–Gilbert equation and common and fluctuating basis sets. *J. Chem. Phys.* **66,** 1245–1254 (1977).
94. Stoll, H., Wagenblast, G. & Preuβ, H. On the use of local basis sets for localized molecular orbitals. *Theor. Chim. Acta* **57,** 169–178 (1980).
95. Smits, G. F. & Altona, C. Calculation and properties of non-orthogonal, strictly local molecular orbitals. *Theor. Chim. Acta* **67,** 461–475 (1985).
96. Francisco, E., Martín Pendás, A. & Adams, W. H. Generalized Huzinaga building-block equations for nonorthogonal electronic groups: Relation to the Adams–Gilbert theory. *J. Chem. Phys.* **97,** 6504–6508 (1992).
97. Couty, M., Bayse, C. A. & Hall, M. B. Extremely localized molecular orbitals (ELMO): a non-orthogonal Hartree-Fock method. *Theor. Chem. Accounts Theory, Comput. Model. (Theoretica Chim. Acta)* **97,** 96–109 (1997).
98. Fornili, A., Sironi, M. & Raimondi, M. Determination of extremely localized molecular orbitals and their application to quantum mechanics/molecular mechanics methods and to the study of intramolecular hydrogen bonding. *J. Mol. Struct. THEOCHEM* **632,** 157–172 (2003).
99. Sironi, M., Genoni, A., Civera, M., Pieraccini, S. & Ghitti, M. Extremely localized molecular orbitals: theory and applications. *Theor. Chem. Acc.* **117,** 685–698 (2007).
100. Genoni, A. X-ray Constrained Extremely Localized Molecular Orbitals: Theory and Critical Assessment of the New Technique. *J. Chem. Theory Comput.* **9,** 3004–3019 (2013).
101. Meyer, B., Guillot, B., Ruiz-Lopez, M. F. & Genoni, A. Libraries of Extremely Localized Molecular Orbitals. 1. Model Molecules Approximation and Molecular Orbitals

Transferability. *J. Chem. Theory Comput.* **12,** 1052–1067 (2016).
102. Genoni, A. & Sironi, M. A novel approach to relax extremely localized molecular orbitals: the extremely localized molecular orbital?valence bond method. *Theor. Chem. Acc.* **112,** 254–262 (2004).
103. Genoni, A., Fornili, A. & Sironi, M. Optimal virtual orbitals to relax wave functions built up with transferred extremely localized molecular orbitals. *J. Comput. Chem.* **26,** 827–835 (2005).
104. Genoni, A. & IUCr. A first-prototype multi-determinant X-ray constrained wavefunction approach: the X-ray constrained extremely localized molecular orbital–valence bond method. *Acta Crystallogr. Sect. A Found. Adv.* **73,** 312–316 (2017).
105. Casati, N. *et al.* Exploring charge density analysis in crystals at high pressure: data collection, data analysis and advanced modelling. *Acta Crystallogr. Sect. B Struct. Sci. Cryst. Eng. Mater.* **73,** 584–597 (2017).
106. Gerratt, J. & Lipscomb, W. N. Spin-coupled wave functions for atoms and molecules. *Proc. Natl. Acad. Sci. U. S. A.* **59,** 332–5 (1968).
107. Karadakov, P. B., Gerratt, J., Cooper, D. L. & Raimondi, M. Core-valence separation in the spin-coupled wave function: A fully variational treatment based on a second-order constrained optimization procedure. *J. Chem. Phys.* **97,** 7637–7655 (1992).
108. Cooper, D. L., Gerratt, J., Raimondi, M., Sironi, M. & Thorsteinsson, T. Expansion of the spin-coupled wavefunction in Slater determinants. *Theor. Chim. Acta* **85,** 261–270 (1993).
109. Chirgwin, B. H. & Coulson, C. A. The Electronic Structure of Conjugated Systems. VI. *Proc. R. Soc. A Math. Phys. Eng. Sci.* **201,** 196–209 (1950).
110. Ditchfield, R., Hehre, W. J. & Pople, J. A. Self-Consistent Molecular-Orbital Methods. IX. An Extended Gaussian-Type Basis for Molecular-Orbital Studies of Organic Molecules. *J. Chem. Phys.* **54,** 724–728 (1971).
111. Rumer, G. No Title. *Göttinger Nachr.* **3,** 337–341 (1932).
112. Kozuch, S. & Martin, J. M. L. Halogen bonds: Benchmarks and theoretical analysis. *J. Chem. Theory Comput.* (2013). doi:10.1021/ct301064t
113. Jayatilaka, D. Wave Function for Beryllium from X-Ray Diffraction Data. *Phys. Rev. Lett.* **80,** 798–801 (1998).
114. Jayatilaka, D., Grimwood, D. J. & IUCr. Wavefunctions derived from experiment. I. Motivation and theory. *Acta Crystallogr. Sect. A Found. Crystallogr.* **57,** 76–86 (2001).
115. Grimwood, D. J., Jayatilaka, D. & IUCr. Wavefunctions derived from experiment. II. A wavefunction for oxalic acid dihydrate. *Acta Crystallogr. Sect. A Found. Crystallogr.* **57,** 87–100 (2001).
116. Bytheway, I., Grimwood, D. J. & Jayatilaka, D. Wavefunctions derived from experiment. III. Topological analysis of crystal fragments. *Acta Crystallogr. Sect. A Found. Crystallogr.* **58,** 232–243 (2002).
117. Bytheway, I. *et al.* Wavefunctions derived from experiment. IV. Investigation of the crystal environment of ammonia. *Acta Crystallogr. Sect. A Found. Crystallogr.* **58,** 244–251 (2002).
118. Grimwood, D. J., Bytheway, I. & Jayatilaka, D. Wave functions derived from experiment. V. Investigation of electron densities, electrostatic potentials, and electron localization functions for noncentrosymmetric crystals. *J. Comput. Chem.* **24,** 470–483 (2003).
119. Gillet, J.-M. & IUCr. Determination of a one-electron reduced density matrix using a coupled pseudo-atom model and a set of complementary scattering data. *Acta Crystallogr. Sect. A Found. Crystallogr.* **63,** 234–238 (2007).
120. Gueddida, S. *et al.* Joint refinement model for the spin resolved one-electron reduced density matrix of $YTiO_3$ using magnetic structure factors and magnetic Compton profiles

data. *J. Chem. Phys.* **148,** 164106 (2018).
121. Hudák, M. *et al.* X-ray constrained unrestricted Hartree–Fock and Douglas–Kroll–Hess wavefunctions. *Acta Crystallogr. Sect. A Found. Crystallogr.* **66,** 78–92 (2010).
122. Bader, R. Atoms in Molecules: A Quantum Theory: Oxford Univ. Press. (1990).
123. Becke, A. D. & Edgecombe, K. E. A simple measure of electron localization in atomic and molecular systems. *J. Chem. Phys.* **92,** 5397–5403 (1990).
124. Kohout, M. A measure of electron localizability. *Int. J. Quantum Chem.* **97,** 651–658 (2004).
125. Schmider, H. . & Becke, A. . Chemical content of the kinetic energy density. *J. Mol. Struct. THEOCHEM* **527,** 51–61 (2000).
126. Dos Santos, L. H. R., Genoni, A., Macchi, P. & IUCr. Unconstrained and X-ray constrained extremely localized molecular orbitals: analysis of the reconstructed electron density. *Acta Crystallogr. Sect. A Found. Adv.* **70,** 532–551 (2014).
127. Genoni, A. & Meyer, B. X-Ray Constrained Wave Functions: Fundamentals and Effects of the Molecular Orbitals Localization. *Adv. Quantum Chem.* **73,** 333–362 (2016).
128. Casati, N. *et al.* Exploring charge density analysis in crystals at high pressure: data collection, data analysis and advanced modelling. *Acta Crystallogr. Sect. B Struct. Sci. Cryst. Eng. Mater.* **73,** 584–597 (2017).
129. Goldfeld, S. M., Quandt, R. E. & Trotter, H. F. Maximization by Quadratic Hill-Climbing. *Econometrica* **34,** 541 (1966).
130. Bürgi, H.-B. *et al.* Electron Distribution and Molecular Motion in Crystalline Benzene: An Accurate Experimental Study Combining CCD X-ray Data on C6H6 with Multitemperature Neutron-Diffraction Results on C6D6. *Chem. - A Eur. J.* **8,** 3512 (2002).

ACKNOWLEDGEMENT

Firstly, I would like to express my sincere gratitude to my advisor Prof. Maurizio Sironi for the continuous support during these three years of PhD studies. Particularly, his guidance helped me during both the good and less good moments of this path, enhancing the quality of my research.

Besides my advisor, I would sincerely like to thank my co-tutors Dr. Alessandra Forni and Dr. Stefano Pieraccini for always being ready to help me and for their great patience.

A very special thanks goes to Dr. Alessandro Genoni, who welcomed me in Metz during my period abroad. Moreover, his patience and commitment to our research projects made me grow up as a scientist and chemist. I will really miss our skype-call!

I am very grateful to Dr. Anna Krawczuk and Dr. Vincent Tognetti, that have been very good reviewers of my thesis, pushing, with their comments and questions, the awareness of my research further. Also, I should like to thank the president of my PhD school, Prof. Emanuela Licandro, and the members of my defense committee: Prof. Piero Ugliengo, Prof. Enrique Espinosa and Prof. Alberto Vertova.

Among other "Academia" people, I have to thank the collegues at Unimi (Giovanni M., Fabio G., Stefano, Federico, Francesco, Rosario, Enrico B., Enrico G., Crescenzo, Ambra, Francesca, Mirko, Giovanni D., Giorgio, Mattia, Matteo, Fabio B. and many others) and the ones known during schools and meetings (Felipe, Carlos, Malte, Athas, Erna, Giovanni, Debora...)

Beside Academia, a very special acknowledgement goes to my family (Mamma, Papà, Marco, Chiara and all the grandparents). Especially, my parents supported me, from a moral point of view, in a very special way. Particularly, my mother never doubted me, even when I did.

Also, I would like to thank my own "fellowship of the ring" (Pippo, Beg, Vene, Nome, Divi, Ludo, Emi and the others). You are not the friends I deserve but you have always been the ones I have needed (yes, the opposite of Batman). Thank you for being my shieldwall also when I should have been exiled to the Wall (deep down inside, we all know it, we are nerds). I hope that our "birrette al Ghost" will never end.

Finally, I would like to thank Monica the first girl who has been able to make me find a little bit of peace and quiet with myself. I know that putting up with me is a titanic effort, but I hope you will be able to manage it for a long time, because you have been the fuel in the last part of this journey.